A 2D MODEL OF SEMI-MOLTEN DROP IMPACT FOR THERMAL SPRAY APPLICATION

By

Tommy Che-Ming Wu

A thesis submitted in conformity with the requirements
for the degree of Master of Applied Science
Graduate Department of Materials Science and Engineering
University of Toronto

Abstract

A 2D Model of Semi-Molten Drop Impact for Thermal Spray Application

Tommy Che-Ming Wu

Master of Applied Science
Graduate Department of Materials Science and Engineering
University of Toronto
2009

In thermal spraying, semi-molten (or partially-melted) particles are likely to form when the sprayed particles are insufficiently heated, or when a composite material is deposited. The present 2D model serves to begin to assess the spreading behavior of a semi-molten particle when impacting a solid substrate.

An *Immersed-Boundary* (IB) scheme was implemented in an axisymmetric fluid model to simulate fluid flow in the presence of a solid core. The IB method calculates a forcing term, which is added to the momentum equation, to enforce the no-slip boundary condition at the core surface.

Results are presented for the impact of a semi-molten tin droplet of radius R for a wide range of solid core radii r, varying the drop size ratio r/R, and the impact velocity U_o. To take into account the fluidity of a semi-molten drop, a modified maximum spread degree, $\xi^*_{\max}$, is defined. The maximum spread degree $\xi^*_{\max}$ is found to decrease significantly when the solid core size r is comparable to the drop size R. As the solid core size increases, one significant change in fluid behavior during spreading is that the rate of energy dissipation of inertia to viscous forces and surface tension increases, which causes fluid to recoil at an earlier time than a completely molten tin drop.

Acknowledgements

I would like to express my thanks and appreciations to my supervisor, Professor J. Mostaghimi for giving me this great opportunity to work on this challenging project. His invaluable guidance, patience, encouragement, and financial support will always be appreciated.

My sincere gratitude goes to my co-supervisor Professor M. Bussmann for helping me solve so many problems and providing me with many insightful suggestions. Without his involvement, this work will not have been possible. His encouragement and kindness will always be remembered.

I would like to thank my friends, Ken Chien, Jack Chang, and Kevin Tsai for their invaluable friendship. Their friendship has made my graduate life in Toronto so wonderful that many good memories were created.

I would like express my heartfelt thanks to my lady, Lynn, and to my family. Thanks for your love and encouragement. You are always my biggest motivation to overcome any obstacles that I encountered. Thanks for your understandings and for giving me so much freedom to pursue my little research dream that now is finally complete.

This work was made possible through the financial assistance by the University of Toronto in the forms of Fellowship.

CONTENTS

LIST OF FIGURES

CHAPTER 1

CHAPTER 2

CHAPTER 3

CHAPTER 4

CHAPTER 5

CHAPTER 1

INTRODUCTION

1.1 Thermal Spray Process and Uses

Thermal spraying is a line-of-sight coating process in which feedstock (coating precursor), which is supplied in the form of either powder or wire, is melted and sprayed onto a surface. The principle behind thermal spraying is to melt the coating material into molten particles and accelerate them towards the substrate surface where deposition occurs. Hence, both heating and momentum transfer are important to the coating deposition. The heat sources employed for melting can be derived either from chemical means (combustion gases) or from electric means (plasma or electric arc). As the particles impinge on the surface, they flatten and solidify rapidly (a few μs) to form a splat, and successive impingement of particles builds up splats layer-by-layer to form a laminar structure which is common to all thermal sprayed coatings. The successive stages of thermal spray coating deposition are shown in Figure 1.

A major advantage of thermal spraying processes is the ability to spray a wide range of materials including ceramics, cermets, metallics and composite coatings for diverse applications. Virtually any material that melts without significant thermal decomposition can be coated onto a substrate surface. Industrial applications include thermal barrier coatings (TBCs) [1,2], abrasive and erosive wear resistance [3,4], corrosion resistance [18], high-temperature erosion-oxidation resistance [5], improving the biocompatibility of medical implants [6], and the fabrication of solid oxide fuel cells (SOFCs) [7].

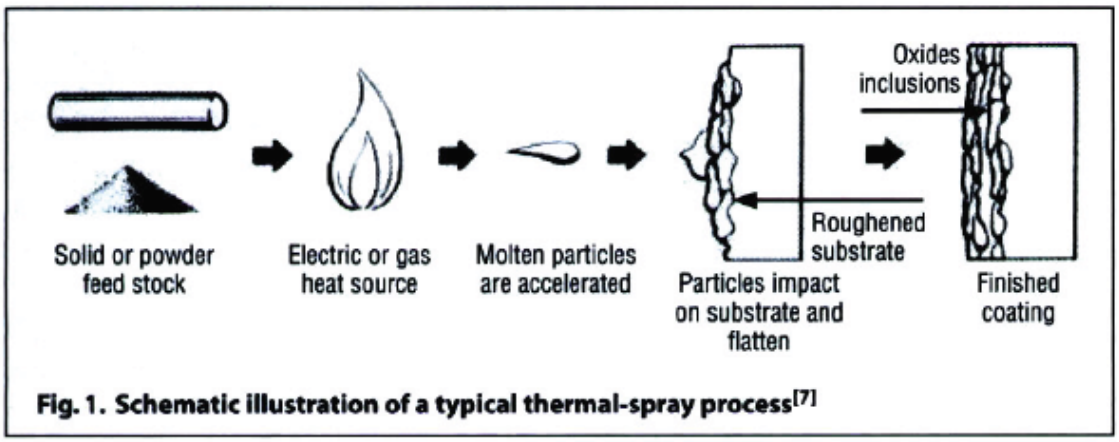

Figure 1- The successive stages of coating formation in the thermal spray process [8]

1.1.1 Various Spraying Techniques

Thermal spray coatings are fabricated by a variety of systems, distinguished based on the feedstock characteristics (wire/powder) and the heat sources employed for melting the feedstock (combustion gases, plasma or electric arc). In the following, various thermal spray processes are described:

Heat sources derived from the combustion gases:

- Flame spraying (FS), conventional combustion
- High velocity oxy-fuel process (HVOF)
- Detonation-Gun Spraying (D-Gun)

Heat sources derived from either electric arc or plasma gases:

- Arc spraying (AS)
- Atmospheric plasma spraying (APS)
- Vacuum plasma spraying (VPS)

A comparison of the characteristics of different thermal spraying techniques is shown in Table 1 .

Table I: Characteristics of Various Thermal-Spray Processes and Their Materials Characteristics.

Spray type	Feed type	Flame temperature	Particle velocity (m/s)	Materials	Microstructural features	Applications
Combustion	Wire/ powder	~3000°C	~40–100	Metals, polymers, ceramics	Relatively high porosity and oxidation	Reclamation, corrosion protection
HVOF	Powder	~3000°C	~400–800	Metals/cermets, low-melt ceramics	High density, excellent adhesion, compressive stresses	Wear protection
Two-wire arc	Wire	~3000–6000°C	50–150	Metals, cermets (cored wires)	Reasonably dense, thick	Reclamation, wear coatings
Plasma	Powder or wire	~5000–25,000°C	80–300	Ceramics, metals	Porosity in ceramic deposits	Thermal barriers, insulators
Cold spray	Powder	Room temperature	400–800	Metals	Dense, compressive stresses	Conductors, reclamation, cladding

Table 1- comparison of various thermal spraying techniques [9]

Combustion spraying, also referred as flame spraying (FS), uses the combustion gases derived from an oxy-fuel chemical reaction to melt the coating material. Flame spraying is available to spray materials in both powder and rod/wire form. In the powder-fed system, see Figure 2 (a), the combustion gases are used to both melt and accelerate the molten particles, which only attain relatively low particle velocity (40-100 m/s). In the wire-fed system, see Figure 2 (b), the combustion gases are only used to melt the wire tip, while a compressed air jet atomizes the molten tip to form small liquid droplets and accelerate them to a higher particle velocity (230-295 m/s) than the powder combustion system. In both types, the combustion flame is controlled by the fuel/oxygen ratio and the fuel type. The fuel/oxygen ratio may vary from 1:1 to 1.1:1, which results in changes in the atmosphere from carburizing to oxidizing, respectively [10]. The types of fuels used in FS spraying processes include propane, acetylene, hydrogen, natural gas, and methyl-

acetylene-propadiene (MAPP), and the choice of fuel type will change the flame temperature (~3000 $^{\circ}C$). In general, the coatings produced by FS spraying exhibit high porosity (10-20%) and low bond strength (typical values are in the range of 15 MPa for ceramic coatings to 30 MPa for other materials [10]) due to the relatively low flame temperature and low particle velocity. Nevertheless, FS spraying has merit due to its cost-effectiveness, ease of operation, and low-cost maintenance.

A novel variation of combustion spraying is High Velocity Oxy-Fuel Spraying (HVOF) which was developed at the beginning of the 1980s by Bick et al. [11] and Kreye et al. [12]. Fuel, usually propane, propylene, MAPP, or hydrogen is mixed with oxygen and burned in a combustion chamber. The flame temperature is also around 3000 $^{\circ}C$, similar to the flame temperature in FS. The HVOF spraying employs a special torch design, see Figure 2 (c), in which the combustion flames are expanded through a converging-diverging nozzle where the gas velocities increase significantly (1500 to 2000 m/s) [13]. The powder is usually injected axially in the nozzle where it is heated and accelerated. The powder is usually fully or partially melted and achieves velocities in the range of 500 m/s to 800 m/s [14]. The HVOF process produces coatings with low porosity and high bond strength (exceeding 69 MPa), and is ideal for metallic and cermet coatings due to the low flame temperature and high gas velocity.

In detonation gun spraying (D-gun), a mixture of oxygen and acetylene, along with a pulse of injected powder, is introduced into a barrel and detonated using a spark, see Figure 2 (d). The high-temperature and high-pressure detonation wave moving down the barrel melts the powder particles and accelerates them to a velocity above 850-1000 m/s [15]. D-gun spraying is a cyclic process. After each detonation, the barrel is purged with nitrogen gas and the process is repeated about 10 times per second.

In two-wire arc spraying, two wires of consumable electrodes are drawn axially to a common point at which the two wires are nearly contacting, see Figure 2 (e). The potential difference between the two electrodes generates an arc, which then melts the wire tips. A nozzle then guides the compressed air across the arc zone, atomizing the

molten metal on the wire tips and propelling them onto the substrate [16]. One of main restrictions of arc spraying is that coating materials have to be electrically conductive, and hence the process is limited to metallic coatings such as zinc and aluminum used for anodic protection against corrosion in the marine industry.

Finally, in plasma spraying, an electric arc is struck between the tungsten cathode and an annular water-cooled copper anode, see Figure 2 (f). The working gases are allowed to flow in between the cathode and the anode. In plasma spraying, an electric arc is discharged between the anode and the cathode. The arc, which is supported by a generator through the connectors, heats up the working gases to high temperatures such that they become ionized, and so creates a high-pressure plasma. Powder is introduced into the gas stream just outside the torch in the diverging region of the nozzle (copper anode). The resulting increase in temperature may exceed 30,000 $^{\circ}C$. The working gases can be either monatomic (Ar and He), molecular (H_2, N_2), or a mixture of both. The choice of working gases is dictated by the ability to melt the sprayed particles; the molecular gases have higher thermal conductivity than the atomic gases so that the plasma temperature for the monatomic gas is higher. On the other hand, the monatomic gases reach a higher gas velocity so more kinetic energy is imparted to sprayed particles. Hence, a mixture of molecular and monatomic gases ensure sufficient melting as well as acceleration of the powder. The particle velocity achieved in plasma spraying ranges from 250 to 560 m/s [14]. Power levels in plasma spray torches are usually in the range of 30 to 80 kW.

For high performance applications, plasma spraying is conducted in a reduced pressure ($10^{-4} \sim 10^{-5}$ torr) inert gas environment, referred to as the Vacuum Plasma Spraying process (VPS). The VPS produces high quality coatings for oxygen-sensitive materials such as MCrAlY, Ni_3Al, and $MoSi_2$; nevertheless, it is a cost-intensive and time-consuming process, and the sprayed parts are often limited by the chamber size.

a)

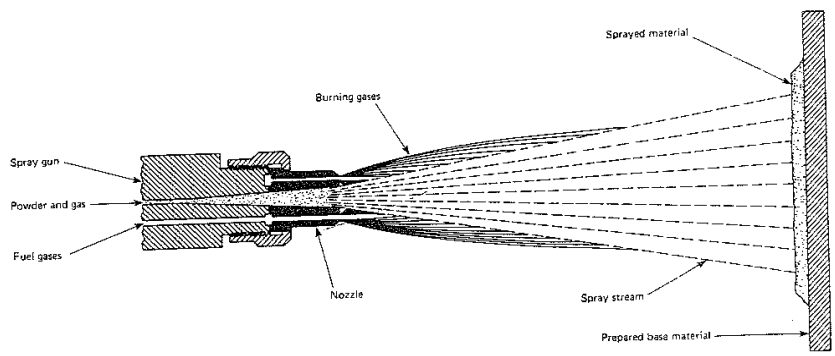
Sprayed material
Burning gases
Spray gun
Powder and gas
Fuel gases
Nozzle
Spray stream
Prepared base material

b)

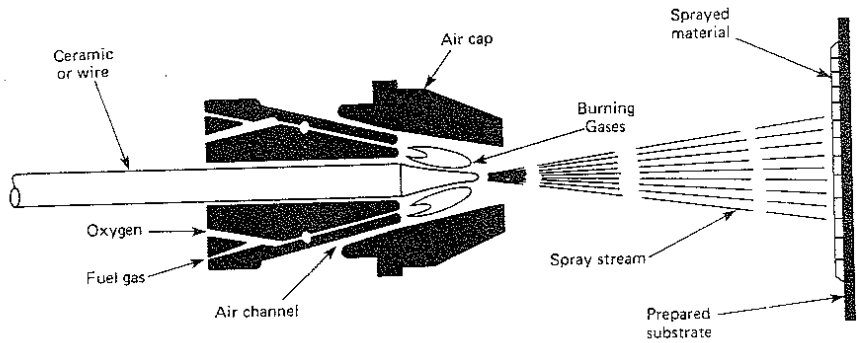
Sprayed material
Air cap
Ceramic or wire
Burning Gases
Oxygen
Fuel gas
Air channel
Spray stream
Prepared substrate

c)

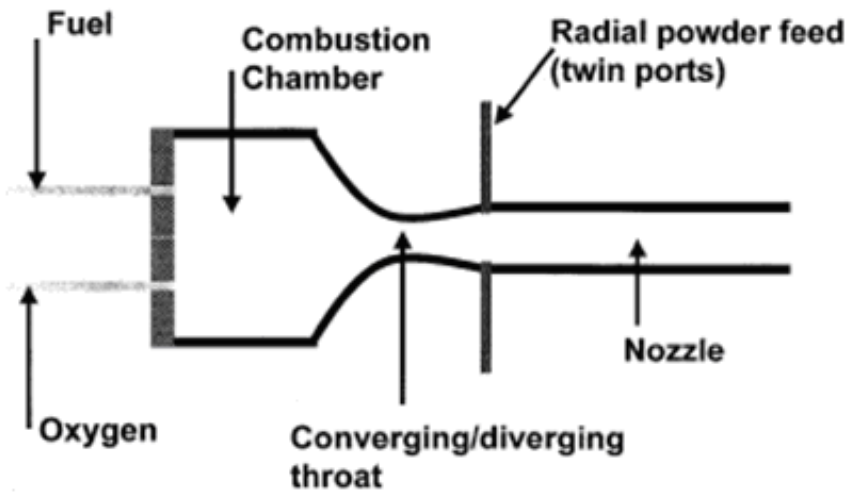
Fuel
Combustion Chamber
Radial powder feed (twin ports)
Nozzle
Oxygen
Converging/diverging throat

d)

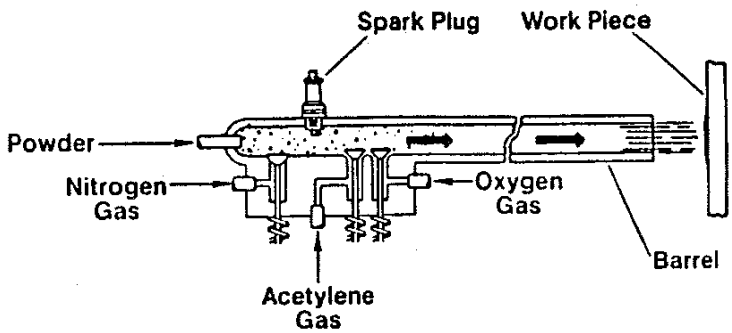

e)

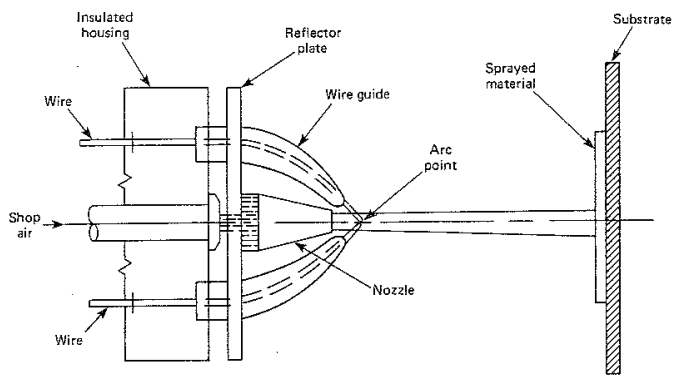

f)

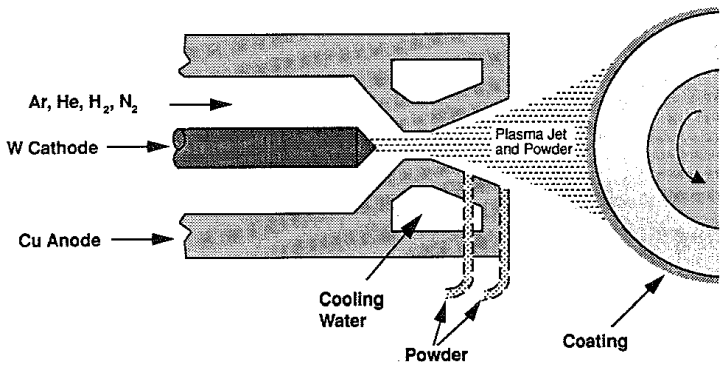

Figure 2- Schematics of: a) powder-fed flame spray torch, b) wire-fed flame spray torch, c) Jet Kote high velocity oxy-fuel gun torch (HVOF), d) D-Gun torch, e) Arc spray torch, f) plasma spray torch [17,18, 14,15].

1.2 Droplet Impact

Overall microstructure and coating properties in thermal spray processes are affected by how well splats are deposited [19,20]. Splat formation occurs in a very short period of time (a few μs), but the physical and chemical processes involved are extremely complex. One advantage of using a numerical model to analyze the process is the ability to isolate a specific group of physical parameters and study how they affect the overall splat deposition process. In addition, modeling can provide insights into the rapid deposition process, while experimental results can only be collected via high-speed cameras [21] and fast-response particle measurement sensors (such as DPV-2000) [22].

In general, the fundamental processes involved during splat formation can be divided into two main areas. The first deals with the flattening behavior of a splat, which can be investigated from the fluid dynamics point of view. The second deals with the heat transfer from a molten droplet to the substrate.

In this thesis, the focus is on the first area while the effects of solidification are neglected. In particular, we focus on modeling the spreading behavior of a two-phase droplet following impact on a solid surface.

1.2.1 Molten Droplet Impact

A splat is formed by the impingement of a molten droplet, followed by rapid solidification as the droplet spreads laterally across a substrate, see Figure 3. The behavior of a flattening splat is governed by the interplay of inertial, viscous and surface tension forces. During spreading, the inertia of the droplet will be dissipated by viscous and surface tension forces. When the droplet reaches a maximum spread diameter, inertia is at a minimum and the rim of the droplet starts to recoil.

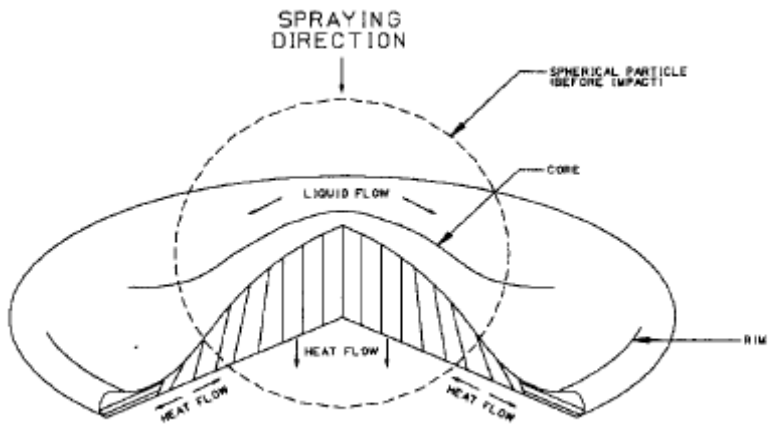

Figure 3- Splat formation in the thermal spray process [23]

The relative importance of these forces is expressed by two non-dimensional groups:

$$We = \frac{\rho D_o U_o^2}{\sigma}$$

$$Re = \frac{\rho D_o U_o}{\mu}$$

where ρ is the fluid density, D_o is the initial droplet diameter, U_o is the initial impact velocity, σ is the surface tension coefficient, and μ is the viscosity. The Weber number (We) provides a measure of the relative magnitudes of inertial and surface tension forces. The Reynolds number (Re) provides a measure of the relative magnitudes of inertial energy and viscous forces.

1.2.2 Semi-Molten Droplet Impact

In thermal spraying, semi-molten particles (or partially-melted particles) are often observed [24,25]. There are two general situations in thermal spraying that a semi-molten droplet is formed. The first is when the sprayed powder is not completely melted due to insufficient thermal loading from the gas stream to the in-flight particle. As a result, only the surface region of the particle is melted while the center core remains solid. The second situation is when a composite powder of two different materials agglomerated into a single composite droplet is sprayed in the semi-molten state. For example, during the deposition of tungsten carbide cobalt (WC-Co) coating, the WC carbides remain solid while the Co matrix is completely melted to allow maximum spreading of the droplet, See Figure 4.

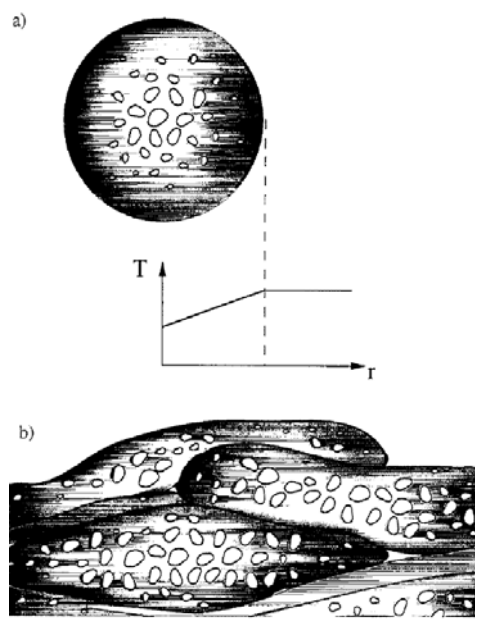

Figure 4- Impingement of a WC-Co droplet to form a thermal spray coating [26]

In both situations, less thermal degradation occurs to the feedstock powder when the powder is sprayed at lower gas-stream temperatures. Spraying at lower gas temperatures is beneficial for fabricating heat-sensitive materials. One group of these materials is the metallic coatings such as Ti, MCrAlY, and Inconel 625. These materials are degraded

due to the formation of oxides when exposed to high temperatures. As a result, their coating lifetime reduces significantly as oxides are prone to spall away when put under stresses [27,28]. Another group of these materials is the cermet coatings such as WC-Co and Cr_3C_2-NiCr. These cermet coatings are degraded due to decarburization of carbides. Carbides are the harder phase that provides the wear-resistance of the coating. Therefore, as the number of carbides decreases due to severe decarburization, the coating wear resistance decreases [26,29,30,5]. For both types of materials, spraying at lower gas temperatures will minimize the effects of oxidation, decarburization, and dissolution, but it also leads to insufficient melting of all solid particles.

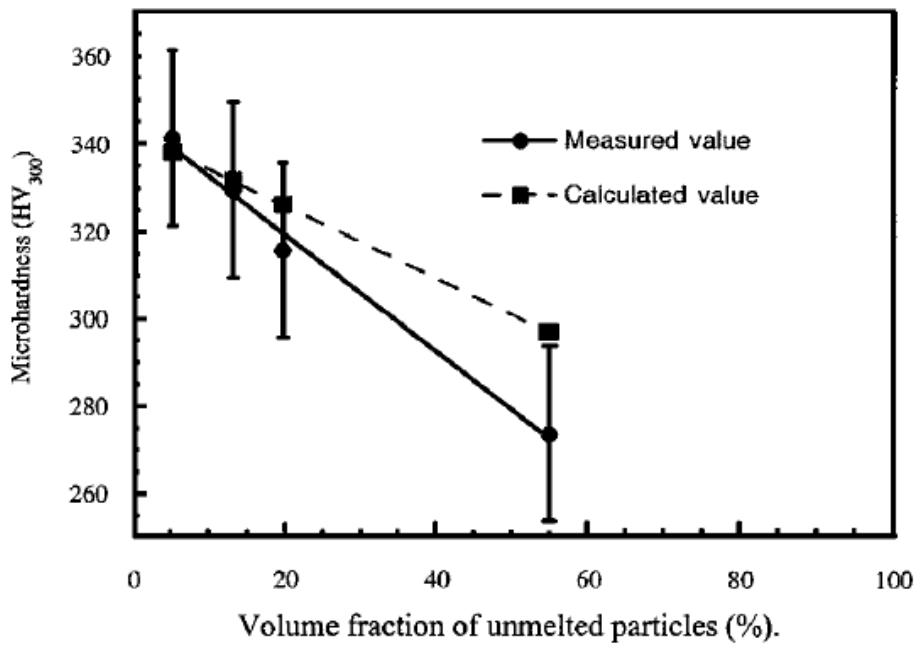

Figure 5- Relationship between microhardness and volume fraction of unmelted particles for Inconel 625 coatings sprayed by the HVOF conditions [31]

As the gas temperature decreases, the number of unmelted particles increases, which causes more voids (porosity) in the coating. As a result, the mechanical strength of the coating decreases with increasing the porosity. For example, a relationship between the microhardness and the volume fraction of unmelted particles was analyzed for the Inconel 625 coating [31]. Figure 5 shows that the microhardness of the coating decreases

linearly with increasing the volume fraction of the unmelted particles, as more porosity is formed at the higher volume fraction of unmelted particles. The SEM micrograph of the 625 coating that contains 54 vol% of unmelted particles is shown Figure 6. It was speculated that the high porosity in the coating is formed by the voids in the inter-splat region of the unmelted particles, see Figure 7.

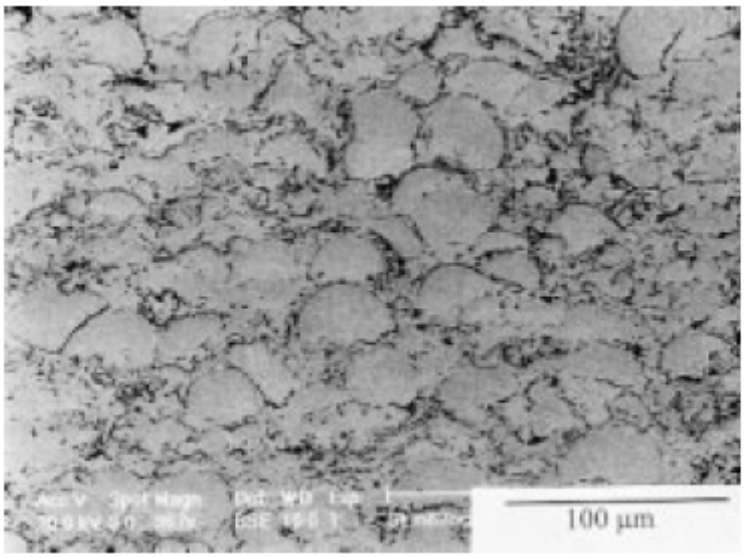

Figure 6- 54 vol% of unmelted particles in Inconel 625 coatings sprayed from powder with mean size of 36 μm [31].

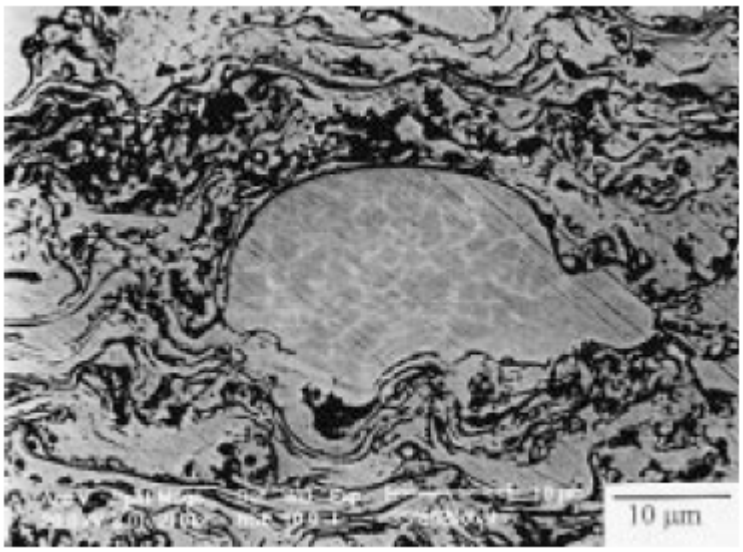

Figure 7- SEM image of Inconel 625 coatings illustrates the voids in microstructure (the black region) near an unmelted particle [31].

For the composite material of WC-Co coating, the carbide size was found to have a significant impact on the flattening of the composite droplet upon impact on a substrate. Kazumi et al.[32] indicated that powders with smaller mean WC carbide sizes formed denser coatings than those with large carbides. This is because the spread degree of a WC-Co drop is higher when it contains smaller carbides, as the liquid matrix is less restrained by them when it flows laterally. In addition, Li et al. [33] observed that large WC carbides tend to rebound off the splat, leading to a significant loss of carbides. Splat samples were collected from three types of feedstock powders- each type of powder contains a different mean carbide size, ranging from 1.5 μm to 3.0 μm. In Figure 8 (a), type 1 powder containing a mean carbide size of 1.5 μm formed a splat with a dense population of well-distributed carbides. In Figure 8 (b), type 2 powder with a slightly larger mean carbide size of 2.35 μm formed a splat in which carbides embossed out of the splat surface; nevertheless, the carbides were still embedded beneath the splat surface. In Figure 8 (c), type 3 powder with the largest mean carbide size of 3.06 μm formed a splat in which large carbides rebounded off the splat surface completely, leaving the splat consisting of the cobalt phase only.

Li et al. further proposed a model to describe the flattening mechanism of a solid-liquid composite droplet. An expected splat thickness δ_e, based on the Jones' approach [34], was first determined with the Reynolds number of the liquid phase:

$$\frac{D}{\delta_e} = \left(8\frac{\rho D U_o}{\mu}\right)^{0.25} \text{ and } \mu = \mu_0 \left(1 - V\right)^{-1}$$

where ρ is the fluid density, D is the droplet size, U_o is the impact velocity, μ is the liquid viscosity, and V is the volume fraction of WC grains. Based on the relative size of carbides, denoted as d_s, three possible outcomes could occur.

a)

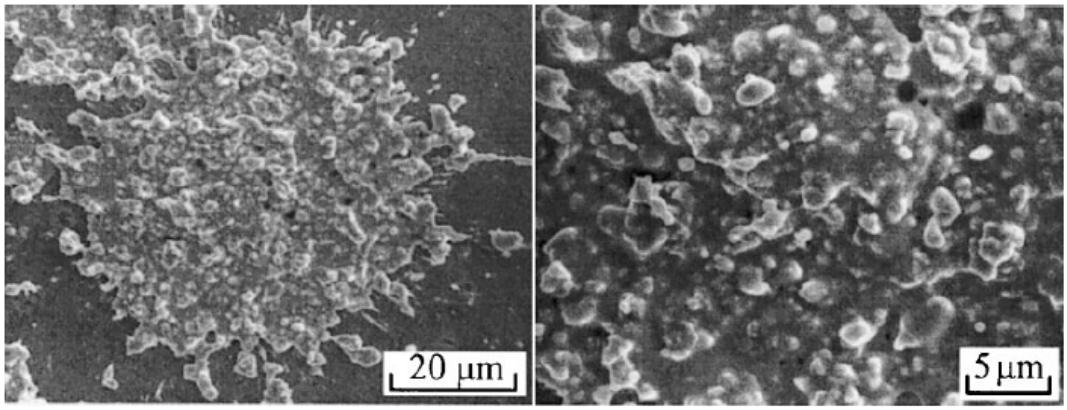

b)

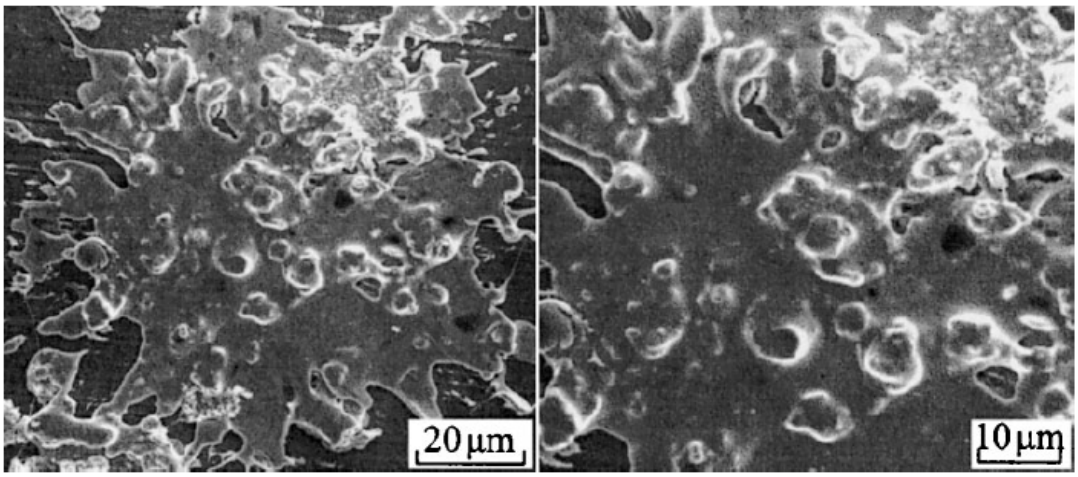

c)

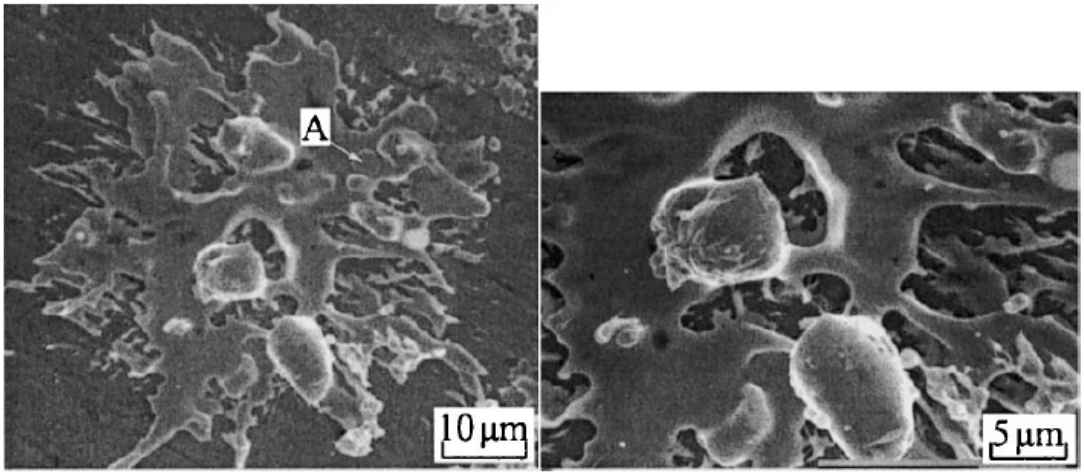

Figure 8- Splat formation of WC-Co with dfferent mean WC grain size a) 1.5 μm, b) 2.35 μm, and c) 3.06 μm [33].

If $d_s < \delta_e$ (Case I), then the flattening of the splat is dominated by the fluid behavior, see Figure 9 (a) and (b). If $d_s \cong \delta_e$ (Case II), then the splat thickness will be roughly the same as the carbide size, see Figure 9 (c). If $d_s < \delta_e$ (Case III), the carbide will tend to rebound off the splat surface, leaving a splat consisting of the binder phase only, see Figure 9 (d).

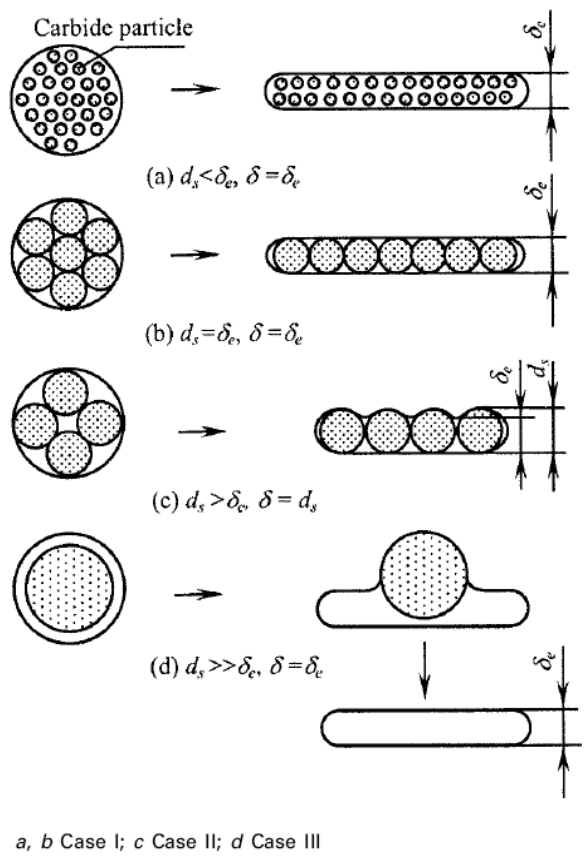

Figure 9- Correlation between the mean sizes of WC particle in the sprayed coatings and the mean sizes of WC particle in the powder feedstock [33].

1.3 Modeling Droplet Impact

In this section, modeling studies of thermal spray droplet impact are reviewed. Harlow and Shannon [35] were the first to investigate the splash of a liquid drop onto a flat plate by solving the full Navier-Stokes equations with the “Marker-and-Cell” method (MAC, in which a set of marker particles are used to track the position and shape of the free surface in the Lagrangian reference of frame). In their calculations, surface tension and viscous force effects were neglected. Tsurutani [36] added the surface tension and viscous effects into the MAC method and also considered the solidification effect of a droplet as it spread. Trapaga and Szekely [37] modeled the impact of molten particles in a thermal spray process by using an Eulerian free surface interface tracking algorithm called the volume of fluid (VOF) method, incorporated into the commercial software, FLOW-3D. Liu [38] used another type of VOF-based code, RIPPLE [39], to simulate molten metal droplet impact. Pasandideh-Fard [40] used a modified SOLA-VOF method to simulate water droplet impact with varying the liquid-solid contact angle, by adding different amounts of a surfactant. Zhao and Poulikakos [41] then followed by incorporating solidification into the MAC method in modeling liquid metal and water droplet collisions. Fukai [42] used the adaptive-grid finite element method to simulate water droplet impact while also taking into account wetting effects. Waldvogel and Poulikakos [43] studied thermal spraying of molten ceramic particles. Bussmann [44] used a fixed-grid Eulerian model with the VOF algorithm to model water droplet impact on an inclined plane and the edge of a step.

1.3.1 Review of VOF and IB methods

As mention above, modeling droplet impact involves solving for the free surface interface along with the flow field. There are two ways of modeling free-surface interfacial flow: one is an Eulerian approach (VOF) and the other is a Lagrangian approach (MAC). VOF was first developed by Hirt and Nichols [45]; a common VOF method used nowadays is based on the RIPPLE code, which was developed by Kothe et al. [39]. VOF implicitly tracks the interface based on the volume fraction in Eulerian mesh cells, which is represented by a color function f . In each timestep, the volume fraction f is advected with the fluid flow based on the material derivative, and then the interface is reconstructed based on the new value of the advected f .

In addition to tracking the free surface of a liquid, when modeling the impact of a partially-molten droplet, the liquid flow behavior in the presence of a solid core must also be simulated. The no-slip boundary condition at the solid/liquid interface requires the local fluid velocity to have the same values as those on the solid surface. Hence, the dynamics of fluid motion must be coupled with the rigid body motion of solid core. Here, the coupling is done via the Immersed Boundary method (IB), by introducing a force term to the Navier-Stokes equations. The principle behind the IB method is that the fluid “sees” a solid body through the forces of pressure and shear that exist along the body surface. Thus, if one were to apply the correct forces, the fluid would flow as though it were passing over a solid object. Thus, the advantage of IB is that multi-phase flow can be solved on a regular fixed Eulerian mesh without introducing any body-conformal grid structure. The imposition of the external force field is enabled by a set of massless Lagrangian points that are located on the immersed boundary and move with the local fluid velocity.

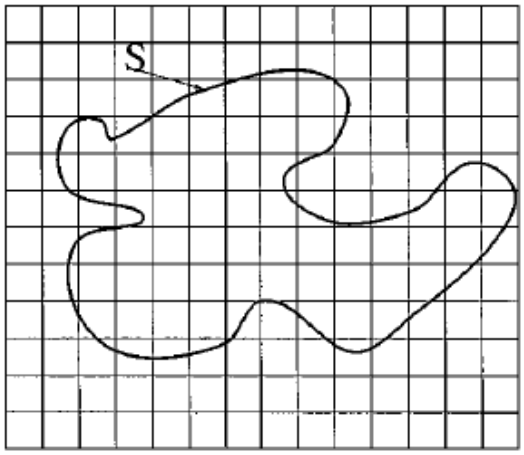

Figure 10 Schematic of an Eulerian mesh and Lagrangian marker points

Moreover, the positions of the Lagrangian points needed not necessarily be coincident with the Eulerian grid points, and so they can have any arbitrary shape and time-dependent positions with respect to the Eulerian grid, Figure 10.

IB was first introduced by Peskin [46,47] to simulate blood flow within a beating heart valve, and it has involved into a general method for solving multi-phase flow. An excellent review on different classes of the IB method is given by Mittal et al [48]. Different IB methods can be distinguished by the means of calculating the forcing term, which is incorporated into the momentum equations. Goldstein et al. [49] calculated the forcing via a *feedback* scheme, in which the forcing is solved iteratively by minimizing the deviation between the local fluid velocity and its desired values. The feedback mechanism is reminiscent of a damped oscillator system, in which a set of virtual strings and dampers attached to the surface points on the boundary restore the target values by generating a force in the opposite direction. One drawback of the feedback scheme is that it induces spurious oscillations and restricts the computational timestep associated with numerical stability [50, 51].

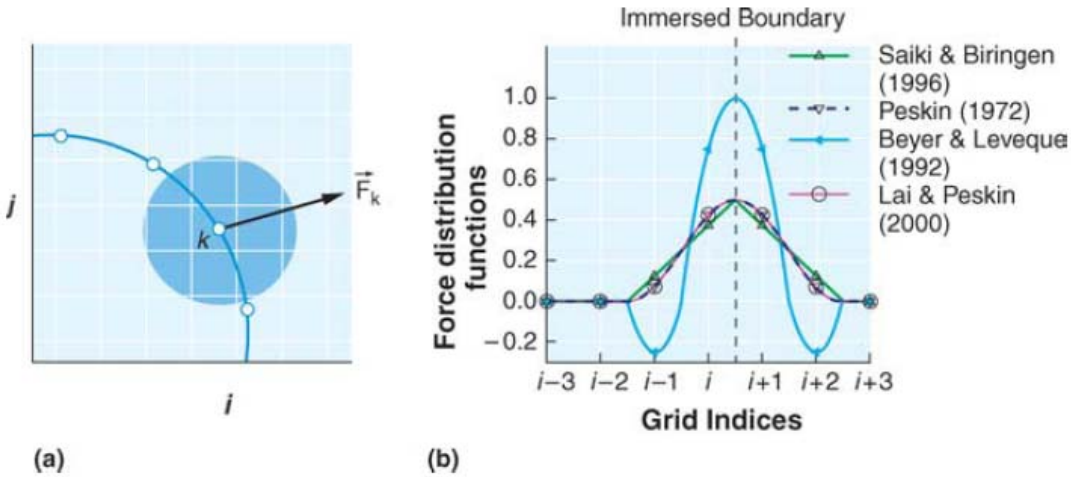

Figure 11 – a) Spreading of the direct forcing over a band of cells, b) force distribution functions employed by various studies.

Fadlun et al. [52] introduced a different scheme referred as *direct forcing*. In direct forcing, a fluid velocity is estimated, *a priori*, based on all of the source terms, but not taking the presence of the immersed boundary into account. The estimated local velocity is then made to satisfy the no-slip boundary condition by explicitly calculating the forcing through direct imposition of the desired velocities. The forcing is direct in the sense that the desired value of the local fluid velocity on the boundary is imposed directly without any dynamical process. After the forcing is calculated on the Lagrangian force points, it id transferred to the Eulerian grid nodes via an interpolation procedure, since the grid nodes do not necessarily coincide with the Lagrangian force points. Uhlmann [53] incorporated a better interpolation procedure into the direct forcing IB scheme, based on Peskin's delta function [46]. The transfer via the Dirac delta function is executed through a discretized form of s smooth distribution function, which spreads each singular force over a band of cells, see Figure 11 (a). The discrete form of the Dirac delta distribution function is a key ingredient to the IB method, and improvements to the function have been made by a number of researchers [54,55,56,57], as plotted in Figure 11 (b).

1.4 Objectives

The first objective of this research was to incorporate the immersed boundary scheme developed by a number of researchers [52,53,55] into the axisymmetric flow model developed by Lucente [58] in order to simulate two-phase droplet impact in the thermal spraying process.

Using this model, the second objective was to investigate the influence of a solid core on the spreading behavior of a semi-molten tin drop, in order to:

1) Compare the spreading behavior of a completely molten drop and a semi-molten drop.

2) Assess the correlation between the spreading degree and the size of the solid core, where the size of the solid core represents melting degree of a molten particle.

In the remainder of this thesis, Chapter 2 and Chapter 3 describe the methodology used to model axisymmetric impact of a semi-molten drop. Chapter 4 describes the verification tests that were carried out to validate the model. Chapter 5 describes the results of the model. Chapter 6 concludes the thesis.

References

[1] A Rabiei and AG Evans. Failure mechanisms associated with the thermally grown oxide in plasma-sprayed thermal barrier coatings. *Acta Materialia*, 48:3963-3976, 2000.

[2] R Taylor and JR Brandon. Microstructure, composition, and property relationships of plasma-sprayed thermal barrier coatings. *Surface and Coatings Technology*, 50:141-149, 1992.

[3] P Saravanan, V Selvarajan, DS Rao, SV Joshi, and G Sundararajan. Influence of process variables on the quality of detonation gun sprayed alumina coatings. *Surface and Coatings Technology*, 123:44-54, 2000.

[4] M Gell, EH Jordan, YH Sohn, D Goberman, L Shaw, and TD Xiao. Development and implementation of plasma sprayed nanostructured ceramic coatings. *Surface and Coatings Technology*, 146-147: 48-50, 2004.

[5] BQ Wang and K Luer. The erosion-oxidation behavior of HVOF Cr_3C_2-NiCr cermet coating. *Wear*, 174:177-185, 1994.

[6] KA Khor, H Li, and P Cheang. Significance of melt-fraction in HVOF sprayed hydroxyapatite particles, splats, and coatings. *Biomaterials*, 25:1177-1186, 2004.

[7] R Hui, Z Wang, O Kesler, L Rose, J Jankovic, S Yick, R Maric, and D Ghosh. Thermal plasma spraying for SOFCs: applications, potential advantages, and challenges. *Journal of Power Sources*, 170:308-323, 2007.

[8] LC Casteletti, AL Neto, and GE Totten. HVOF production of hard chromium substitution coatings for improved wear. *Industrial Heating*, 75:53-57, 2008.

[9] H Herman, S Sampath, and R McCune. Thermal Spray: current status and future trends. MRS Bulletin, 25:17-25, 2000.

[10] L Pawlowski. The Science and Engineering of Thermal Spray Coatings. John Willey & Sons, Chcichester, England, 1985.

[11] H Bick and W Jurgens. Advanced high velocity thermal spraying of metallic and ceramic powders. *DVS Berichte*, 80:92-94, 1983.

[12] H Kreye, D Fandrich, HH Muller, and G Reingers. Microstructure and bond strength of WC-Co coatings deposited by hypersonic flame spraying (Jet-Kote process). *Proceedings of 11th International Thermal Spraying Conference*, 121-128, 1986.

[13] KV Rao, DA Somerville, and DA Lee. Properties and characterization of coatings made using Jet Kote Thermal Spray Technique. *Proceedings of 11th International Thermal Spraying Conference*, 873-888, 1986.

[14] RC Tucker. Thermal Spray Coatings. *Surface Engineering American Society Materials Handbook*, 5:497-501, 1994.

[15] RC Tcuker. Plasma and detonation gun deposition techniques and coating properties. Deposition Technologies for Films and Coatings. Noyes Publications, New Jersey, 454-489.

[16] R Bolot, MP Planche, H Liao, and C Coddet. A three-dimensional model of the wire-arc spray process and its experimental validation. *Journal of Materials Processing Technology*, 200:94-105, 2008.

[17] RP Krepski. Thermal Spray Coating Applications in the Chemical Process Industries, The Materials Technology Institute of the Chemical Process Industries Inc., Georgetown, 1993.

[18] D Zhang, SJ Harris, and DG McCartney. Microstructure formation and corrosion behaviour in HVOF-sprayed Inconel 625 coatings. *Materials Science and Engineering,* 344: 45-56, 2003.

[19] M Friis, C Persson, and J Wigren. Influence of particle in-flight characteristics on the microstructure of atmospheric plasma sprayed yttria stabilized ZrO_2. *Surface and Coatings Technology,* 141:115-27, 2001.

[20] M Vardelle, A Vardelle, AC Leger, P Fauchais, and D Gobin. Influence of article parameters at impact on splat formation and solidification in plasma spraying processes. *Journal o f Thermal Spray Technology,* 4:50-58, 1994.

[21] NZ Mehdizadeh, M Lamontagne, C Moreau, S Chandra, and J Mostaghimi. Photographing impact of molten molybdenum particles in a plasma Spray. *Journal of Thermal Spray Technology,* 14: 354-361, 2005.

[22] HR Salimijazi, L. Pershin, TW Coyle, J Mostaghimi, S Chandra, YC Lau, L Rosenzweig, and E Moran. Effect of droplet characteristics and substrate surface topography on the final morphology of plasma-sprayed zirconia single splats. *Journal of Thermal Spray Technology,* 16:291-299, 2007.

[23] S Sampath and H Herman. Rapid solidification and microstructure development during plasma spray deposition. *Journal of Thermal Spray Technology,* 5:445-456, 1996.

[24] TS Sidhu, S Prakash, and RD Agrawal. Characterization of NiCr wire coatings on Ni and Fe-based superalloys by the HVOF process. *Surface & Coatings Technology*, 200: 5542-5549, 2006.

[25] VL Tellkamp, ML Lau, A Fabel, and EJ Lavernia. Thermal spraying of nanocrystalline Inconel 718. *Nanostructured Materials*, 9:489-492, 1997.

[26] C Verdon, A Karimi, and JL Martin. A study of high velocity oxy-fuel thermally sprayed tungsten carbide based coatings, Part 1: Microstructures. *Materials Science and Engineering*, 246:11-24, 1998.

[27] E Lugscheider, C Herbst, and L Zhao. Parameter studies on high-velocity oxy-fuel spraying of MCrAlY coatings. *Surface and Coatings Technology*, 108–109:16-23, 1998.

[28] J Kawakita, H Katanoda, M Watanabe, K Yokoyama, and S Kuroda. Warm Spraying: An improved spray process to deposit novel coatings. *Surface & Coatings Technology*, 202:4369-4373, 2008.

[29] JM Guilemany, JM de Paco, J Nutting, and JR Miguel. Characterization of the W_2C phase formed during the high velocity oxygen fuel spraying of a WC + 12 pct Co powder. *Metallurgical and Materials Transactions*, 30:1913-1921, 1999.

[30] S Deshpande, T Sampath, and H Zhang. Mechanisms of oxidation and its role in microstructural evolution of metallic thermal spray coatings - Case study for Ni–Al. *Surface & Coatings Technology*, 200:5395-5406, 2006.

[31] J He, M. Ice, and E Lavernia. Particle melting behavior during high-velocity oxygen fuel thermal spraying. *Journal of Thermal Spray Technology*, 10:83-93, 2001.

[32] T Kazumi, H Yoshio, and CJ Li. Splat formation and stacking behavior of particles in high velocity oxygen-fuel spraying of WC-Co coatings. *Journal of the Japan Institute of Metals*, 59:1130-1135, 1995.

[33] CJ Li, YY Wang, GJ Yang, A Ohmori and KA Khor. Effect of solid carbide particle size on deposition behaviour, microstructure and wear performance of HVOF cermet coatings Materials. *Science and Technology*, 20:1087-1096, 2004.

[34] H Jones. Cooling, freezing and substrate impact of droplets formed by rotary atomization. *Journal of Physics D: Applied Physics*, 4:1657-1660, 1971.

[35] F.H Harlow and JP Shannon. The splash of a liquid droplet. *Journal of Applied Physics*, 38:3855-3866, 1967.

[36] K Tsurutani, M Yao, J Senda, and H Fujimoto. Numerical analysis of the deformation process of a droplet impinging upon a wall. *JSME International Journal, Series 2: Fluids Engineering, Heat Transfer, Power, Combustion, Thermophysical Properties*, 33:555-561,1990.

[37] G Trapaga and J Szekely. Mathematical modeling of the isothermal impingement of liquid droplets in spraying processes, *Metallurgical Transactions B*, 22:901-914, 1991.

[38] H Liu, EJ Lavernia, and RH Rangel. Numerical simulation of substrate impact and freezing of droplets in plasma spray processes. *Journal of Physics D*, 26: 1900-1908, 1993.

[39] DB Kothe, CR Mjolsness, and MD Torrey. RIPPLE: a computer program for incompressible flow with free surfaces. Los Alamos National Laboratory. Technicalreport, LA-12007-MS, 1991.

[40] M Pasandideh-Fard, YM Qiao, S Chandra, and J Mostaghimi. Capillary effects during droplet impact on a solid surface. *Physics of Fluids*, 8: 650-659,1996.

[41] Z Zhao, D Poulikakos, and J Fukai. Heat transfer and fluid dynamics during the collision of a liquid droplet on a substrate - I. Modeling. *International Journal Heat Mass Transfer*, 39: 2791–2802, 1996.

[42] J Fukai, Y Shiiba, T Yamamoto, O Miyatake, D Poulikakos, CM Megaridis, and Z Zhao. Wetting effects on the spreading of a liquid droplet colliding with a flat surface: experiment and modeling. *Physics of Fluids*, 7:236-247, 1995.

[43] JM Waldvoge and D Poulikakos. Solidification phenomena in picoleter size solder droplet deposition on a composite substrate. *International Journal Heat Mass Transfer*, 40:295-309, 1997.

[44] M Bussmann, J Mostaghimi, and S Chandra. On a three-dimensional volume tracking model of droplet impact. *Physics of Fluids*, 11: 1406-1417, 1999.

[45] CW Hirt and BD Nichols. Volume of fluid (VOF) method for the dynamics of free boundaries. *Journal of Computational Physics*, 39:201-225, 1981.

[46] CS Peskin. Numerical analysis of blood flow in the heart. *Journal of Computational Physics*, 25: 220 1977.

[47] CS Peskin. The fluid dynamics of heart valves: Experimental, theoretical, and computational methods. *Annual Review of Fluid Mechanics*, 14:235, 1982.

[48] R Mittal and G Iaccarino. Immersed Boundary Methods. *Annual Review of Fluid Mechanics*, 37:239-61, 2005.

[49] D Goldstein, R Handler, and L Sirovich. Modeling a no-slip flow boundary with an external force field. *Journal of Computational Physics*, 105: 354-366, 1993.

[50] EM Saiki and S Biringen. Numerical simulation of a cylinder in uniform flow: Application of a virtual boundary method. *Journal of Computational Physics*, 123: 450-465, 1996.

[51] J Kim, D Kim, and H Choi. An Immersed-Boundary Finite-Volume Method for Simulations of Flow in Complex Geometries. *Journal of Computational Physics*, 171:132-150, 2001.

[52] EA Fadlun, R Verzicco, P Orlandi, and J Mohd-Yusofz. Combined Immersed-Boundary Finite-Difference Methods for Three-Dimensional Complex Flow Simulations. *Journal of Computational Physics*, 161:35-60, 2000.

[53] Markus Uhlmann. An immersed boundary method with direct forcing for the simulation of particulate flows. *Journal of Computational Physics*, 209: 448-476, 2005.

[54] K. Tsurutani, M. Yao, J Senda, and H Fujimoto, Numerical analysis of the deformation process of a droplet impinging upon a wall. *JSME International Journal, Series 2: Fluids Engineering, Heat Transfer, Power, Combustion, Thermophysical Properties*, 33:555-561, 1990.

[55] CS Peskin. Flow patterns around heart valves: a digital computer method for solving the equations of motion. *IEEE Transactions on Biomedical Engineering BME*, 20:316-317, 1973.

[56] RP Beyer and RJ Leveque. Analysis of a one-dimensional model for the immersed boundary method. *SIAM Journal on Numerical Analysis*, 29:332-364, 1992.

[57] MC Lai and CS Peskin. An immersed boundary method with formal second-order accuracy and reduced numerical viscosity. *Journal of Computational Physics*, 160:705-719, 2000.

[58] M Lucente. A numerical study of axisymmetric droplet impact of a shear thinning fluid. M.A.Sc. thesis. Graduate Department of Mechanical and Industrial Engineering, Unversity of Toronto, 2006.

CHAPTER 2

MATHEMATICAL MODEL

2.1 Mathematical Model

This chapter describes the mathematical model for axisymmetric impact of a Newtonian drop on a solid substrate, where the drop contains a solid core. The governing fluid equations are the continuity and conservation of momentum equations:

$$\nabla \cdot \vec{u} = 0 \tag{2.1}$$

$$\frac{\partial(\rho\vec{u})}{\partial t} = -\nabla \cdot (\rho\hat{u}\vec{u}) + \nabla \cdot \vec{\tau} - \nabla p + \rho\vec{g} + \vec{F}_{ST} + \vec{f}_{IB} \tag{2.2}$$

where $\vec{u}$ is the velocity vector, t is time, ρ is density, P is pressure, $\vec{g}$ is the gravity vector, $\vec{F}_{ST}$ is the surface tension force, $\vec{f}_{IB}$ is the immersed boundary force to enforce the no-slip boundary condition at the solid-liquid interfaces, and $\vec{\tau}$ is the viscous stress tensor:

$$\vec{\tau} = \mu\left(\nabla\vec{u} + \nabla\vec{u}^T\right)$$

where μ is the fluid viscosity. In axisymmetric coordinates:

$$\vec{\tau} = \begin{bmatrix} \tau_{rr} & \tau_{rz} & 0 \\ \tau_{zr} & \tau_{zz} & 0 \\ 0 & 0 & \tau_{\theta\theta} \end{bmatrix} = \mu \begin{bmatrix} 2\dfrac{\partial u}{\partial r} & \left(\dfrac{\partial u}{\partial z} + \dfrac{\partial v}{\partial r}\right) & 0 \\ \left(\dfrac{\partial u}{\partial z} + \dfrac{\partial v}{\partial r}\right) & 2\dfrac{\partial v}{\partial z} & 0 \\ 0 & 0 & \dfrac{2u}{r} \end{bmatrix} \tag{2.3}$$

The components of the stress tensors are as shown in Figure 1:

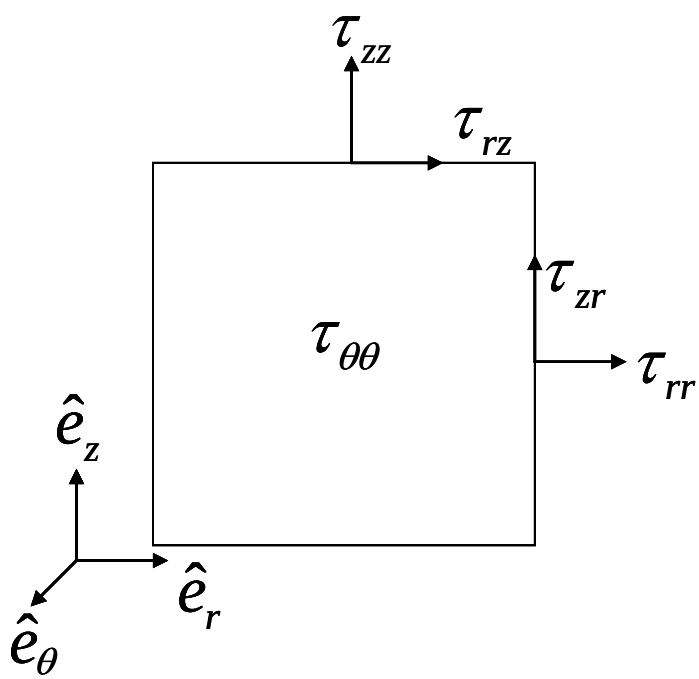

Figure 1 Viscous stress tensors in axisymmetric coordinates

and the divergence of $\vec{\tau}$ is:

$$\nabla \cdot \vec{\tau} = \left[\frac{1}{r} \frac{\partial \left(r\tau_{rr} \right)}{\partial r} + \frac{\partial \tau_{rz}}{\partial z} - \frac{\tau_{\theta\theta}}{r} \right] \hat{e}_r + \left[\frac{1}{r} \frac{\partial \left(r\tau_{rz} \right)}{\partial r} + \frac{\partial \tau_{zz}}{\partial z} \right] \hat{e}_z \tag{2.4}$$

where $\hat{e}_r$ and $\hat{e}_z$ are the unit vectors in the r and z directions.

A function f is used to track the liquid interface. $f = 1$ indicates one fluid, and $f = 0$ indicates the other fluid. This scalar field of f is advected with the flow:

$$\frac{Df}{Dt} = \frac{\partial f}{\partial t} + \left(\vec{u} \cdot \nabla f \right) = 0 \tag{2.5}$$

The surface tension force is treated as a body force using the continuum surface force (CSF) model of Brackbill et al. [1]:

$$\vec{F}_{ST} = \sigma \int_S \kappa \hat{n} \delta dS \tag{2.6}$$

where σ is the surface tension coefficient, κ is the curvature, $\hat{n}$ is the unit normal vector to the fluid interface, δ is the Dirac delta function, and S represents the interface surface.

The immersed boundary force $f_{IB}\left(\vec{x},t\right)$ is also treated as a body force using the direct forcing model of Uhlmann [2]. Its value is determined by first calculating the Lagrangian counterpart of the boundary force, $\vec{F}_{IB}\left(s,t\right)$, at each forcing point, $\vec{X}\left(s,t\right)$, on the immersed boundary. Then, $\vec{F}_{IB}\left(s,t\right)$ is transferred onto the Eulerian mesh points:

$$f_{IB}\left(\vec{x},t\right) = \int_0^L F_{IB}\left(s,t\right) \delta\left(\vec{x} - \vec{X}\left(s,t\right) \right) ds \tag{2.7}$$

where L is the length of the immersed boundary, $0 \le s \le L$, δ is the Dirac delta function, and $\vec{X}(s,t)$ is the positions of a forcing point at a given time t.

2.2 Boundary Conditions

The governing equations are subject to boundary conditions (BC) at solid walls, symmetry planes, inlet boundaries, and outlet boundaries. Two types of BC are available: the Neumann type and the Dirichlet type. The Dirichlet type specifies the boundary values directly, and the Neumann type specifies the gradients of boundary values.

At a solid wall, no fluid can be transferred across a wall, and the fluid is at rest at the wall, the no-slip boundary condition. The boundary conditions for velocities and velocity gradients at a stationary wall are:

$$\vec{u}_{wall} = (u,v) = (0,0) \tag{2.8}$$

Equation 2.10 leads to zero normal stress at a solid wall.

In axisymmetric coordinates, $r = 0$ is a symmetry line, across which no fluid can be transferred, and the free-slip boundary condition is applied:

$$\vec{u}_{sym} = (u,v) = (0, v_{sym}) \tag{2.9}$$

$$\left(\frac{\partial v}{\partial r}\right)_{sym} = 0 \tag{2.10}$$

At an inlet boundary, an inlet velocity is specified across the boundary:

$$\vec{u}_{inlet} = \vec{U}_{inlet} \tag{2.11}$$

At an outlet boundary, we assume velocity gradients are zero.

Finally, at a contact line, where two fluids meet at a solid substrate, the contact angle, θ, is specified (see Figure 2), that depends on the fluid and solid materials.

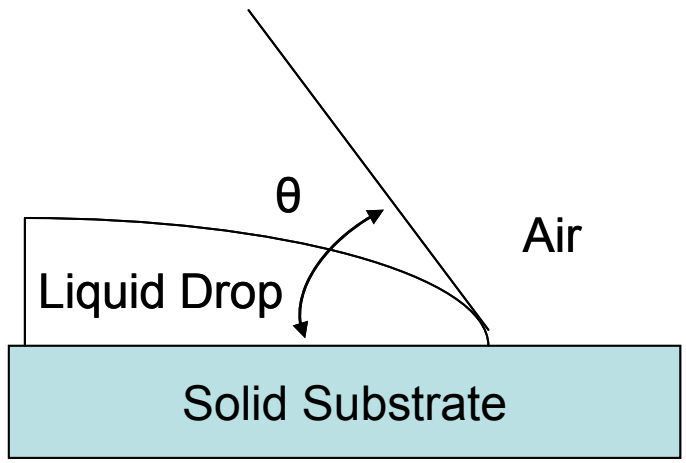

Figure 2- Static contact angle at the liquid-gas interface at a solid substrate

References

[1] JU Brackbill, DB Kothe, and C Zemach. A continuum method for modeling surface tension. *Journal of Computational Physics*, 100:335-354, 1992.

[2] M Uhlmann. An immersed boundary method with direct forcing for the simulation of particulate flows. *Journal of Computational Physics*, 209:448-476, 2005.

CHAPTER 3

NUMERICAL MODEL

3.1 Numerical Model

An immersed boundary scheme was implemented on the fluid flow model developed by Lucente [1] to simulate fluid flow around a solid core during a semi-molten drop impact. In Lucente's flow model, the liquid interface was tracked by the "Volume of Fluid" method (VOF), and the surface tension was treated with the continuum surface force model (CSF). In this chapter, the focus is on the implementation of the "Immersed Boundary method" (IB).

The code was developed in 2D axisymmetric cylindrical coordinates with a fixed Eulerian mesh. A typical numerical domain imposed with the immersed boundary is shown in Figure 1. The code solves for flow based on a finite-volume method. The cylindrical discretization for each control volume is shown Figure 2.

The momentum equation (Equation 2.2) is discretised using a two-step projection method that separates Equation 2.2 into two equations (Equation 3.1 and Equation 3.6) which are

solved in succession, once per timestep $\Delta t = t^{n+1} - t^n$. In the first step, an interim velocity $\vec{u}'$ is explicitly calculated from the convective flux, viscous flux and pressure at the time t^n level:

$$\frac{\left(\rho\vec{u}'\right)-\left(\rho\vec{u}^n\right)}{\Delta t} = \underbrace{-\nabla\cdot\left(\rho\hat{u}\vec{u}\right)^n + \nabla\cdot\tau^n - \nabla p\big|_c^n}_{rhs^n} \tag{3.1}$$

The $\vec{u}'$ field does not satisfy the no-slip BC at the immersed boundary. To take the presence of the immersed boundary into account, an Eulerian boundary force is calculated with the following Equations 3.2 to 3.4.

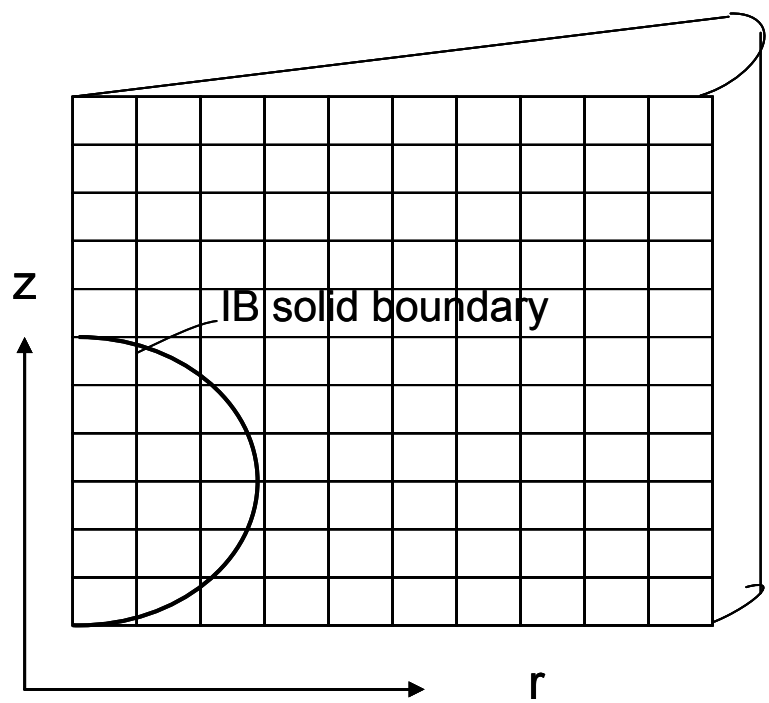

Figure 1- Schematic of the mesh and the immersed boundary imposed inside the numerical domain

For the mth Lagrangian force point, located inside the center cell (i, j) of a 3×3 stencil (see Figure 3), the $\vec{u}'$ field is transferred via the δ Dirac delta function:

$$\vec{U}_m^{'}\left(\vec{X}_m\right) = \sum_{l,k=-1}^{1} \vec{u}_{i+l,j+k}^{'}\delta\left(\vec{x}_{i+l,j+k} - \vec{X}_m\right)\Delta V_{i+l,j+k},\ 1 \le m \le nB \tag{3.2}$$

where $\vec{U}_m^{'}$ is the interpolated velocity at the mth force point, $\vec{X}_m$ is the coordinate of the mth force point, ΔV is the Eulerian cell volume, and nB is the total number of Lagrangian force points.

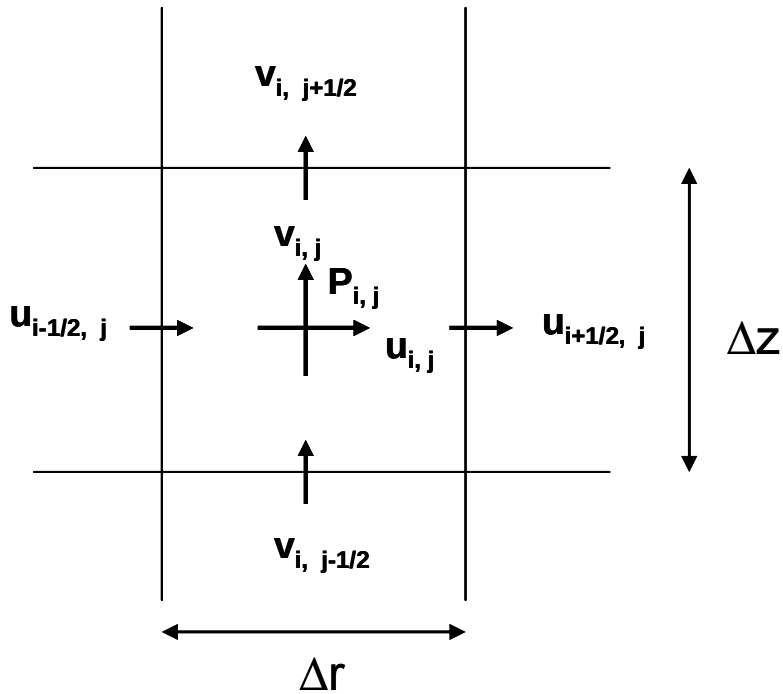

Figure 2- Positions of flow variables in each control volume, and index conventions

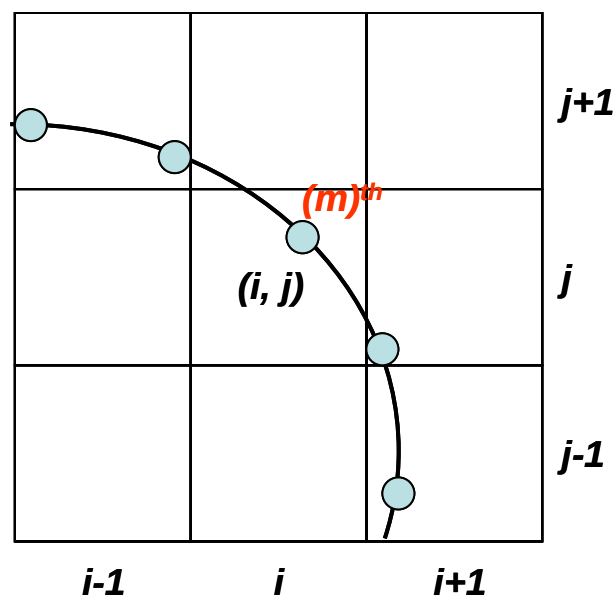

Figure 3- m^{th} Lagrangian force point located inside the center cell (*i,j*) of a 3 X 3 stencil

$\vec{U}_m^{'}$ is an estimated fluid velocity that is interpolated from the surrounding cells. To impose a desired value of fluid velocity at the mth force point, a direct force term is calculated as:

$$\vec{F}_{IB}^{m} = \rho \frac{\left(\vec{U}_m^{d} - \vec{U}_m^{'}\right)}{\Delta t} \tag{3.3}$$

where $\vec{F}_{IB}^{m}$ is the mth Lagrangian immersed boundary force, $\vec{U}_m^{d}$ is the mth desired velocity, ρ is the fluid density, and Δt is the timestep.

After $\vec{F}_{IB}^{m}$ is calculated, it is transferred back to the surrounding cells inside the same stencil from which $\vec{U}_m^{'}$ is interpolated. The transfer is done via the Dirac delta function δ:

$$\vec{f}_{IB}\left(i, j\right) = \sum_{m=1}^{nB} F_{IB}\left(\vec{X}_m\right)\delta\left(\vec{x}_{i+l,\, j+k} - \vec{X}_m\right)\Delta V_m^{L} \tag{3.4}$$

where $\vec{f}_{IB}\left(i, j\right)$ is the Eulerian immersed boundary force inside the stencil and ΔV_m^{L} is the cell volume about the mth force point.

The body forces $\vec{f}_{IB}\left(i, j\right)$ and the surface tension force $\vec{F}_{ST}$ from Equation 2.6 are then added to the $\vec{u}'$ field, and the time t^n level pressure gradient ∇p^n is removed (since ∇p^n was only added to improve the estimate of $\vec{u}'$ before interpolating $\vec{U}_m^{'}$) :

$$\frac{\left(\rho\vec{u}''\right) - \left(\rho\vec{u}_c'\right)}{\Delta t} = \vec{f}_{IB} + \vec{F}_{ST} - \nabla p^n \tag{3.5}$$

The $\vec{u}''$ field is the second estimated fluid velocity, that takes into account the presence of the immersed boundary. Nevertheless, $\vec{u}''$ is not divergence-free yet; it does not satisfy continuity (Equation 2.1). The divergence-free $\vec{u}^{n+1}$ is calculated using Equation 3.6 :

$$\frac{\rho\left(\vec{u}^{n+1}-\vec{u}''\right)}{\Delta t}=-\nabla p^{n+1} \tag{3.6}$$

To solve for the unknown ∇p^{n+1}, Equation 3.6 is combined with Equation 2.1 to yield a Poisson equation:

$$\nabla\cdot\left(\frac{\nabla p^{n+1}}{\rho}\right)=-\frac{\nabla\cdot\left(\vec{u}''\right)}{\Delta t} \tag{3.7}$$

To summarize, the following algorithm advances the solution from time t^n level to t^{n+1} level, and clarifies how the face-centered (fc) and the cell-centered (cc) velocities are used:

1. Initialize time t^n level velocities $\vec{u}_{cc}^{n}$ and $\vec{u}_{fc}^{n}$.
2. Calculate f^{n+1} via Equation 2.5.
3. Calculate the first estimate of the $\vec{u}_{cc}'$ field via Equation 3.1.
4. Interpolate $\vec{u}_{cc}'$ to the Lagrangian force points to get $\vec{U}_m'$ via Equation 3.2.
5. Calculate $\vec{f}_{IB}$ via Equation 3.4.
6. Add $\vec{f}_{IB}$ and $\vec{F}_{ST}$ to $\vec{u}_{cc}'$, and remove ∇p^n from it to obtain the second estimate of the $\vec{u}_{cc}''$ field via Equation 3.5.
7. Interpolate the cell-centered $\vec{u}_{cc}''$ to the face-centered $\vec{u}_{fc}''$ using the van Leer algorithm [2].
8. Solve Equation 3.7 for $\underline{P_{cc}^{n+1}}$.

9. Calculate $\underline{\nabla p_{fc}^{n+1}}$ and average to cell centers to obtain $\underline{\nabla p_{cc}^{n+1}}$.
10. Calculate $\vec{u}_{cc}{}^{n+1}$ and $\vec{u}_{fc}{}^{n+1}$ via Equation 3.6.

The following sections describe in details how each term in the momentum equation is evaluated except the surface tension term and the volume fraction of liquid interface. This thesis focused on the implementation of the "Immersed Boundary method" (IB).

3.2 Convective Flux

The convective term of Equation 2.2 is transformed from a volume integral to a surface integral using Gauss theorem:

$$\int_V \nabla \cdot \left(\rho \hat{u} \vec{u}\right) dV = \int_S \left(\rho \hat{u}\right) \vec{u} \cdot \vec{n}_A dS \tag{3.8}$$

where $\left(\rho \hat{u}\right)$ is the mass flux across a surface area S, $\vec{u}$ is the convected velocity (momentum per unit mass) across S, and $\vec{n}_A$ is the unit vector to S. In discrete form, consider conservation of the v component of momentum in the cell $\left(i, j\right)$:

$$\begin{aligned}\int_S \left(\rho \hat{u}\right) \vec{u} \cdot \vec{n}_A dS \approx & \left(\rho u_{i+1/2,j}\right)\left(v_{i+1/2,j}^{conv}\right) - \left(\rho u_{i-1/2,j}\right)\left(v_{i-1/2,j}^{conv}\right) \\ & + \left(\rho v_{i,j+1/2}\right)\left(v_{i,j+1/2}^{conv}\right) - \left(\rho v_{i,j-1/2}\right)\left(v_{i,j-1/2}^{conv}\right)\end{aligned} \tag{3.9}$$

where the mass fluxes $\left(\rho \hat{u}\right)$ are calculated by the volume tacking algorithm [3], and the v^{conv} terms are the convected velocities across cell faces. For cell faces that contain segments of the fluid interface, values of v^{conv} are calculated by a first order upwinding scheme. For cell faces away from an interface, v^{conv} is calculated using the second order upwinding scheme of van Leer [2].

3.3 Viscous Diffusion

The r-component and z-component of the viscous term $(\nabla \cdot \tau)$ in Equation 2.2 are discretized using Gauss theorem:

$$\begin{aligned}\int (\nabla \cdot \tau)_r \, dV &= \int_{i-1/2,j}^{i-1/2,j} \tau_{rr} dA + \int_{i,j-1/2}^{i,j+1/2} \tau_{rz} dA - \int_{i,j} \frac{\tau_{\theta\theta}}{r} dV \\ &= \left(2A\mu \frac{\partial u}{\partial r} \right)\Bigg|_{i+1/2,j} - \left(2A\mu \frac{\partial u}{\partial r} \right)\Bigg|_{i+1/2,j} \\ &+ \left(A\mu \left(\frac{\partial u}{\partial z} + \frac{\partial v}{\partial r} \right) \right)\Bigg|_{i,j+1/2} - \left(A\mu \left(\frac{\partial u}{\partial z} + \frac{\partial v}{\partial r} \right) \right)\Bigg|_{i,j-1/2} - \left(2V \frac{\mu u}{r^2} \right)\Bigg|_{i,j}\end{aligned} \tag{3.10}$$

$$\begin{aligned}\int (\nabla \cdot \tau)_z \, dV &= \int_{i-1/2,j}^{i+1/2,j} \tau_{zr} dA + \int_{i,j-1/2}^{i,j+1/2} \tau_{zz} dA \\ &= \left(A\mu \left(\frac{\partial u}{\partial z} + \frac{\partial v}{\partial r} \right) \right)\Bigg|_{i+1/2,j} - \left(A\mu \left(\frac{\partial u}{\partial z} + \frac{\partial v}{\partial r} \right) \right)\Bigg|_{i-1/2,j} \\ &+ \left(2A\mu \frac{\partial v}{\partial z} \right)\Bigg|_{i,j+1/2} - \left(2A\mu \frac{\partial v}{\partial z} \right)\Bigg|_{i,j-1/2}\end{aligned} \tag{3.11}$$

The evaluation of all terms except $2V\mu u / r^2$ requires evaluation of velocity gradients at faces. The following two derivatives must be evaluated at each face: $\partial u / \partial z$ and $\partial v / \partial r$. In addition, $\partial u / \partial r$ must be evaluated at east faces (or west faces), and $\partial v / \partial z$ must be evaluated at north faces (or south faces). The derivatives normal to a face are evaluated in a straightforward manner from the cell-centered velocities:

$$\left(\frac{\partial u}{\partial r} \right)\Bigg|_{i+1/2,j} \approx \frac{u_{i+1,j} - u_{i,j}}{\Delta r} \tag{3.12}$$

$$\left(\frac{\partial u}{\partial z} \right)\Bigg|_{i,j+1/2} \approx \frac{u_{i,j+1} - u_{i,j}}{\Delta z} \tag{3.13}$$

$$\left(\frac{\partial v}{\partial r}\right)\bigg|_{i+1/2,\,j} \approx \frac{v_{i+1,\,j} - v_{i+1,\,j}}{\Delta r} \tag{3.14}$$

$$\left(\frac{\partial v}{\partial z}\right)\bigg|_{i,\,j+1/2} \approx \frac{v_{i,\,j+1} - v_{i,\,j}}{\Delta z} \tag{3.15}$$

Finally, the derivatives tangent to a face are calculated from the face-centered velocities:

$$\left(\frac{\partial u}{\partial z}\right)\bigg|_{i+1/2,\,j} \approx \frac{u_{i+1/2,\,j+1} - u_{i+1/2,\,j-1}}{2\Delta z} \tag{3.16}$$

$$\left(\frac{\partial v}{\partial r}\right)\bigg|_{i,\,j+1/2} \approx \frac{v_{i+1,\,j+1/2} - v_{i-1,\,j+1/2}}{2\Delta r} \tag{3.17}$$

3.4 Immersed Boundary

The purpose of the immersed boundary method provides a means of imposing a solid object of any shape onto a fixed Eulerian grid. The flow then “feels” the object due to an extra forcing term on the momentum equation.

The immersed boundary is tracked by a set of massless force points, which do not necessarily coincide with the Eulerian gridpoints. For the present work, the positions of the Lagrangian force points are evenly spread out on the hemispherical surface of a solid core with a constant angle $\Delta\theta$, see Figure 4:

$$\Delta\theta = \frac{\pi}{nB - 1} \tag{3.18}$$

where nB is the total number of force points on the immersed boundary.

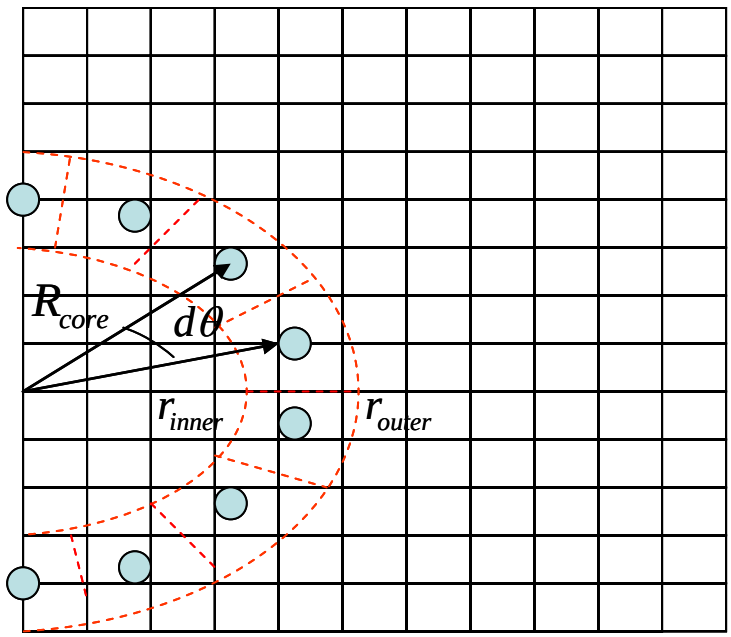

Figure 4- Lagrangian force points and the associated control volumes distributed over the hemisphere's surface

The value of nB depends on the solid core radius R_{core} and the Eulerian mesh size h (a uniform mesh size is used in present work), and is calculated by equating the cross section area of the Lagrangian control volume, $(\delta s)(r_{outer} - r_{innner})$, with the Eulerian mesh area, h^2:

$$(\delta s)(r_{outer} - r_{innner}) = h^2 \tag{3.19}$$

where δs is the arc length of the control volume calculated as $\delta s = \pi R_{core} / (nB - 1)$, and r_{outer} and r_{innner} are the outer and inner radii of the control volume, respectively. Since it is assumed that the radial width is the same as the Eulerian mesh size, i.e., $r_{outer} - r_{inner} = h$, Equation 3.19 is modified as:

$$nB = \begin{cases} \dfrac{\pi R_{core}}{h} + 2, \text{ if } \dfrac{\pi R_{core}}{h} \geq 0.5 \\ \dfrac{\pi R_{core}}{h} + 1, \text{ if } \dfrac{\pi R_{core}}{h} \leq 0.5 \end{cases} \tag{3.20}$$

Equation 3.20 states that nB is directly proportional to R_{core} and inversely proportional to h. In addition, $(\pi R_{core}/h)$ is not necessarily an integer value; if the fractional part of the value exceeds 0.5, an extra force point is added.

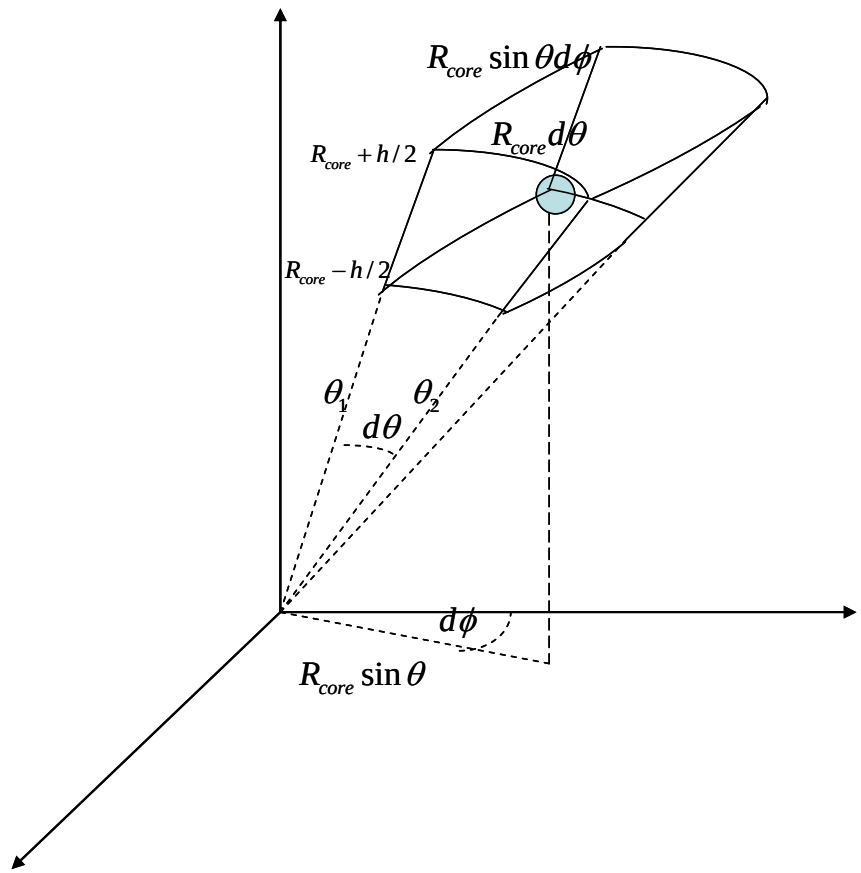

Figure 5- An infinitesimal volume of a spherical shell in spherical coordinates

Each Lagrangian force point is associated with a cell volume, ΔV_m^L. In axisymmetric coordinates the volume of ΔV_m^L increases in the radial direction. Properly sizing ΔV_m^L is important since the immersed boundary force $\vec{F}_{IB}^m$ is later multiplied by ΔV_m^L to obtain the corresponding body force. ΔV_m^L is derived from the volume integration of an infinitesimal spherical shell (see Figure 5) in spherical coordinates (r,θ,ϕ):

$$\begin{aligned}\Delta V_l &= \int_r \int_\phi \int_\theta \left(r \sin\theta d\phi\right)\left(r d\theta\right)\left(dr\right) \\ &= \int_{r=R_{core}-h/2}^{r=R_{core}+h/2} \int_{\phi=0}^{2\pi} \int_{\theta_1}^{\theta_2} r^2 \sin\theta d\theta d\phi dr \\ &= \frac{2}{3}\pi\left(\cos\theta_1 - \cos\theta_2\right)\left[\left(R_{core}+h/2\right)^3 - \left(R_{core}-h/2\right)^3\right]\end{aligned} \tag{3.21}$$

3.4.1 Two-Dimensional Dirac Delta function

The 2D Dirac delta function δ of Roma et al. [4] was employed to transfer variable properties between the Lagrangian force points and the Eulerian grid, see Equation 3.2 and Equation 3.4. The δ function was modified to accommodate the axisymmetric coordinates, and it was approximated by the product of the 1D delta functions δ_h^1 in the r and z directions, respectively:

$$\delta\left(\bar{x}_{i,j} - \bar{X}_m\right) = \frac{\delta_h^1\left(r_{i,j} - R_m\right)\delta_h^1\left(z_{i,j} - Z_m\right)}{\Delta V_{i,j}} \tag{3.22}$$

where $\left(r_{i,j}, z_{i,j}\right)$ and $\left(R_m, Z_m\right)$ are the cylindrical coordinates of the Eulerian grid points and the Lagrangian force points, respectively, and $\Delta V_{i,j}$ is an Eulerian cell volume.

Both $\delta_h^1\left(r_{i,j} - R_m\right)$ and $\delta_h^1\left(z_{i,j} - Z_m\right)$ are assumed to be smooth functions, and they are calculated by dividing each of these by the Eulerian mesh size h. Consider the *r*-component of δ_h^1:

$$\delta_h^1\left(r - R_m\right) = \phi\left(\frac{r_{i,j} - R_m}{h}\right) \tag{3.23}$$

and,

$$r = \frac{r_{i,j} - R_m}{h} \tag{3.24}$$

where r is the number of cells between the Eulerian grid point and the Lagrangian force point. The ϕ function is approximated based on r as:

$$\phi(r) = \begin{cases} \frac{1}{6}\left[5 - |3| - \sqrt{-3(1-|r|)^2 + 1}\right], 0.5 \le |r| \le 1.5 \\ \frac{1}{3}\left(1 + \sqrt{-3r^2 + 1}\right), |r| \le 0.5 \\ 0, \quad otherwise \end{cases} \tag{3.25}$$

3.5 Pressure

Finally, pressure at time $n+1$ level, $P_{i,j}^{\,n+1}$, is calculated from the Poisson equation (3.7). In discrete form, Equation 3.7 is discretized using Gauss theorem:

$$\frac{1}{\rho}\int_S \nabla_P^{\,n+1} \cdot \hat{n}_A dS = -\frac{1}{\Delta t}\int_A \vec{u}^{\,*} \cdot \hat{n}_A dS \tag{3.26}$$

Expanding Equation 3.26 yields an algebraic equation of the form:

$$a_{i,j} P_{i,j} + \sum_{nb} a_{nb} P_{nb} = b_{i,j} \tag{3.27}$$

where nb indicates the neighboring cells shown in Figure 6, and the coefficients are evaluated as follows:

$$a_{i+1,j} = \left(\frac{A}{\rho \Delta r}\right)_{i+1/2,j} \tag{3.28}$$

$$a_{i-1,j} = \left(\frac{A}{\rho \Delta r} \right)_{i-1/2,j} \tag{3.29}$$

$$a_{i,j+1} = \left(\frac{A}{\rho \Delta z} \right)_{i,j+1/2} \tag{3.30}$$

$$a_{i,j+1/2} = \left(\frac{A}{\rho \Delta z} \right)_{i,j+1/2} \tag{3.31}$$

$$a_{i,j} = -\left(a_{i+1,j} + a_{i-1,j} + a_{i,j+1} + a_{i,j-1} \right) \tag{3.32}$$

$$b = \frac{1}{\Delta t} \left(A_{i+1/2,j} u''_{i+1/2,j} - A_{i-1/2,j} u''_{i-1/2,j} + A_{i,j+1/2} v''_{i,j+1/2} - A_{i,j-1/2} v''_{i,j-1/2} \right) \tag{3.33}$$

The algebraic equations are solved with a Conjugate Gradient solver. Once $P_{i,j}^{\ n+1}$ is solved, it is used to calculate the face-centered pressure gradients:

$$\nabla p_{i+1/2,j}^{n+1} = \frac{P_{i+1,j}^{n+1} - P_{i,j}^{n+1}}{\Delta r} \tag{3.34}$$

$$\nabla p_{i,j+1/2}^{n+1} = \frac{P_{i,j+1}^{n+1} - P_{i,j}^{n+1}}{\Delta z} \tag{3.35}$$

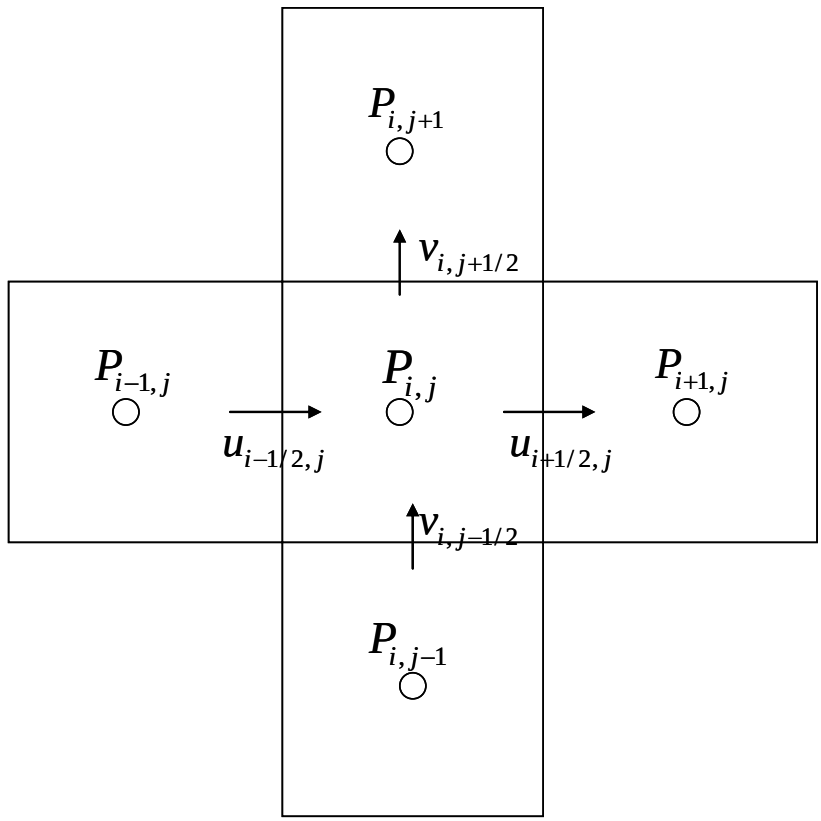

Figure 6- Stencil for the pressure Poisson equation

The z- component of the cell-centered pressure gradients are evaluated by the arithmetic averaging:

$$\left(\nabla p_{i,j}^{n+1}\right)_z = \frac{1}{2}\left(\frac{\nabla p_{i,j+1/2}^{n+1}}{\rho} + \frac{\nabla p_{i,j-1/2}^{n+1}}{\rho}\right) \tag{3.36}$$

The r- component of cell-centered pressure gradients are evaluated by the volume-weighting averaging:

$$\left(\nabla p_{i,j}^{n+1}\right)_r = \frac{\Delta V_{i\to i+1/2,j}}{\Delta V_{i,j}}\frac{\nabla p_{i+1/2,j}^{n+1}}{\rho} + \frac{\Delta V_{i-1/2\to,j}}{\Delta V_{i,j}}\frac{\nabla p_{i-1/2,j}^{n+1}}{\rho} \tag{3.37}$$

where $\Delta V_{i\to i+1/2,j}$ and $\Delta V_{i-1/2\to,j}$ are shown in Figure 7.

Finally, both time $n+1$ face-centered and cell-centered velocities are updated by using Equation 3.6 as follows:

$$u_{i+1/2,j}^{n+1} = u_{i+1/2,j}^{''} - \frac{\Delta t}{\rho} \nabla p_{i+1/2,j}^{n+1} \tag{3.38}$$

$$v_{i,j+1/2}^{n+1} = v_{i,j+1/2}^{''} - \frac{\Delta t}{\rho} \nabla p_{i,j+1/2}^{n+1} \tag{3.39}$$

$$u_{i,j}^{n+1} = u_{i,j}^{''} - \frac{\Delta t}{\rho} \left(\nabla p_{i,j}^{n+1} \right)_r \tag{3.40}$$

$$v_{i,j}^{n+1} = v_{i,j}^{''} - \frac{\Delta t}{\rho} \left(\nabla p_{i,j}^{n+1} \right)_z \tag{3.41}$$

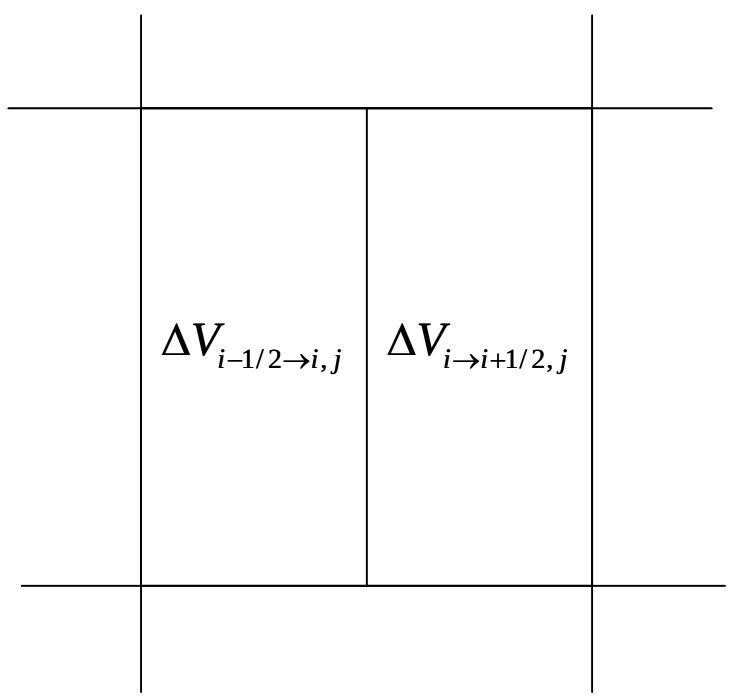

Figure 7- Volume portions of a cell used to do the volume-weighting averaging

References

[1] M Lucente. A numerical study of axisymmetric droplet impact of a shear thinning fluid. M.A.Sc. thesis. Graduate Department of Mechanical and Industrial Engineering, University of Toronto, 2006.

[2] BV Leer. Towards the ultimate conservative divergence scheme. V. A second-order sequel to Godunov's method. *Journal of Computational Physics*, 32:101-136, 1979.

[3] M Bussmann, DB Kothe, and JM Sicilian. Modeling high density ratio incompressible interfacial flows. *American Society of Mechanical Engineers, Fluids Engineering Division*, 257:707-713, 2002.

[4] AM Roma, CS Peskin, and MJ Bergery. An Adaptive Version of the Immersed Boundary Method. *Journal of Computational Physics*, 153:509–534, 1999.

CHAPTER 4

VALIDATION

The following validation tests were completed to ensure that the model was properly implemented.

1) To assess the viscous and convective terms of the model, laminar pipeflow near an entrance region was simulated.

2) To assess the Immersed Boundary algorithm, axisymmetric flow past a stationary sphere in a free-stream was simulated.

4.1 Laminar Pipe Flow

The first validation test was developed to ensure the viscous and convective terms of the model were implemented properly by simulating laminar flow of Newtonian fluid in the inlet region of a circular pipe, assuming the gravitational force was zero. The circular pipe was chosen for this test since the model is built on 2-D cylindrical coordinates. A characteristic number is defined by the diameter of the pipe D D and the fluid properties:

$$Re = \frac{\rho U_o D}{\mu} \tag{4.1}$$

where ρ is the fluid density, U_o is the inlet fluid velocity, and μ is the viscosity. In this case, oil was chosen for this test ($\rho = 888$ [kg/m^3] and $\mu = 0.834$ [kg/m-s]). Figure 1 shows the v- and u- components of velocity near the pipe entrance ($Re = 1.8$). The flow enters the domain from the inlet boundary with a crossflow velocity of $U_o = 0.01 m/s$. The domain size in the $\hat{e}_r$ and $\hat{e}_z$ directions are $0.09m$ and $0.18m$, which correspond to the radius and the length of the pipe, respectively. The flow was solved at a mesh resolution of 80x160. A no-slip boundary was imposed at the top (pipe wall) and an axisymmetric boundary was imposed at the bottom (centerline of the flow). The right and left sides of the domain correspond to the inlet and the outlet boundaries.

The v- velocity field in Figure 1 a) shows that the flow comes in with an inlet velocity of $U_o = 0.01 m/s$. Since fluid immediately encounters the pipe wall after crossing the inlet boundary, fluid is forced to move towards the centerline as shown by the u- velocity field, see Figure 1 b). As fluid moves inward to the pipe, the v-component velocity starts to develop a parabolic profile, and the profile reaches a steady state at $z = 0.1m$.The parabolic profile of the v- velocity at the outlet boundary ($z = 0.18m$) is compared with the well-known analytical solution:

$$v = \left(\frac{P_o - P_L}{L}\right)\left(\frac{R^2}{4\mu}\right)\left[1 - \left(\frac{r}{R}\right)^2\right] \tag{4.2}$$

where R is the pipe radius. As shown in Figure 2, the numerical parabolic velocity profile agrees well with the analytical solution.

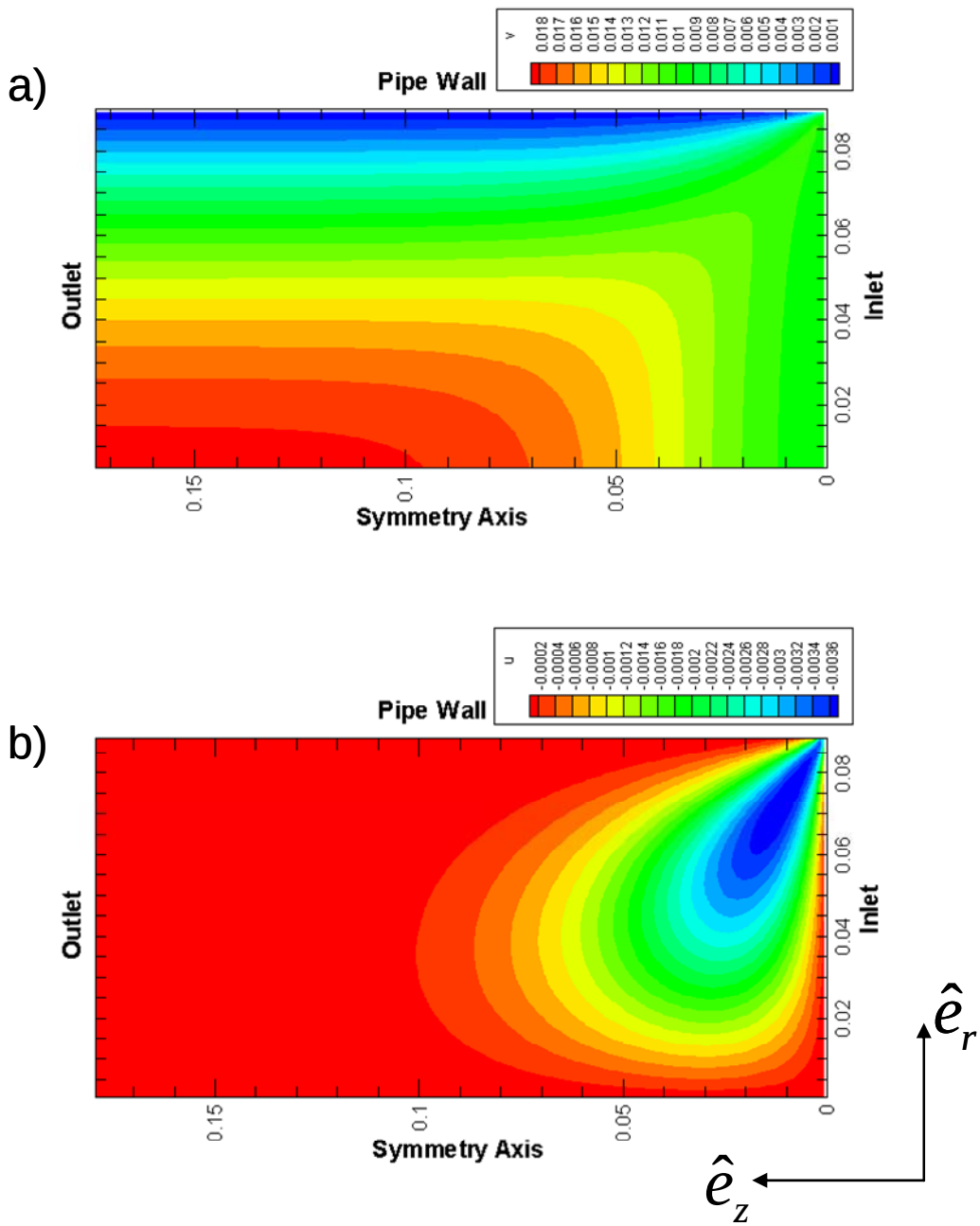

Figure 1- The v -component a) and u -component b) of velocity for viscous pipeflow near the entrance region, *Re*=1.8.

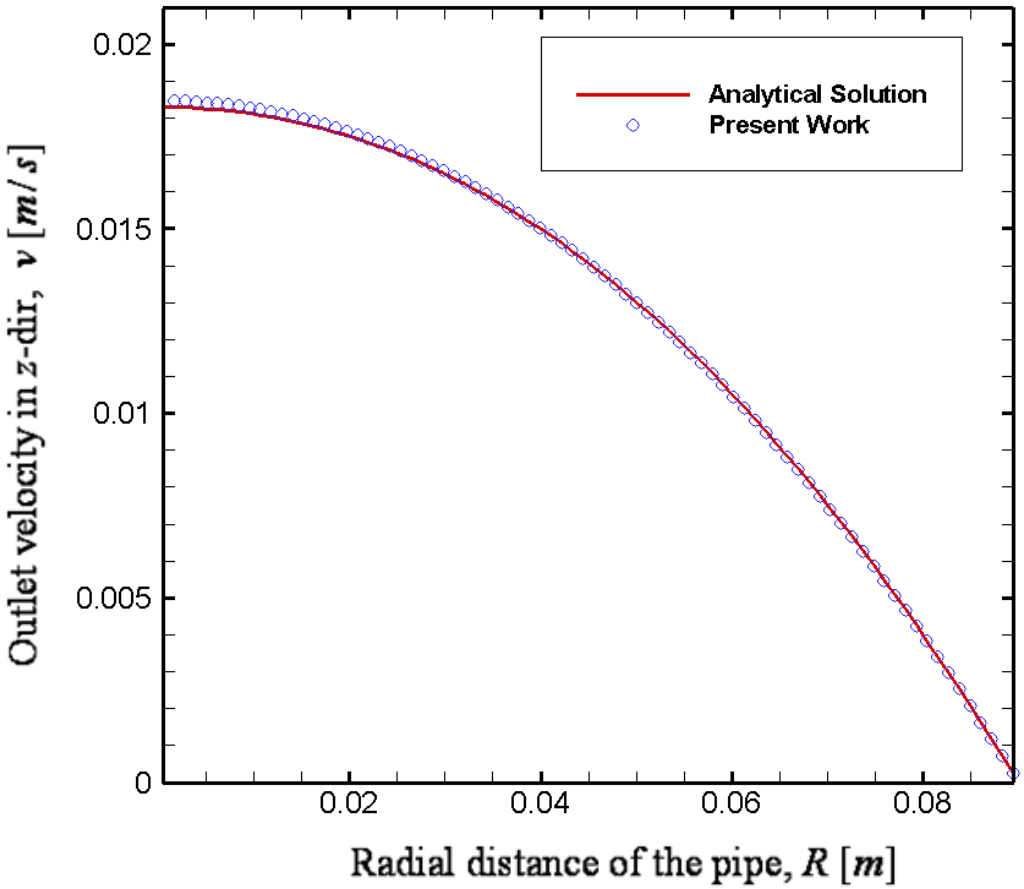

Figure 2- Comparison of the v - velocity profile at the outlet boundary with the analytical solution.

4.2 Axisymmetric Flow Past A Stationary Sphere in Free-Stream

The second validation test was to solve for viscous flow past a sphere in a free stream, in the lower Reynolds number regime, $Re \leq 200$. In this flow regime, the flow remains axisymmetric, as confirmed by several researchers [1,2,3]. The Reynolds number is defined as:

$$Re = \frac{\rho D U_\infty}{\mu} \tag{4.3}$$

where D is the sphere diameter and U_∞ is the free-stream velocity. In this study, the cylindrical coordinate system was employed. To enforce the no-slip boundary condition at the immersed sphere boundary, a set of $nB = 15$ Lagrangian force points were defined at the sphere surface. The simulation was run at a mesh resolution of 80x240. In Figure 3, the fluid enters the domain from the inlet boundary at U_∞ and exits the outlet boundary with the Neumann pressure boundary condition applied. At the top and bottom of the domains, a free-slip boundary condition was imposed, and so that the viscous stress was zero.

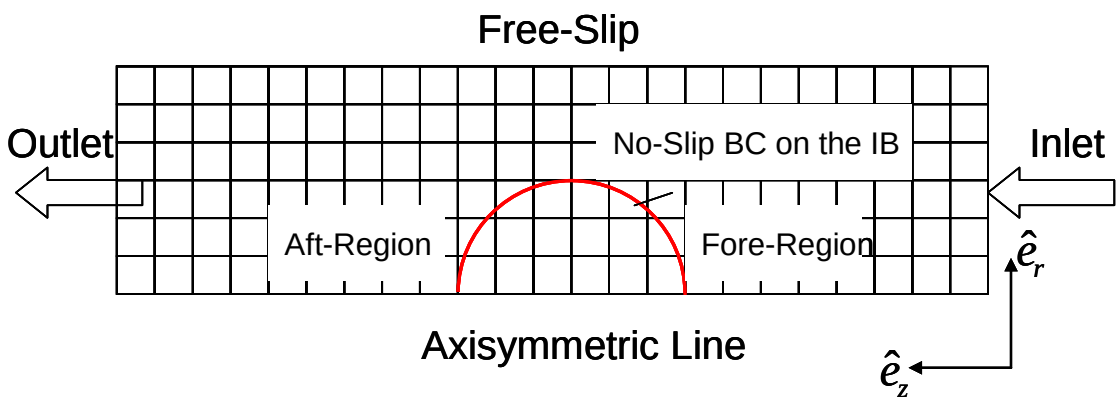

Figure 3- Boundary conditions for flow past a sphere in a free-steam

4.2.1 Axisymmetric Flow Past A Sphere for *Re* ≤ 0.5

The flow past a sphere of $D = 10mm$ at $Re=0.1$ was simulated. The size of the numerical domain was scaled by the sphere radius, R. The domain had a length of $z = 54R$ and a radius of $r = 18R$, and the sphere was located at the halfway point of ($z = 27R$) in the streamwise direction. The u and v velocity components are plotted in Figure 4 (a) and Figure 4 (b), respectively, where the velocity values are normalized by the free-stream velocity U_∞. In both figures, the contour lines of the velocity distributions are symmetric in the fore- and aft- regions of the sphere. In Figure 4 (a), fluid in the fore-region of the sphere is being "pushed out" by the front of the sphere; as the u-component in this

region is positive and increases as fluid approaches the sphere. On the other side, fluid in the aft-region of this is “pulled in” by the rear of the sphere, making the u-component in the aft-region negative; its absolute value decreases with distance from the sphere.

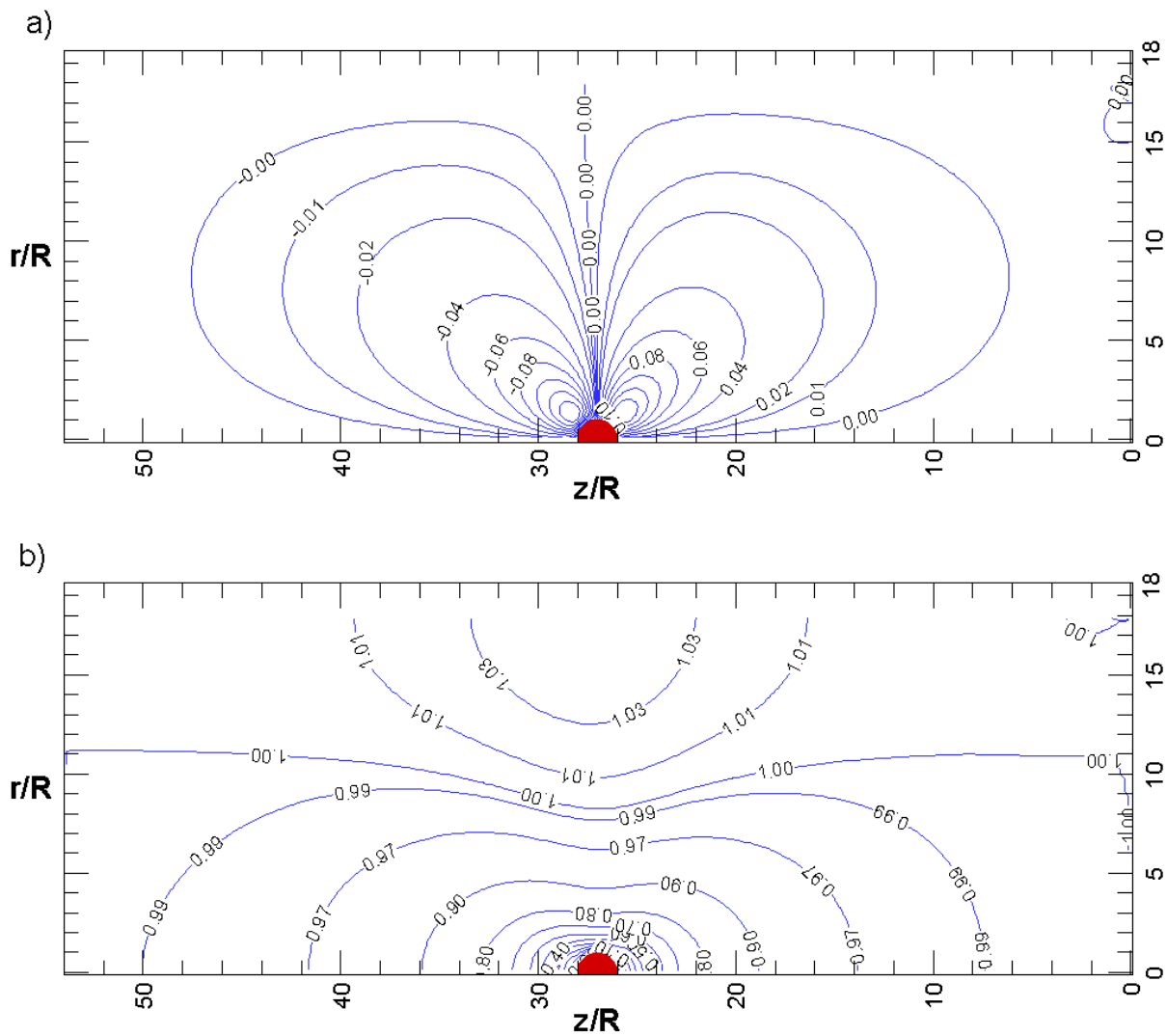

Figure 4- a) u - component and b) v - component velocity fields at *Re*=0.1, normalized by the free stream velocity, U_∞.

In Figure 4 (b), the v- component velocity field in the fore- and aft- regions is plotted. In the fore-region, the v- component decreases as fluid approaches the sphere. In the aft-region, the v- component increases with increasing distance from the rear of the sphere.

To ensure that the velocity fields are correct, the numerical results were compared with the exact solution of Stokes [4] for velocity distributions at low Reynolds numbers, $Re \leq 0.5$, where fluid flow is laminar, and asymmetric along a solid sphere, see Equation 4.4 and Equation 4.5. Stoke's analytical solution is provided in the spherical coordinate system: θ is the angle from the stagnation point in the $\hat{e}_\theta$ direction, and r is the radial distance from the center of the sphere in the $\hat{e}_R$ direction pointing outward, see Figure 5.

$$u_R = V_\infty \times \cos(\theta) \times \left(1 + 0.5\left(\frac{r}{a}\right)^3 - 1.5\left(\frac{r}{a}\right)\right) \text{ in } \hat{e}_R \tag{4.4}$$

$$u_\theta = -V_\infty \times \sin(\theta) \times \left(1 - 0.25\left(\frac{r}{a}\right)^3 - 0.75\left(\frac{r}{a}\right)\right) \text{ in } \hat{e}_\theta \tag{4.5}$$

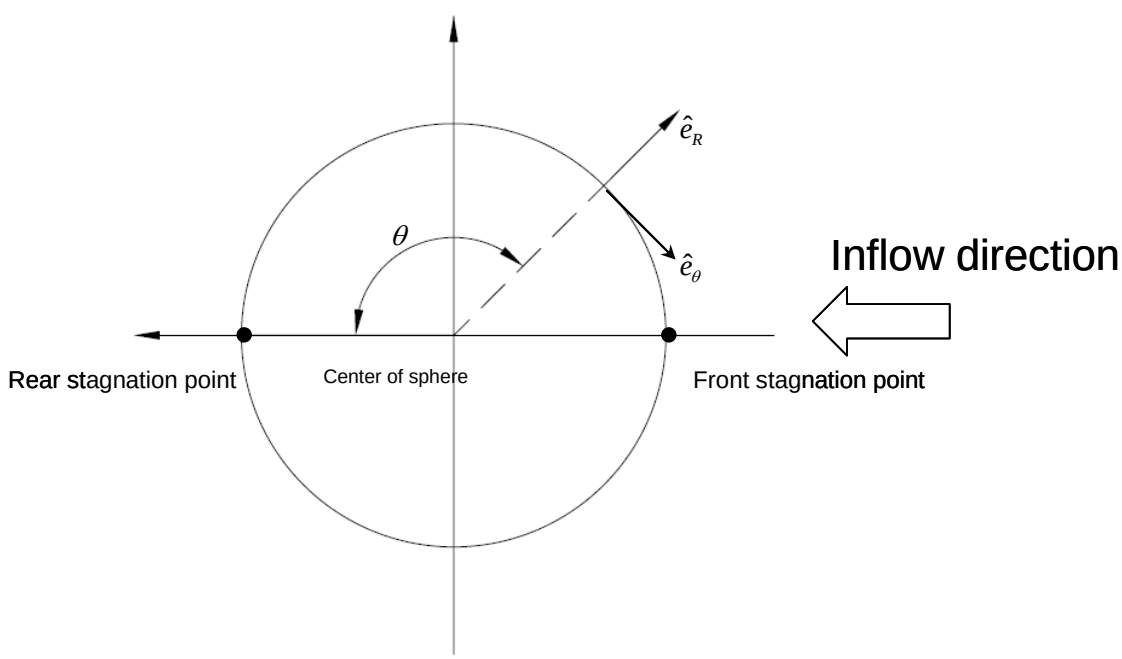

Figure 5- Spherical coordinates of analytical solution based at the center of the solid sphere.

After the proper coordinate transformation, the numerical results of the velocity distributions shown in Figure 4 agreed well with the analytical solution given in Equations 4.4 and 4.5.

For the flow at $Re \leq 0.5$, the exact solution for the drag force F_{drag}, which is the sum of form drag (due to pressure) and friction drag (due to viscous stress), is calculated as:

$$F_{drag} = 3\pi\mu D U_{\infty} \tag{4.6}$$

where μ is the fluid viscosity, D is the sphere diameter, and U_{∞} is the free-stream velocity. By substituting Equation 4.6 into Equation 4.7, a direct relationship between the drag coefficient C_D and the Reynolds number Re is derived:

$$C_D = \frac{\dfrac{F_{drag}}{\left(D^2/4\right)\pi}}{1/2\rho U_{\infty}^2} = \frac{24}{Re} \tag{4.7}$$

where F_{drag} is the drag force defined in Equation 4.6, D is the diameter of the sphere, ρ is the fluid density, U_{∞} is the free-stream velocity, and Re is the Reynolds number defined in Equation 4.3.

4.2.2 Axisymmetric Flow Past A Sphere for $24 \leq Re \leq 200$

For Reynolds number exceeds $Re>24$, the fluid starts to separate from the sphere surface, forming a recirculation zone in the wake-region. The fluid flow past a sphere was simulated at $Re=25$, $Re=50$, $Re=100$, $Re=150$, and $Re=200$ at the mesh resolution 25x125. The numerical domain scales with the sphere radius, R. The domain has a length of $z = 20R$ and a radius of $r = 4R$. For the above five Reynolds numbers, the streamlines past the sphere are plotted in Figure 6.

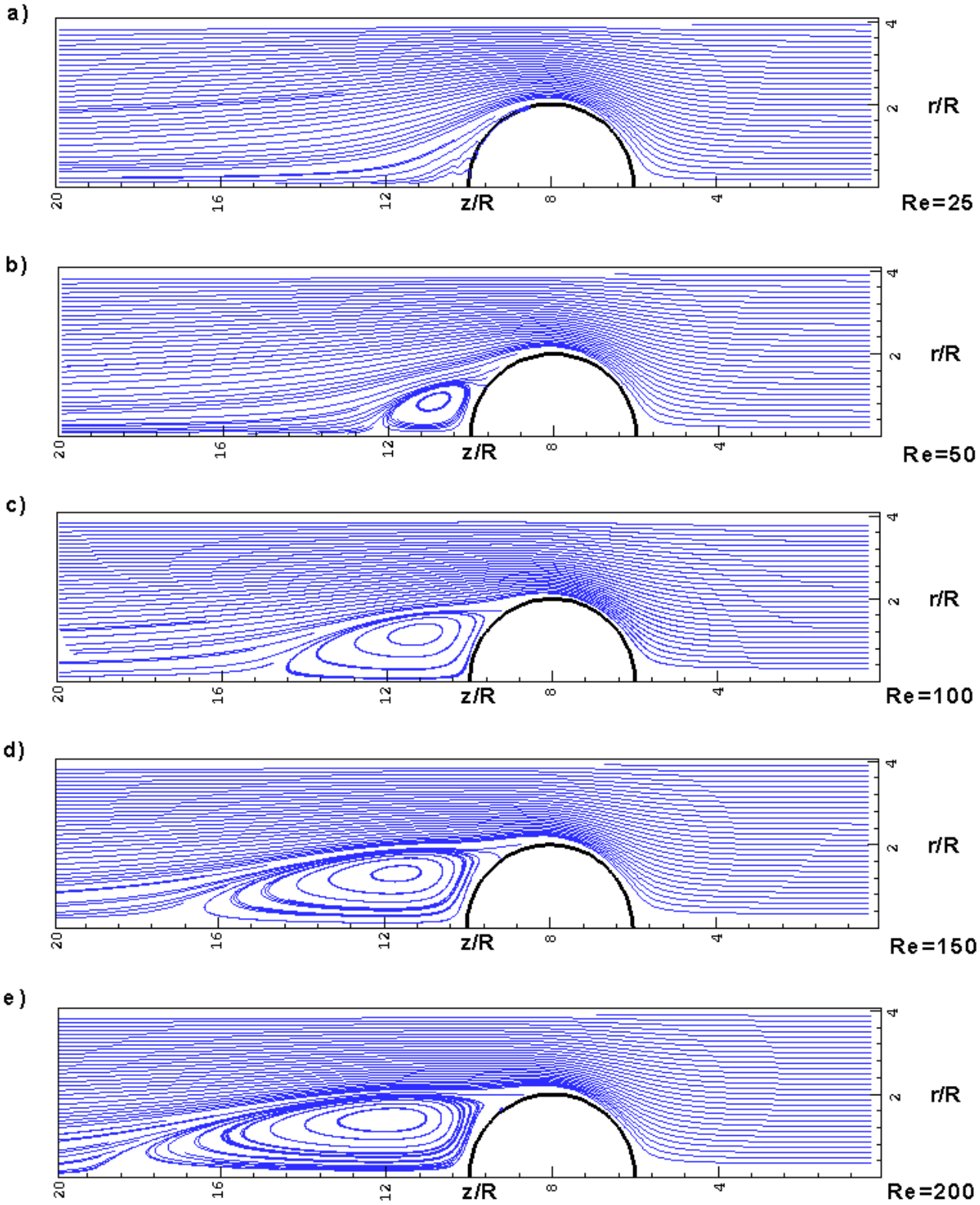

Figure 6- Axisymmetric streamlines past the sphere, a) *Re*=25; b) *Re*=50; c) *Re*=100; d) *Re*=150; e) *Re*=200.

In Figure 6, as $Re>24$, the fluid starts to separate from the solid surface and a recirculation zone is formed in the wake-region. The size of the recirculation zone increases with increasing the Reynolds number as shown in Figure 6.

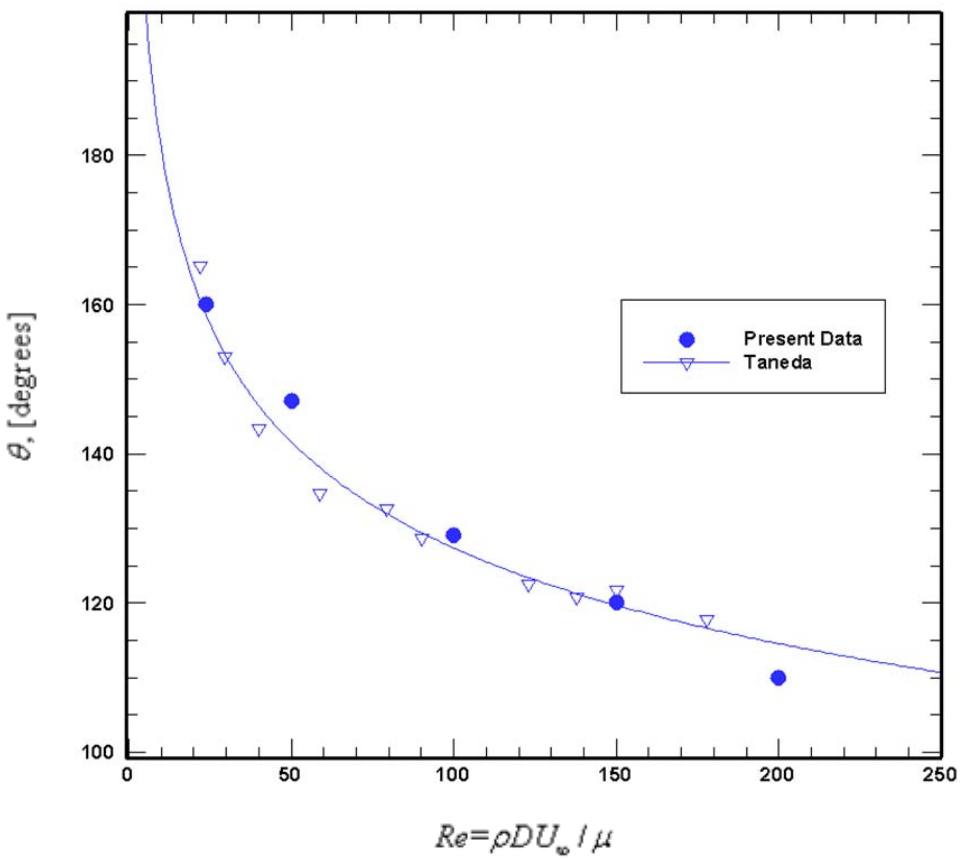

Figure 7- Separation angle vs the Reynolds number for axisymmetric flow past a sphere

To verify the streamline plots in Figure 6, the separation angle θ was measured and compared with Taneda's results [2], see Figure 7. The separation angle is defined between the axisymmetric line and the point at which fluid separates from the sphere surface. θ at the four Reynolds numbers, $Re=25$, $Re=25$, $Re=50$, $Re=100$, and $Re=150$, are in good agreement with Taneda's results, but the angle at $Re=200$ deviated slightly from the curve. It is speculated that the deviation is caused by the fact

that the flow starts to become asymmetric when $Re \geq 200$, but the model simulates the above streamline plots at the axisymmetric conditions.

Finally, to summarize the modeling results for the axisymmetric flow past a sphere, the drag coefficient C_D is plotted against the Reynolds number Re for the flow regime of $Re \leq 200$, see Figure 8. The numerical data generated from this model agrees well the experimental data of Clift and Gauvin [5], whose values are represented by Equation 4.8:

$$C_D = \frac{24}{Re}\left(1 + 0.15 Re^{0.687}\right) + \frac{0.42}{1 + 4.25 \times 10^4 Re^{-16}} \tag{4.8}$$

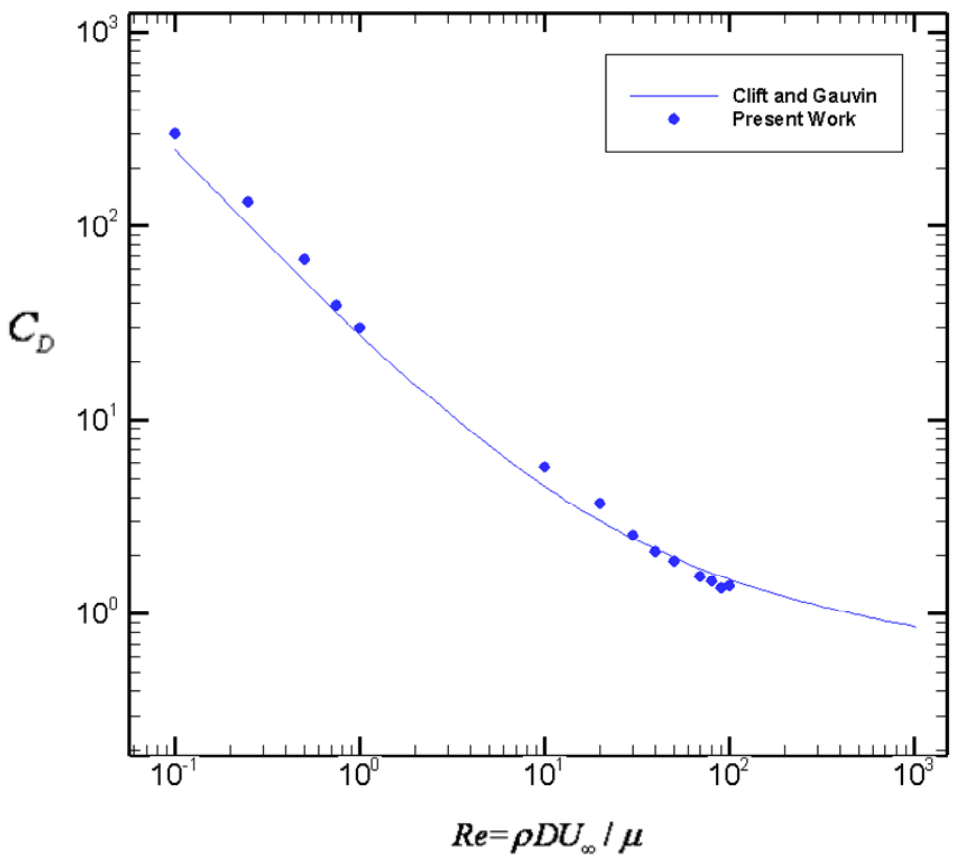

Figure 8- Drag Coefficient C_D vs the Reynolds number Re for $Re \leq 200$.

References

[1] TA Johnson and VC Patel. Flow past a sphere up to a Reynolds number of 300. *Journal of Fluid Mechanics*, 378: 19-70, 1999.

[2] S Taneda. Experimental investigation of the wake behind a sphere at low Reynolds numbers. *J. Phys. Soc. Japan*, 11: 1104-1108, 1956.

[3] S Lee. A numerical study of the unsteady wake behind a sphere in a uniform flow at moderate Reynolds numbers. *Computers & Fluids*, 29: 639-667, 2000.

[4] DR Poirier and GH Geiger. "Creep Flow around a Sphere", Transport Phenomena in Materials Processing. The TMS society, Warrendale, 68~71, 1994.

[5] R Clift, JR Grace, and ME Weber. Bubbles, Drops, and Particles. Academic Press, San Diego, CA, 1978.

CHAPTER 5

RESULTS AND DISCUSSION

In Section 1.2.2, the advantages and disadvantages of spraying materials in a gas at low temperature were described. The primary advantage is that less thermal degradation will occur, and so the initial composition of the coating material can be maintained throughout the deposition process. The disadvantage of spraying at a low gas temperature is that the melting degree of the sprayed particles is usually lower. This causes a higher volume fraction of unmelted particles, which leads to more voids (or porosity) in the as-deposited coatings. To optimize the coating properties, a balance between the thermal degradation and the porosity level must be struck.

The present 2D model of a single semi-molten drop impact can serve to begin to assess this balance. Porosity in the microstructure of a thermal spray coating is related to the flattening behavior of each individual particle upon impact on a solid substrate. The present model can be used to examine the relationships between the spreading degree and the solid core size, which can be correlated to the molten fraction of a homogenous sprayed particle, or to the solid phase volume fraction of a heterogeneous particle such as WC-Co. The effect of the solid core is modeled by simulating the fluid flow of a liquid

tin drop with a solid core immersed at its center. Tin was chosen since most so materials sprayed at low gas temperatures are metallic, yet tin is readily used in the lab. The gas phase is assumed to be invisid. It is assumed that the substrate temperature is higher than the melting temperature of tin and hence no solidification occurs on impact. The substrate is assumed to be made of stainless steel, and the associated contact angle of tin on the surface is $\theta = 125^{\circ}$. The fluid properties of tin are listed in Table 1. The material of the solid core is irrelevant to the spreading behavior of the liquid tin, as only the no-slip boundary condition is imposed at the solid-liquid interface regardless of the solid material used.

The initial configuration of a solid-liquid droplet is shown in Figure 1. The center of the liquid drop is located at a height of 0.9 times the drop radius (denoted as R), and the center of the solid core is located at a height equal to its radius (denoted as r). Both centers (of the drop and the solid core) are aligned at $x = 0$, which is the symmetry axis. It is assumed that the solid core is fixed at the solid substrate at the beginning of the simulation because the immersed boundary algorithm implemented in this model only considers a stationary solid object.

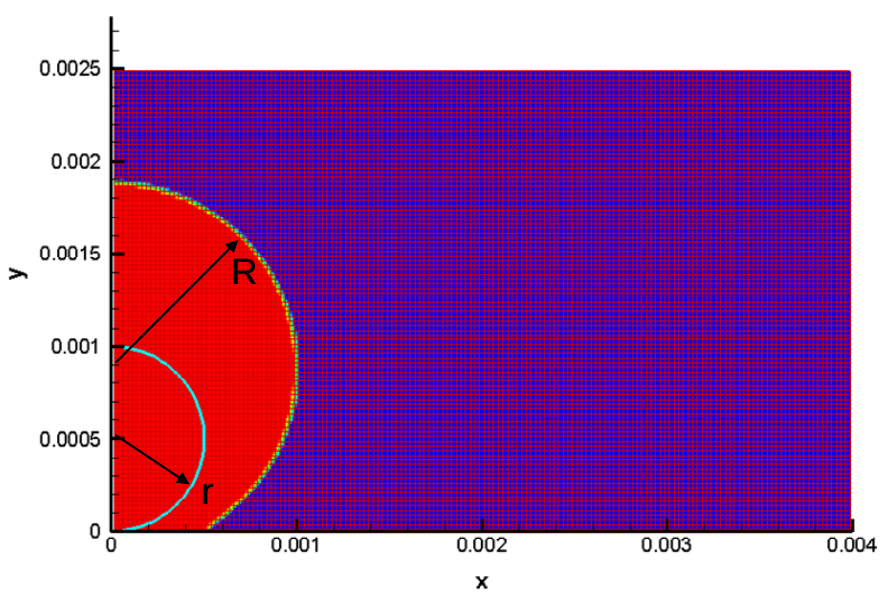

Figure 1-Initial configuration of a solid-liquid drop used in the model.

Density [kg/m^3]	7000
Viscosity [kg/m-s]	0.00185
Surface Tension [N/m]	0.544
Contact Angle [degree]	125

Table 1- Fluid properties of liquid tin on stainless steel.

The center of the drop is set lower than its radius to avoid a sharp liquid-gas-solid interface at the substrate surface. The numerical domain scales with the drop radius R: It has a height of $y = 2.5R$ and a radius of $x = 4R$. A uniform mesh is employed and the mesh resolution is set to $cpr = 25$, where cpr stands for the number of cells per drop radius.

To quantitatively measure the spread behavior, three terms are introduced as follows. The time t is non-dimensionalized as:

$$t^* = \frac{tU_o}{D_o} \tag{5.1}$$

where t^* is the non-dimensional time, U_o is the impact velocity, and D_o is the initial drop diameter. A spreading degree ξ is defined, and that gives a simple measure of how a deformed droplet flattens:

$$\xi = \frac{D_{splat}}{D_o} \tag{5.2}$$

where D_{splat} is the splat diameter. Finally, the maximum spread degree $\xi_{\max}$ is defined at the maximum spread:

$$\xi_{\max} = \frac{D_{splat,\max}}{D_o} \tag{5.3}$$

where $D_{splat,\max}$ is the maximum splat diameter that occurs during the droplet spread.

5.1 Impact of a Molten Tin Drop

In order to analyze the effect of solid core size, a "reference" tin drop without a solid core was first simulated. For a completely molten tin drop with $R = 1\ mm$, impacting at $U_o = 1\ m/s$, three distinct stages of droplet deformation can be observed from the spread curve in Figure 3 (snapshots of the droplet deformation at different t^* are illustrated in Figure 4):

1) $0 \le t^* \le 0.5$: During the initial stage, the droplet flattens as the kinetic energy is dissipated into surface tension and viscous work.
2) $0.5 \le t^* \le 1.5$: A ring-shaped rim forms at the circumference of the droplet. In this stage, the inner area of the droplet is drawn to a thin film.
3) $1.5 \le t^* \le 3.5$: The rim of the droplet recoils under the surface tension force. The deformed droplet may recoil to a high extent and rebound off the substrate surface completely.

5.2 Impact of a Semi-Molten Tin Drop

In this section, semi-molten tin drops with constant drop radius $R = 1\ mm$ and different solid core size ratios were analyzed. For the impact velocity of $U_o = 1 m/s$, the Reynolds number and the Weber number are 7568 and 26, respectively. Re and We were defined in Section 1.2.1.

r/R	*Φ*	*V_liquid* [mm^3]	D_{liquid} [mm]	ξ*max
0	1.000	4.189	2.000	
0.2	0.992	4.155	1.995	2.121
0.3	0.973	4.076	1.982	2.128
0.35	0.957	4.009	1.971	2.092
0.45	0.909	3.807	1.937	2.065
0.55	0.834	3.492	1.882	1.966
0.6	0.784	3.284	1.844	1.898
0.65	0.725	3.038	1.797	1.836
0.7	0.657	2.752	1.739	1.757

Table 2- For constant drop R=1mm, the corresponding volume fraction ϕ of the liquid phase, the volume of liquid phase V_liquid and the equivalent fluid diameter D_{liquid}, for various core size ratios r/R.

Figure 5 shows the spread curves at the various core size ratios ranging from $r/R = 0$ to $r/R = 0.7$. The curves for larger core size ratios reach lower values of $\xi_{\max}$ within a shorter period of time, in part because as the solid core size increases at constant R, less fluid is available for spreading. The volume fraction of the liquid phase ϕ in a semi-molten drop is calculated as:

$$\phi = 1 - \left(\frac{r}{R}\right)^3 \tag{5.4}$$

The volume fractions of the liquid phase are shown in Table 2, for core size ratios ranging from 0.2 to 0.7.

In Figure 5, the spread degree was analyzed based on the ratio of splat diameter to initial drop diameter, see Equation 5.2. But as the solid core does not contribute to spreading of a semi-molten drop, perhaps its volume should not be considered as part of the initial fluid volume. To examine the spread behavior of a semi-molten drop in terms of the volume of liquid phase available, a modified spread degree $\xi*$ is defined in Equation 5.5.

$\xi*$ is calculated based on the diameter of a pure liquid drop D_{liquid} whose volume is equivalent to the liquid phase inside the semi-molten liquid drop.

$$\xi* = \frac{D_{splat}}{D_{liquid}} \tag{5.5}$$

where,

$$D_{liquid} = D_o \phi^{1/3}$$

Figure 6 presents $\xi*$ vs time, and takes into account the changing fluid volume as the solid core size varies. That is, the curves with larger solid core size ratios correspond to smaller values of D_{liquid}, see Table 2. After the modifications, the curves in Figure 6 are closer together than the curves in Figure 5. Specifically in Figure 6, the curves within the time period of $0 \le t* \le 0.5$ are very similar and almost collapse on the same line. This indicates that during the initial spread, the spread degree is less affected by different solid core sizes. On the other hand, during the time period $0.5 \le t* \le 1.5$, the curves diverge, and those for smaller core size ratios reach higher values of $\xi^*_{\max}$ than those for larger core size ratios. In summary, the fluidity of a semi-molten drop increases as the core size ratio decreases, and so the solid core is less of an impediment to the fluid motion. The effects of solid core size and fluid volume are analyzed in detail in Sections 5.5 and 5.6.

5.3 Comparison of Molten and Semi-Molten Drop Impacts

To compare the spread behavior of a molten and a semi-molten tin drop, snapshots of semi-molten tin drops with core size ratios of $r/R = 0.2$, $r/R = 0.55$, and $r/R = 0.7$, are shown in Figure 7, 8, and 9, respectively. The splat morphology of the semi-molten drop is very similar to the molten tin drop during the initial stage of spreading from $0 \le t^* \le 0.5$ (compare Figure 4 with Figures, 8, and 9). But as $t^* \ge 0.5$, the splat morphology changes. At $t^* = 1.0$, most fluid that was originally on top of the solid core had spread out to the side completely, leaving the top surface of the solid core to sticking out of the splat surface. In addition, due to the presence of the solid core in the center, the fluid in the semi-molten drop is forced to spread around the solid core at an angle, such that a "triangulated" area is formed. As a result, the center region of a completely molten drop is drawn out to a much thinner splat thickness, see Figure 4.

Figure 10 to 13 illustrate these impacts in more detail, and show the velocity fields as well. Figure 11 shows the fluid flow inside a drop of $R = 1\ mm$ with a core size ratio $r/R = 0.2$. In this case, the fluid in the drop spreads in a very similar fashion as the drop without a core, see Figure 10. This is because the volume fraction of fluid in this case is 99.2%, and hence it is reasonable that the fluid flow varies little in the presence of a small solid core. After the splat spreads to the maximum diameter around $t^* = 1.5$ in Figure 11, it starts to recoil, as indicated by the formation of a recirculation flow in the periphery of the splat. As the splat recoils, a ring-shaped rim is formed and the recirculation flow inside the rim flows in the opposite direction to the spreading fluid.

Figure 12 shows the fluid flow of the same drop size but with a larger core size ratio $r/R = 0.55$ (the volume fraction of fluid associated with this core size is 83.4%). In this case, fluid immediately feels the presence of the solid core as the drop spreads. As fluid flows past the solid core, it separates from the core surface and spreads along a plane which we later refer to as the "separation plane", see Figure 2. The fluid beneath the separation plane forms a recirculation flow at $t^* = 0.5$, which is not seen in the

completely molten drop. It is expected that this recirculation flow will increase the dissipation of viscous energy of the fluid that is spreading along the separation plane since it flows in the opposite direction to the fluid above it. In addition, the fluid inside the recirculation flow formed by the solid core is trapped, which means that less fluid is available for spreading.

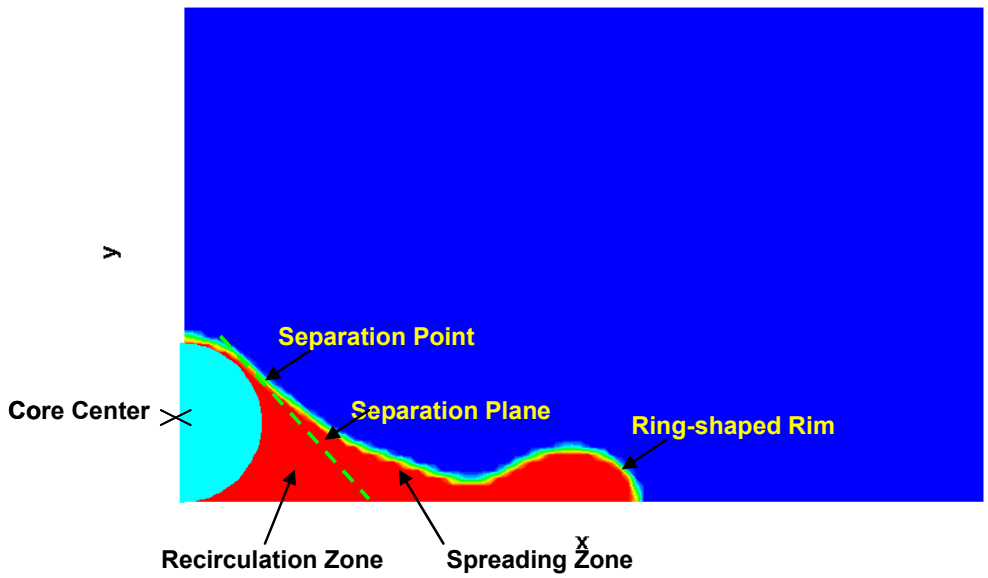

Figure 2- Illustration of different flow zones inside a solid-liquid droplet during spreading.

As the rate of kinetic energy is dissipated faster for the drop with $r/R = 0.55$ than for the drop with $r/R = 0.2$, the splat recoils at an earlier time. For $r/R = 0.55$, the splat recoils at $t^* = 1.0$ as indicated by the concave-shaped splat surface. For $r/R = 0.2$, the splat recoils at $t^* = 1.5$. In fact as the core size ratio increases to $r/R = 0.7$, the kinetic energy of fluid is dissipated so fast that the surface recoils immediately after the fluid spreads to the substrate surface. The splat diameter is so small that the two recirculation flows – one beneath the solid core and the other inside the rim- almost collapse near the separation plane, see $t^* = 1.0$ in Figure 13.

5.4 Effect of Impact Velocity

In this section, the effect of impact velocity on a semi-molten tin drop impact is explored for two different core size ratios: $r/R = 0.7$ or $r/R = 0.2$, for a drop of radius $R = 1\ mm$.

U_o **[m/s]**	***Re***	***We***
1	7568	26
2	15135	103
3	22703	232
4	30270	412

Table 3- Reynolds and Weber numbers for different impact velocities U_o

For both core sizes, the impact velocity was varied from $U_o = 1\ m/s$ to $U_o = 4\ m/s$; the corresponding Reynolds and Weber numbers are shown in Table 3.

Figure 14 shows snapshots of a semi-molten tin drop with a core size ratio of $r/R = 0.7$ spreading at $t^* = 1$, at four different impact velocities. The plots show that the spread degree increases with increasing impact velocity. This is due to the increase in kinetic energy to overcome surface tension and viscous work, as reflected by the higher values of Re and We. The increase in the splat degree means that the splat thickness becomes thinner, because the same volume of fluid contributes to spreading. As well, volume of fluid that is trapped inside the recirculation flow near the solid core remains relatively the same in the four plots, because as the fluid flows down from the top of the drop, it separates from the solid surface and spreads along the separation plane. Increasing the impact velocity does not release the trapped fluid from this recirculation zone.

Figure 15 shows snapshots of a semi-molten tin drop spreading with core size ratio of $r/R = 0.2$ at $t^* = 1$, at four different impact velocities. Increasing the impact velocity

imparts more kinetic energy to the drop. As a result, the rim that is formed due to surface tension at $U_o = 1\ m/s$ flattens out when the impact velocity exceeds $2\ m/s$. Nevertheless, the center of the splat morphology does not change much as the recirculation zone formed by the solid core is still present in the center at the high impact velocities.

5.5 Effect of Solid Core Size

In this section, the effect of solid core size as it impedes fluid motion is analyzed. To eliminate the effect of fluid volume on the fluidity of the spread, a constant fluid V_{consr} was added to a varying solid core size, so that the total drop radius R varied as follows:

$$R = \left(\frac{3}{4\pi} V_{consr} + r^3 \right)^{1/3} \tag{5.6}$$

where V_{consr} is the constant fluid volume. In this section, V_{consr} is set to $3.6652\ mm^3$, which is chosen based on based on $r = 0.5\ mm$ and $R = 1\ mm$. The drop radii for different solid core radii, ranging from $r = 0.2\ mm$ to $r = 0.9\ mm$, are shown in Table 4.

Figure 16 shows the modified spread degrees ξ^* based on Equation 5.5. In Figure 16, the maximum spread values decrease with increasing solid core size, which implies that larger solid cores impede the fluid motion to a greater extent than smaller ones. In addition, as the solid core size increases, the time required to reach the maximum spread decreases. This indicates that the rate of kinetic energy dissipation of fluid in a semi-molten drop with a larger core is faster than with a smaller core.

Figures 17 to 19 show snapshots of semi-molten drops containing different solid core radii: $r = 0.2\ mm$, $r = 0.6\ mm$, and $r = 0.9\ mm$. Notice that recoil occurs at different times, which indicates that the rates of kinetic energy dissipation to viscous work and surface energy are different even though they contain the same amount of fluid.

r [mm]	*R* [mm]	*r/R*	*Φ*	ξ*max
0.2	0.959	0.208	0.991	2.090
0.3	0.966	0.310	0.970	2.069
0.5	1.000	0.500	0.875	2.007
0.6	1.029	0.583	0.802	1.935
0.7	1.068	0.655	0.718	1.866
0.9	1.171	0.769	0.546	1.738

Table 4- For the conserved liquid volume $V_{consr} = 3.6652\ mm^3$ **, the solid core size is varied from** $r = 0.2\ mm$ **to** $r = 0.9\ mm$**.**

For $r = 0.2\ mm$, the rim of the splat recoils at $t^* = 1.25$, as indicated by the concave splat surface. For $r = 0.6\ mm$, the splat recoils at $t^* = 1.0$. For $r = 0.9\ mm$, the splat recoils at $t^* = 0.75$. In addition, the splat morphologies are very different. The splat shape is more controlled by the solid core as the solid core size increases, and it changes from a disk-shape to a sphere-shape.

5.6 Effect of Drop Size

In this section, the effect of fluid volume on the spreading of a semi-molten drop is analyzed. To eliminate the effect of solid core size on the spread, a constant solid radius of $r = 0.5\ mm$ is used while the drop radius increases from $R = 1\ mm$ to $R = 2\ mm$. The associated fluid volumes for different drop radii are shown Table 5.

Figure 20 shows the spread curves for various drop sizes ranging from $R = 1\ mm$ to $R = 2\ mm$. The maximum spread degree increases from $\xi^*_{\max} = 2.007$ to $\xi^*_{\max} = 2.664$ as the drop size doubles. This is expected since more fluid volume becomes available.

In comparison with the effect of solid core size on the spread (the maximum spread degree only increases from $\xi^*_{\max} = 2.007$ to $\xi^*_{\max} = 2.090$ when the solid core ratio varies from *0.5* to *0.2*, see Table 4), varying the drop size has a more profound effect on the semi-molten drop spread.

R [mm]	*r/R*	*Φ*	*V_liquid* [mm^3]	ξ*max
1.00	0.500	0.875	3.665	2.007
1.20	0.417	0.928	6.715	2.221
1.40	0.357	0.954	10.970	2.371
1.60	0.313	0.969	16.634	2.482
1.80	0.278	0.979	23.905	2.577
2.00	0.250	0.984	32.987	2.664

Table 5- For a constant solid core size $r = 0.5mm$, the drop size is varied from $R = 1.0\ mm$ to $R = 2.0\ mm$.

Finally, to analyze the combined effects of solid core size and drop size, two semi-molten drops- one with a drop radius of $R = 1\ mm$ and the other $R = 2\ mm$- are compared at the same core size ratios. The large semi-molten drop contains a bigger solid core than the small one but contains more fluid as well. The solid and fluid volumes of the two drops are compared in Table 6. The question that arises from Table 6 is which one of two factors- solid core size or drop size- is more dominant in controlling the spread of a semi-molten drop (it has been shown that a large solid core impedes fluid motion to a greater extent than a small solid one; on the other hand, increasing the fluid volume also increases the fluidity of a semi-molten drop). Figure 21 plots the maximum spread $\xi^*_{\max}$ vs the core size ratio r/R for these two drops. Both curves reach plateau values as the core size ratio decreases, since the solid core size becomes too small to impose any significant effects on the fluid. On the other hand, when the core size is comparable to the drop size, i.e. $r/R \geq 0.5$, significant changes in $\xi^*_{\max}$ are observed as indicated by the steep slopes. Finally, comparing $\xi^*_{\max}$ at the same core size ratio indicates that the larger drop spreads to a greater splat diameter, which implies that at the same core size ratio, even though the large drop contains a larger solid core, the fluidity of the drop is compensated by the higher fluid volume within it, as the drop size is more dominant than the solid core size in controlling the spread degree of a semi-molten drop.

	***R=1* mm**	***R=2* mm**
R [mm]	*1*	*2*
r [mm]	0.7	1.4
r/R	0.7	0.7
Φ	0.657	0.657
V_liquid [mm^3]	2.752	22.016
V_solid [mm^3]	1.437	11.494

Table 6- Comparison of two drops at the same core size ratio.

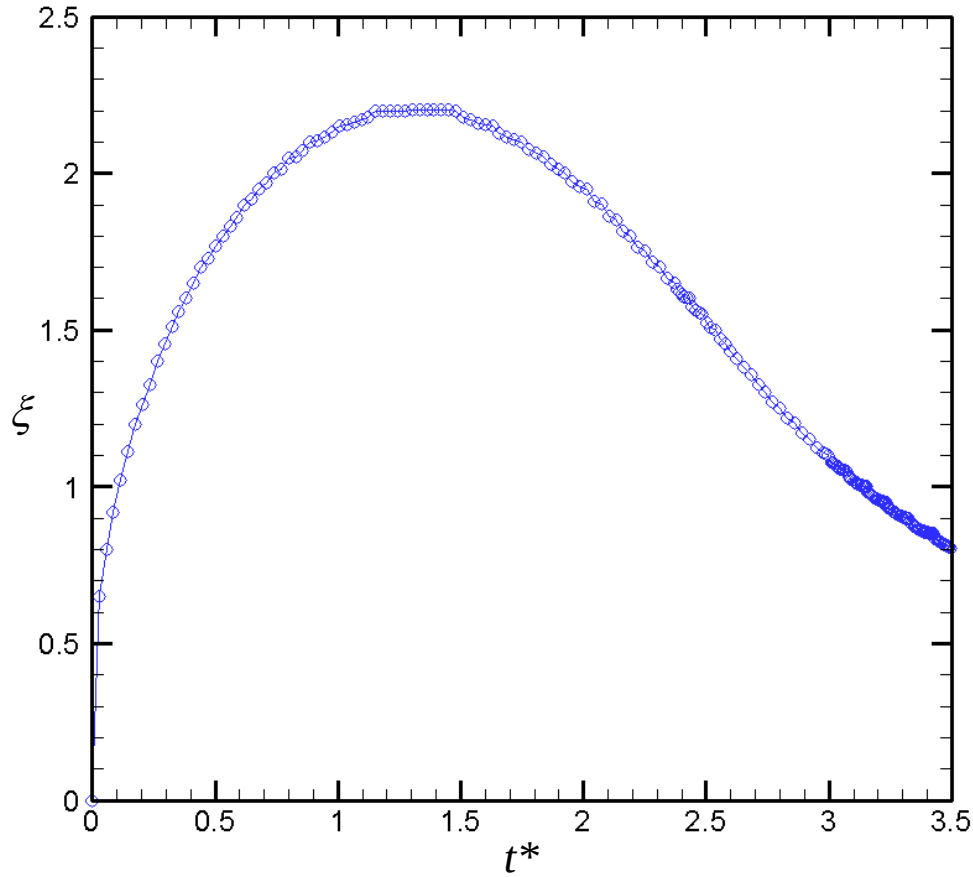

Figure 3- Spread degree ξ vs. non-dimensional time t* for the impact of a completely molten tin drop with radius R = 1 mm and impact velocity U_o = 1 m/s.

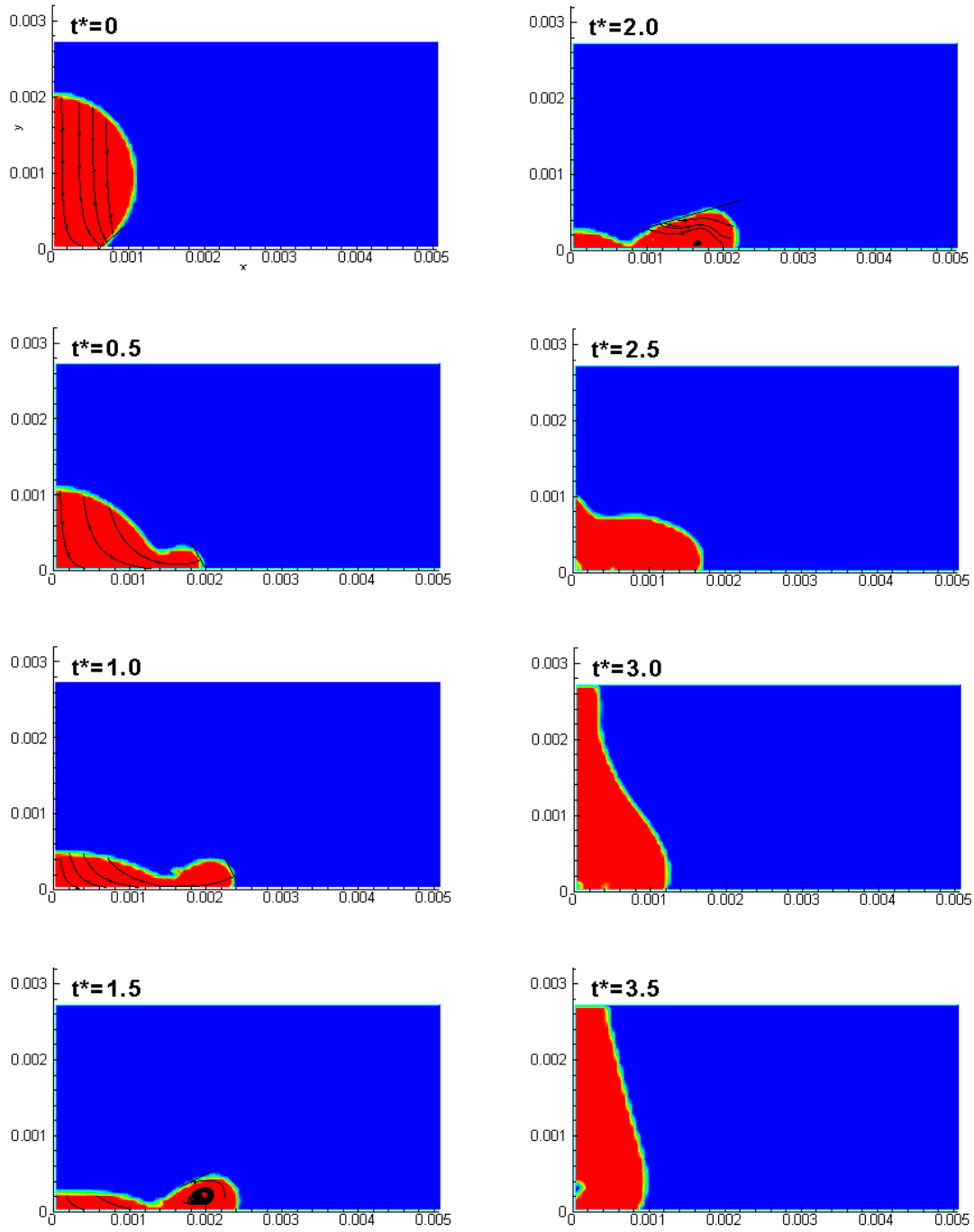

Figure 4- Snapshots of the impact of a complete molten tin drop with radius R= 1mm and impact velocity U_o = 1m/s. t* is the non-dimensional time, and t* = 3.5 corresponds to physical time t =7 ms.

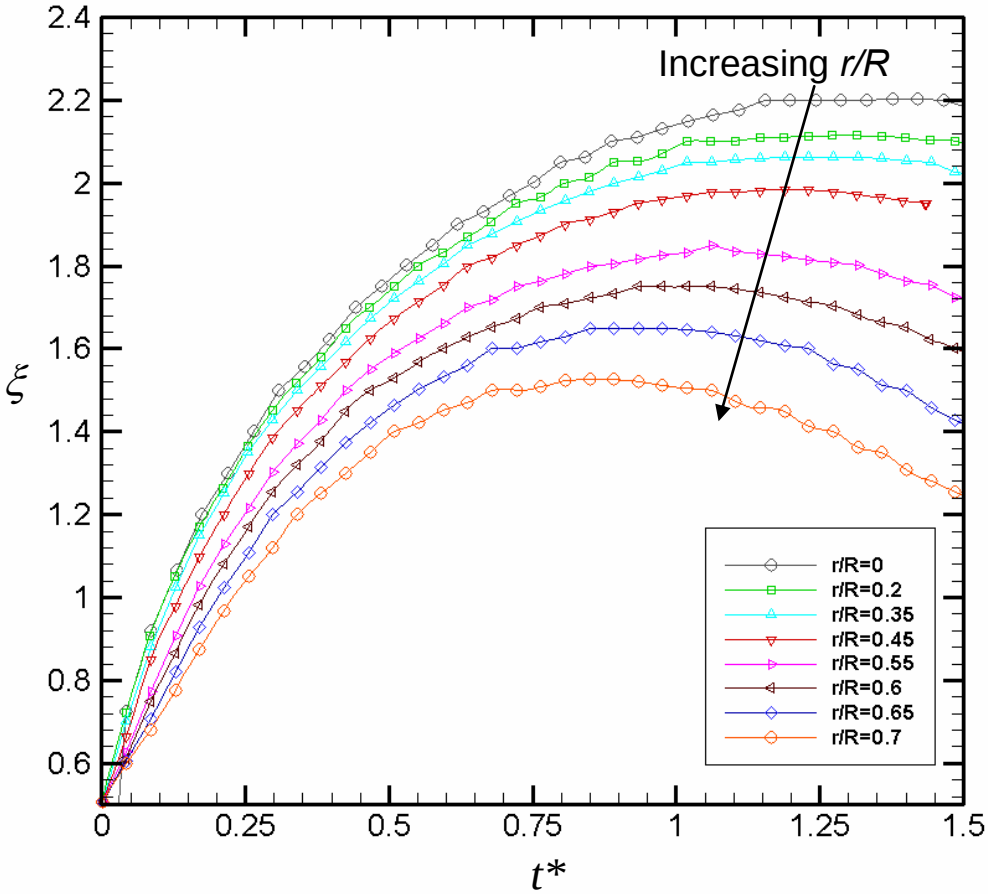

Figure 5- Spreading degree (ξ) vs non-dimensional time (t^*) for the impact of a semi-molten tin drop with constant drop radius ($R = 1\ mm$) and varying the core size radius (r).

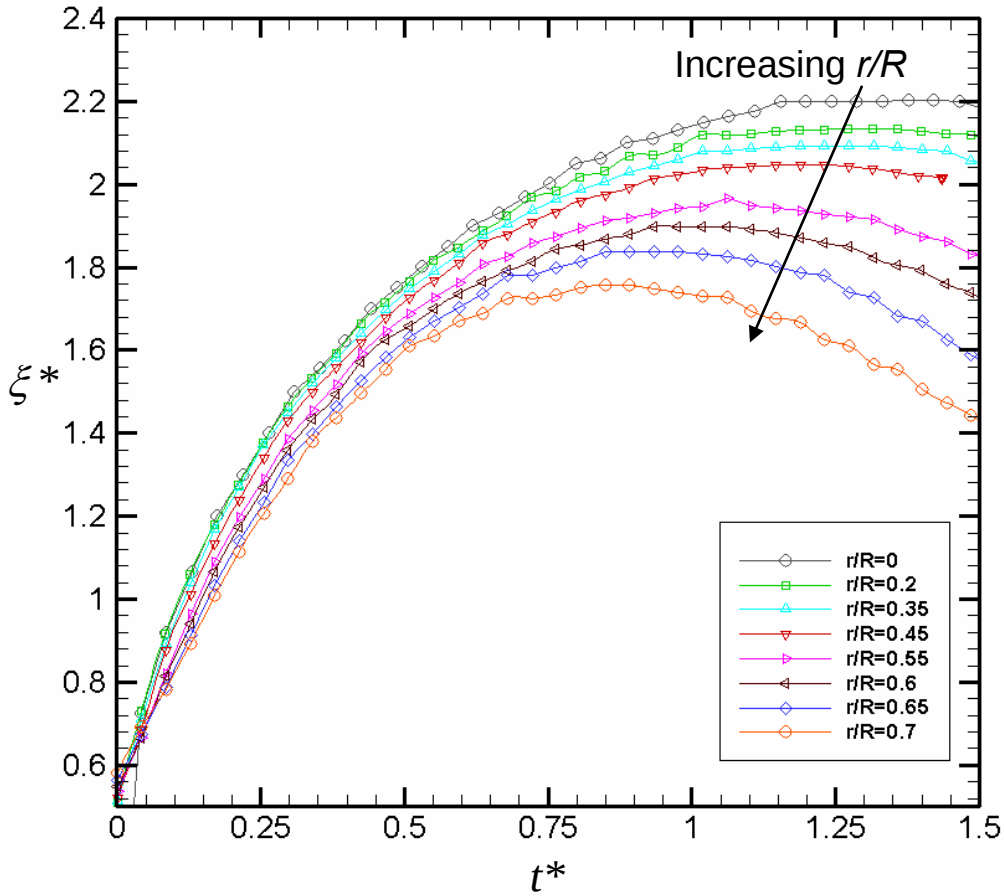

Figure 6- Modified spreading degree (ξ^*) vs non-dimensional time (t^*) for the impact of a semi-molten tin drop with constant drop radius ($R = 1\ mm$), and varying the solid core radius (r). ξ^* is based on the equivalent diameter D_{liquid} for the fluid volume inside the drop.

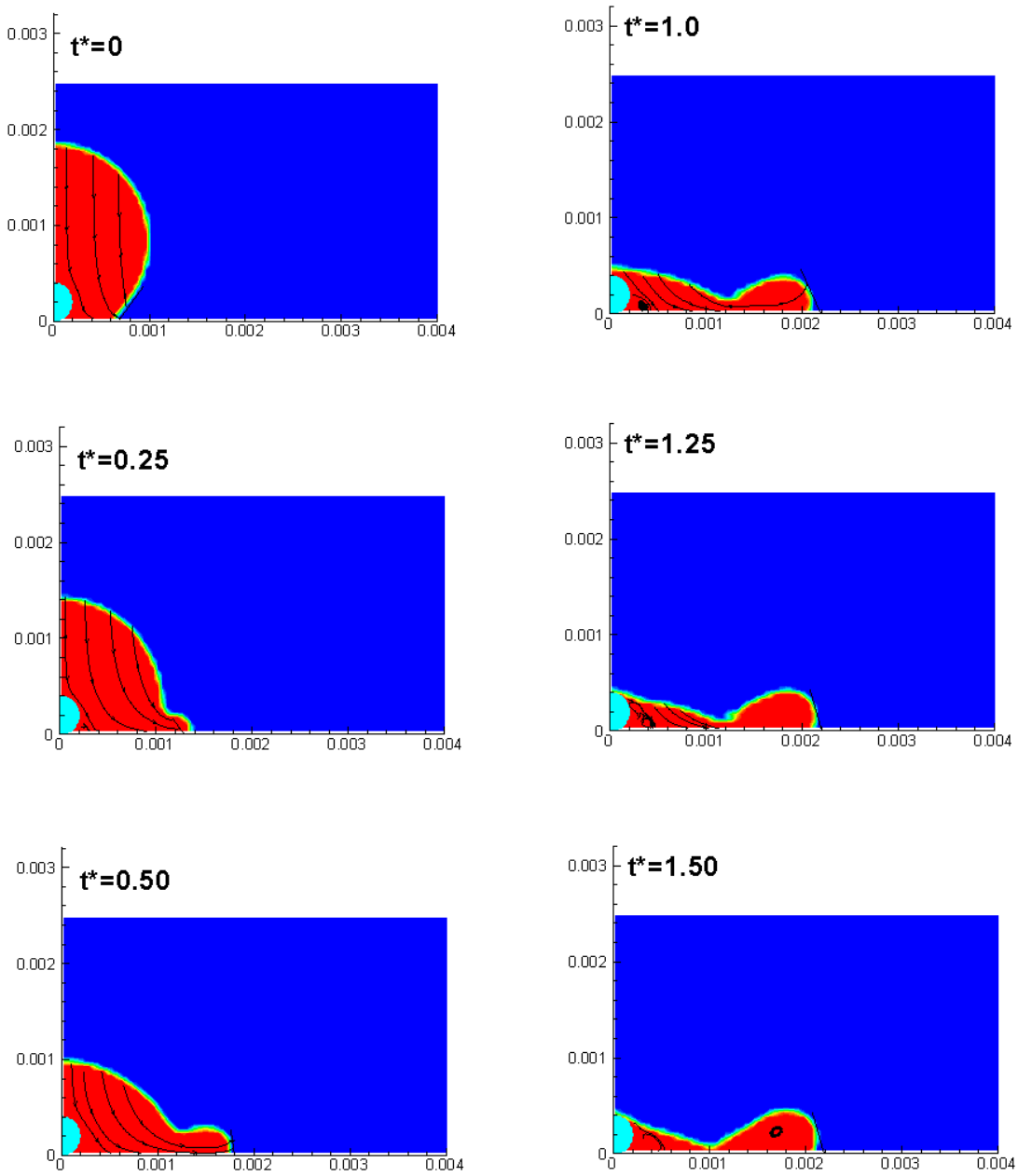

Figure 7- Snapshots of the impact of a semi-molten tin drop with drop radius ($R = 1\ mm$) and core size ratio ($r / R = 0.2$). The impact velocity is $U_o = 1\ m/s$ and t^* is the non-dimensional time. The value of $t^* = 1.5$ corresponds to real time $t = 3ms$.

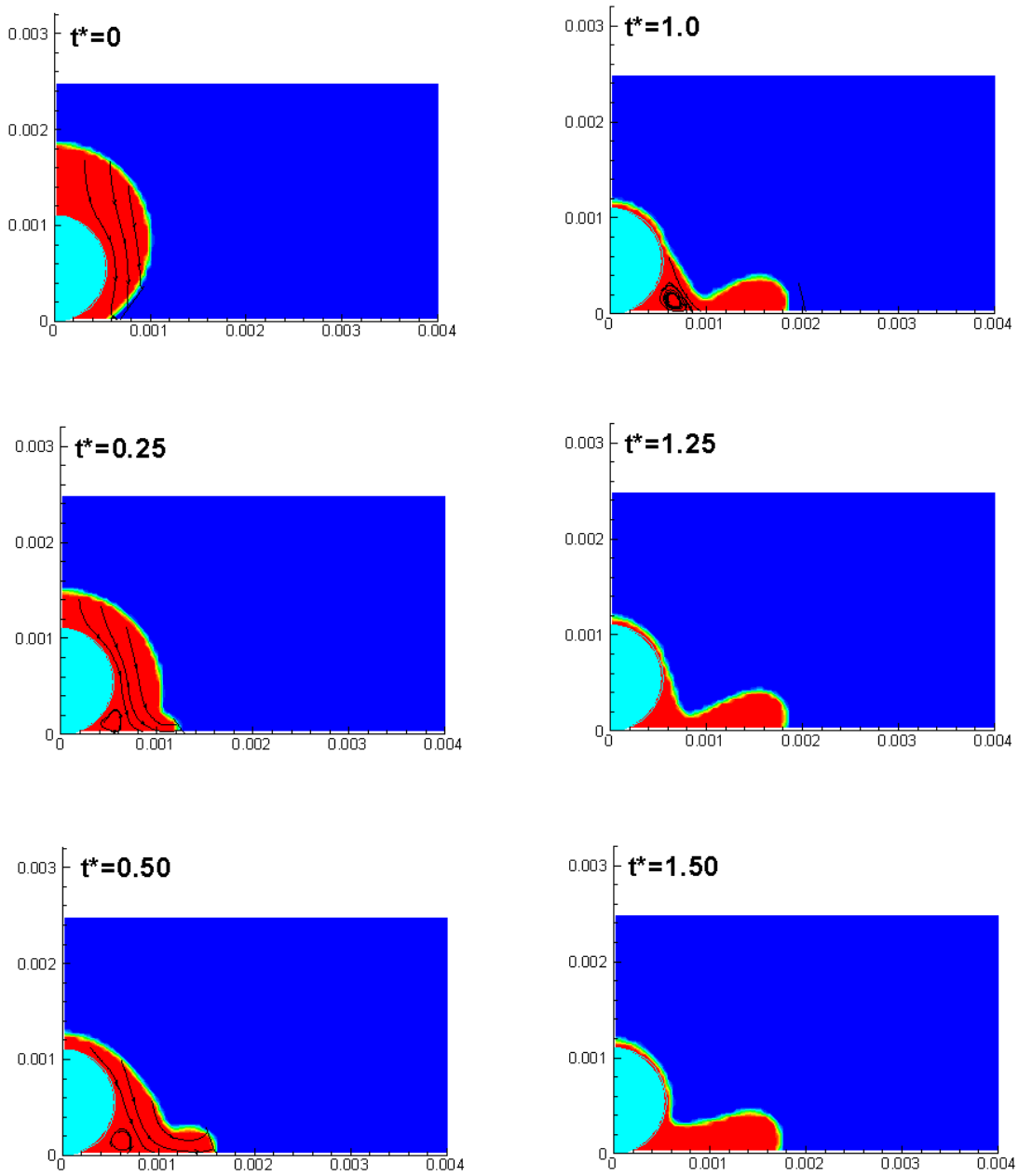

Figure 8- Snapshots of the impact of a semi-molten tin drop with drop radius ($R = 1\ mm$) and core size ratio ($r/R = 0.55$). The impact velocity is $U_o = 1\ m/s$ and t* is the non-dimensional time. The value of t* = 1.5 corresponds to real time t = 3ms.

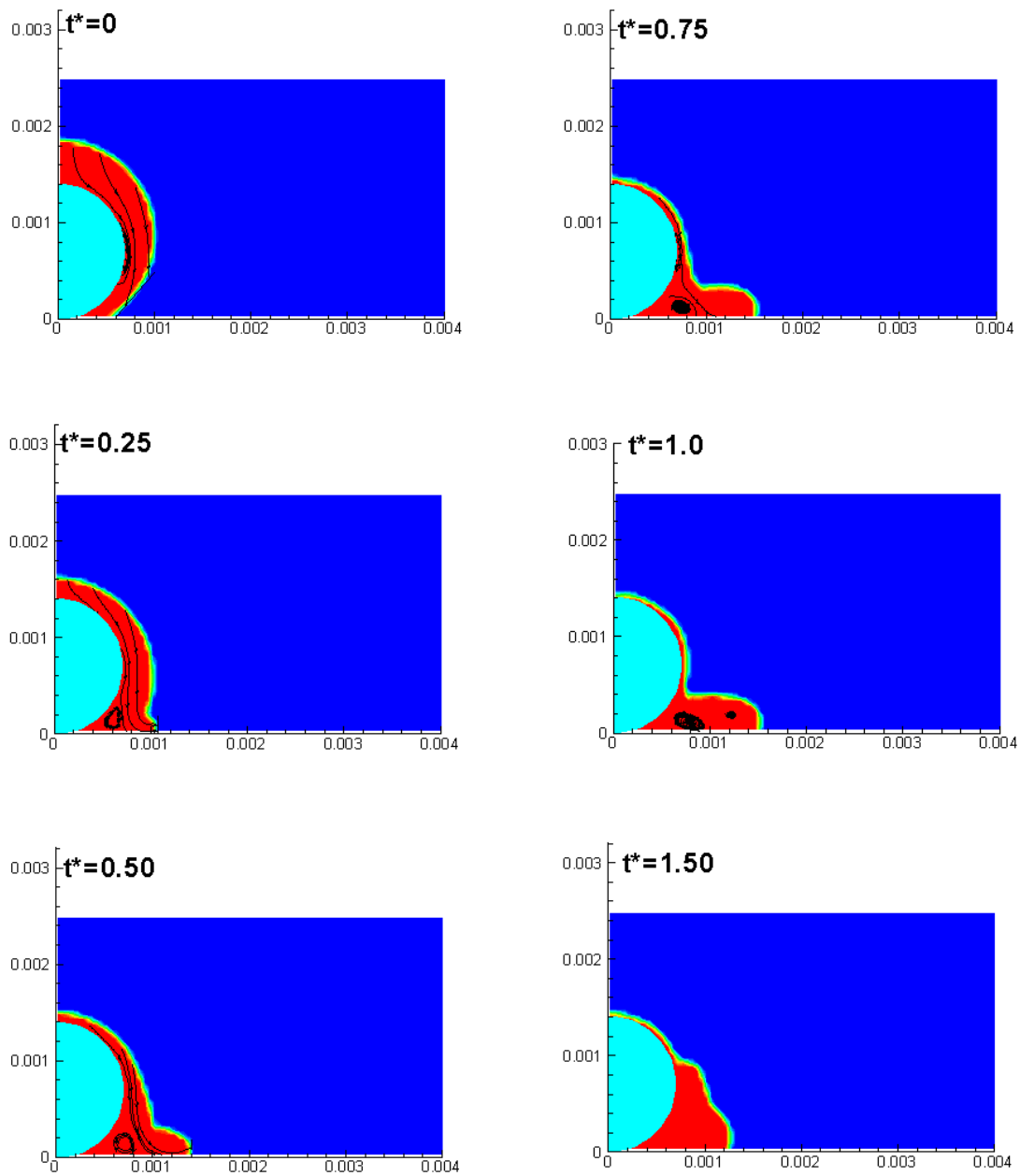

Figure 9- Snapshots of the impact of a semi-molten tin drop with drop radius ($R = 1\ mm$) and core size ratio ($r / R = 0.7$). The impact velocity is $U_o = 1\ m/s$ and t* is the non-dimensional time.

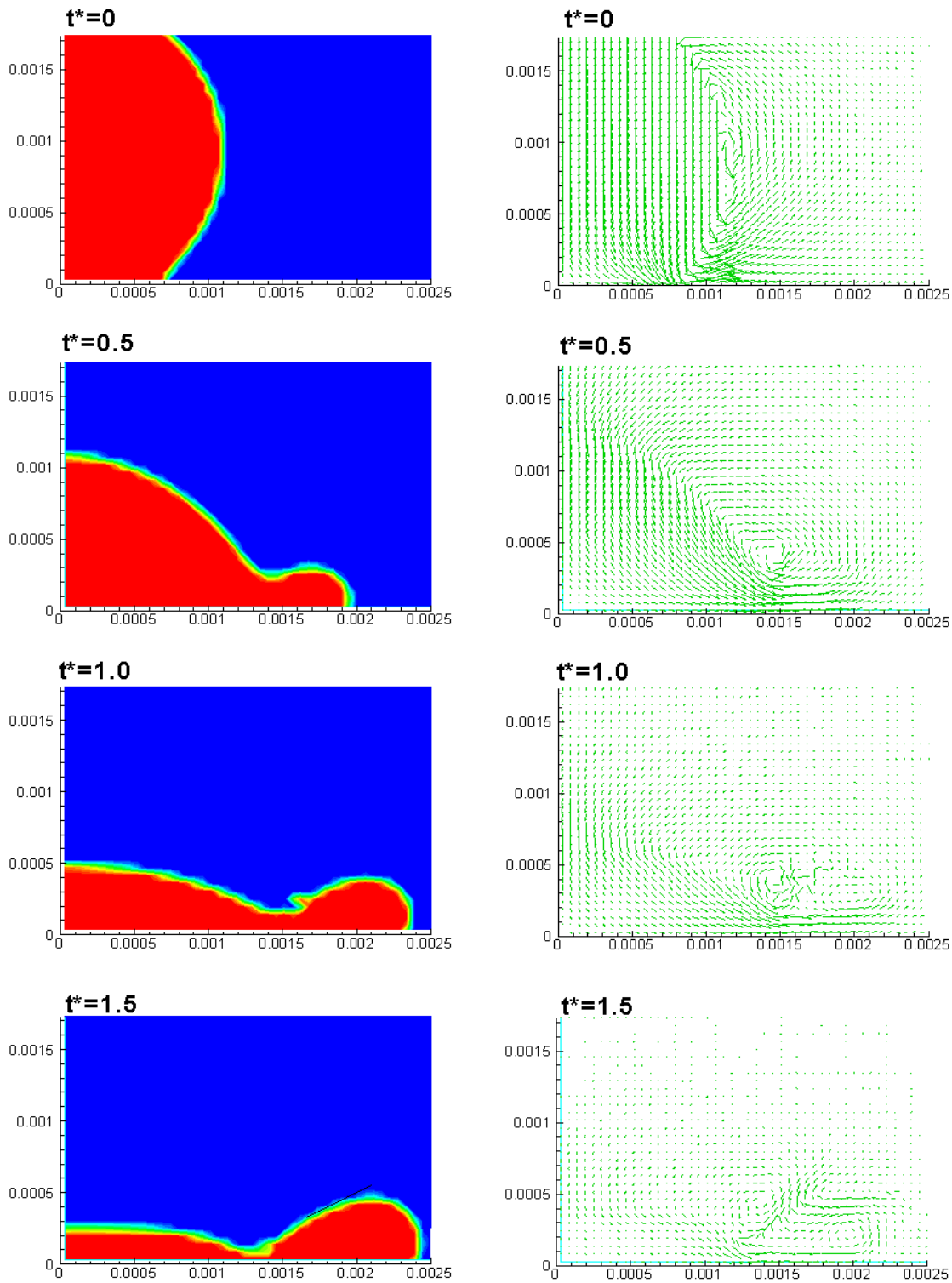

Figure 10- Snapshots of the impact of a completely molten tin drop with drop radius ($R = 1\ mm$). The impact velocity is $U_o = 1\ m/s$ and t* is the non-dimensional time.

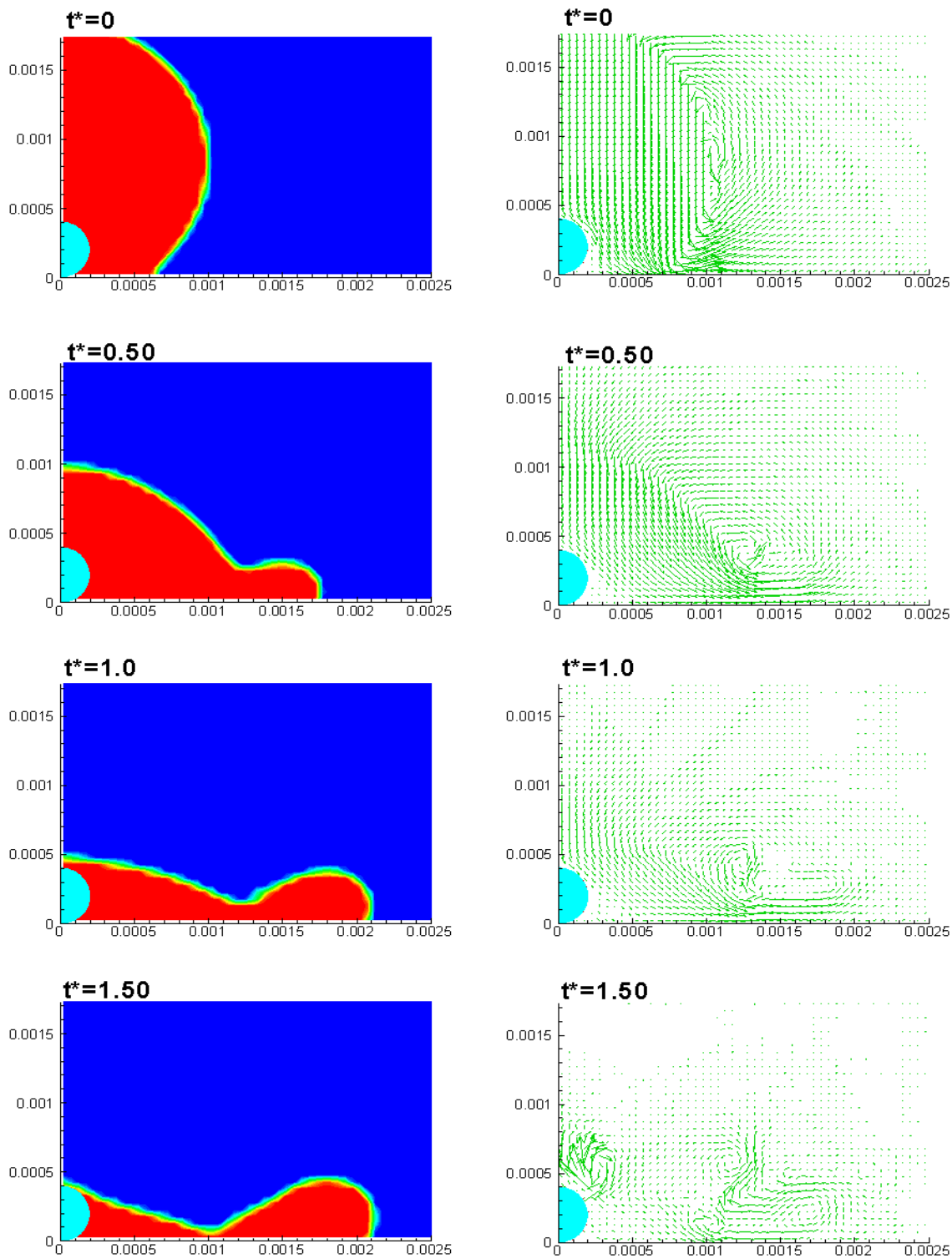

Figure 11- Snapshots of a semi-molten drop impact with drop radius ($R = 1\ mm$) and core size ratio ($r / R = 0.2$). The impact velocity is $U_o = 1\ m/s$. t* is the non-dimensional time.

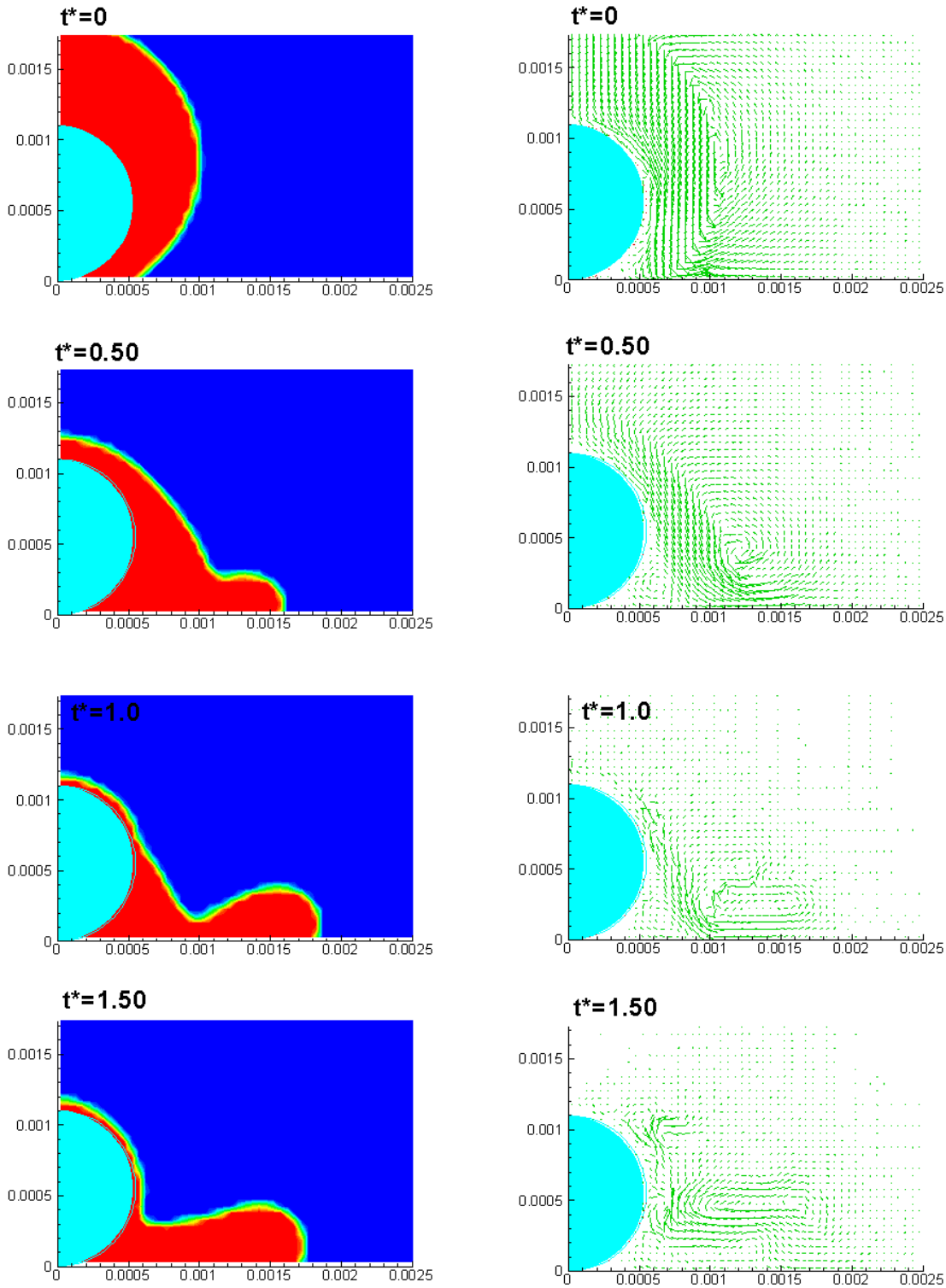

Figure 12- Snapshots of a semi-molten tin drop impact with drop size ($R = 1\ mm$) and core size ratio ($r / R = 0.55$). The impact velocity is $U_o = 1\ m/s$ and t^* is the non-dimensional time.

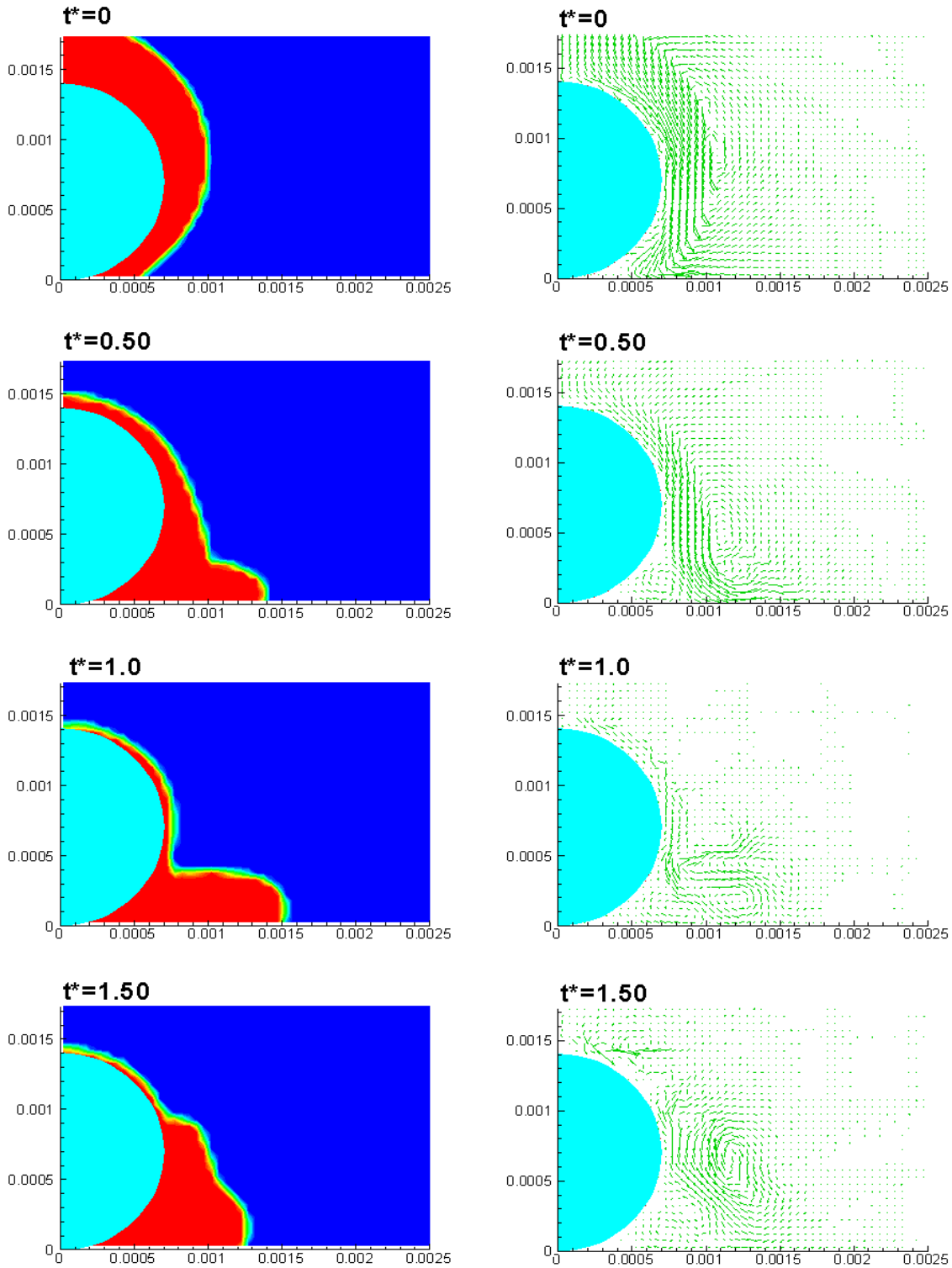

Figure 13- Snapshots of a semi-molten tin drop impact with drop size ($R = 1\ mm$) and core size ratio ($r / R = 0.7$). The impact velocity is $U_o = 1\ m/s$ and t^* is the non-dimensional time.

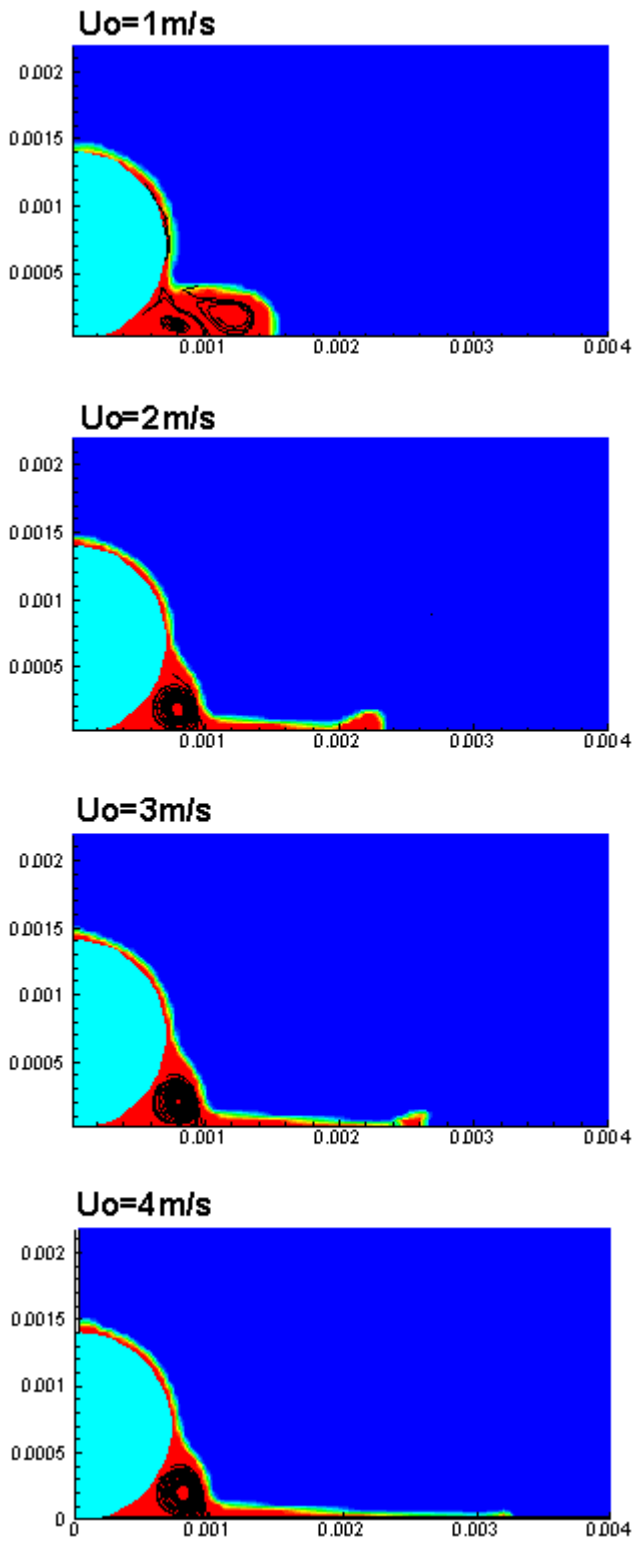

Figure 14- Snapshots of a semi-molten tin drop impact with drop size ($R = 1\ mm$) and core size ratio ($r/R = 0.7$) at $t^* = 1$. The impact velocity ranges from $U_o = 1\ m/s$ to $U_o = 4\ m/s$.

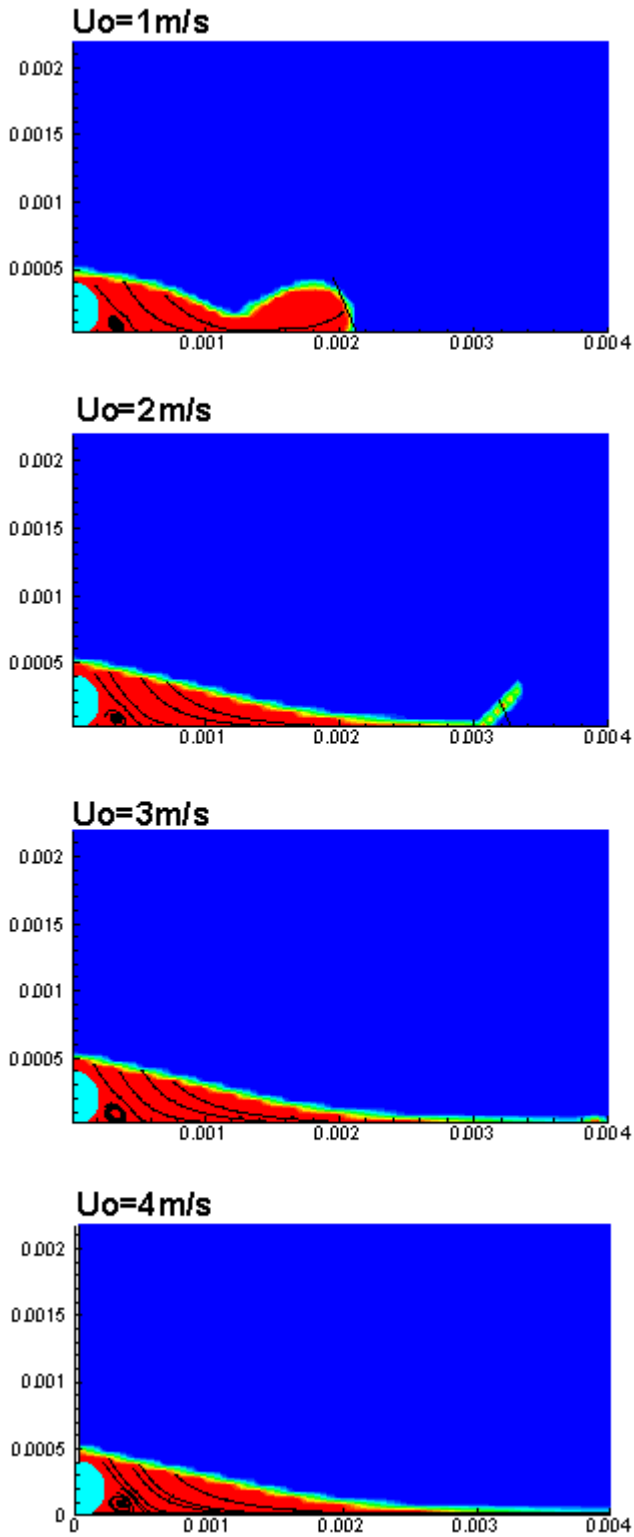

Figure 15- Snapshots of a semi-molten tin drop impact with drop radius ($R = 1\ mm$) and core size ratio ($r / R = 0.2$) at $t^* = 1$. The impact velocity ranges from $U_o = 1\ m/s$ to $U_o = 4\ m/s$.

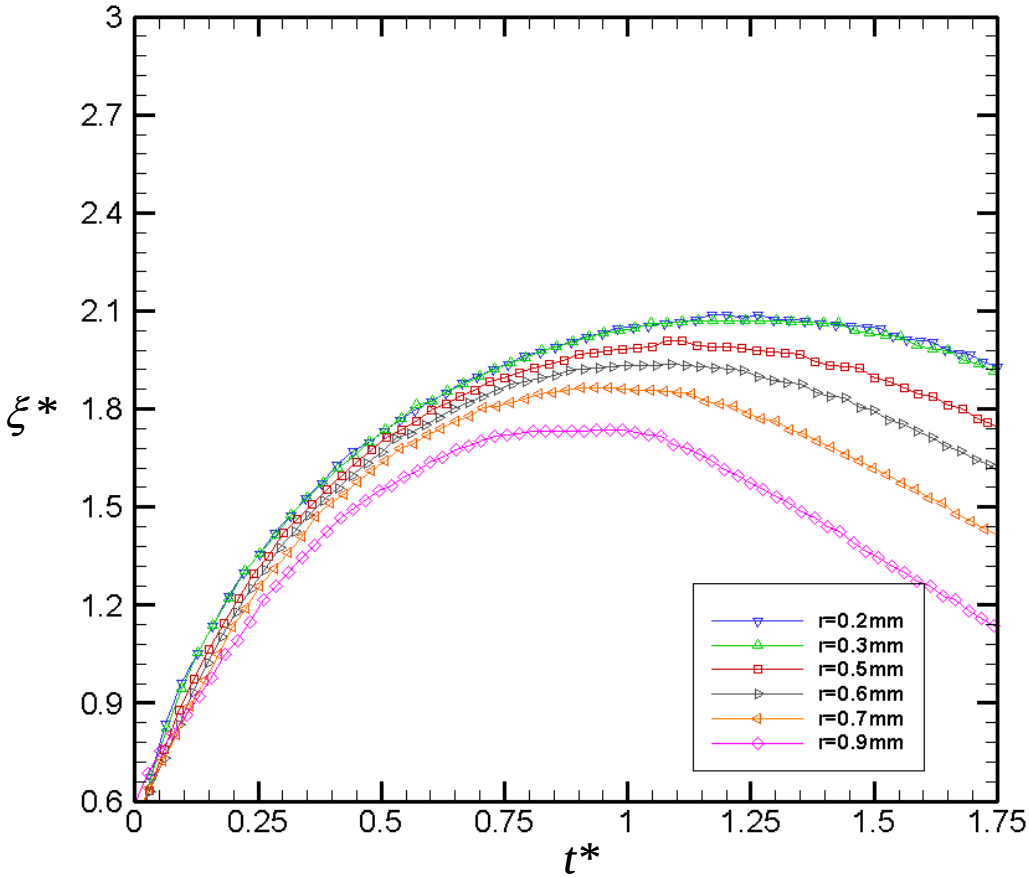

Figure 16- Modified spreading degree (ξ^*) vs non-dimensional time (t^*) for the impact of a semi-molten tin drop with varying the core size radii (r), and the corresponding drop radii (R) are scaled with r for the conserved volume $V_{consr} = 3.6652\ mm^3$. ξ^* is based on the equivalent diameter D_{liquid} for the fluid volume inside the drop.

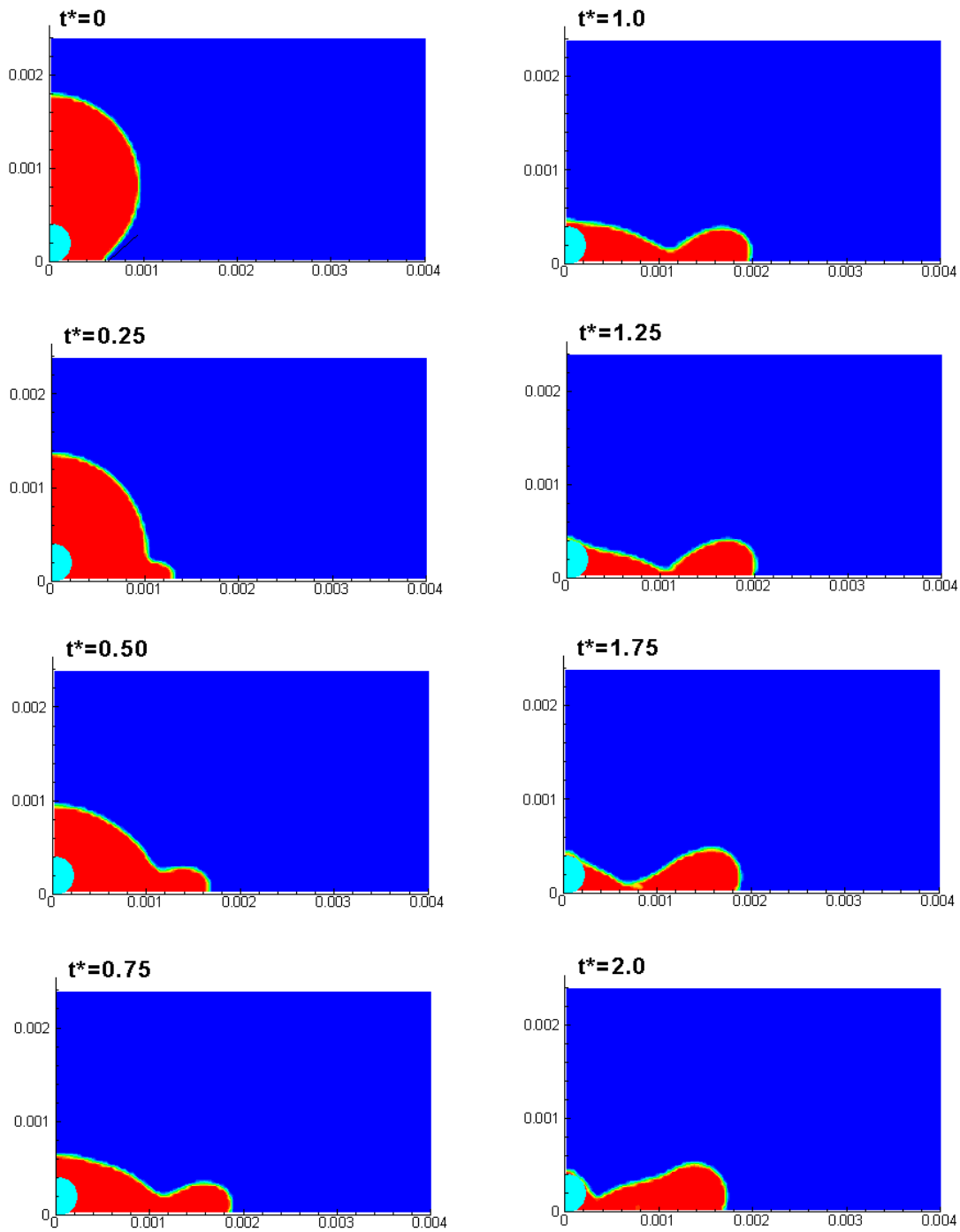

Figure 17- Snapshots of a semi-molten tin drop impact with core size r = 0.2mm and drop size R = 0.959 mm. The fluid volume is conserved, $V_{consr} = 3.6652\ mm^3$ **. The impact velocity is** $U_o = 1\ m/s$ **.**

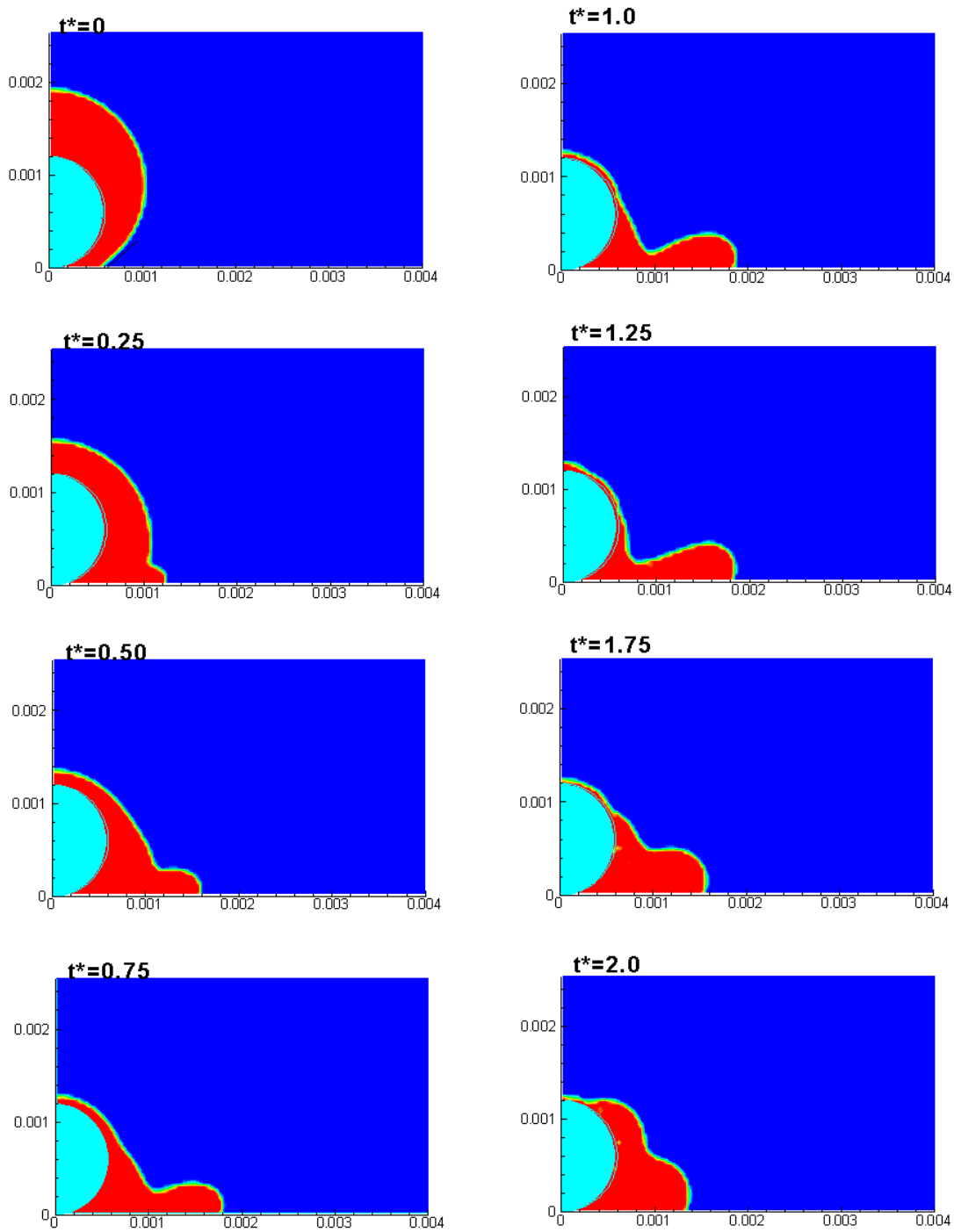

Figure 18- Snapshots of a semi-molten tin drop impact with core size r = 0.6 mm and drop size R = 1.029 mm. The fluid volume is conserved, $V_{consr} = 3.6652\ mm^3$ **. The impact velocity is** $U_o = 1\ m/s$ **.**

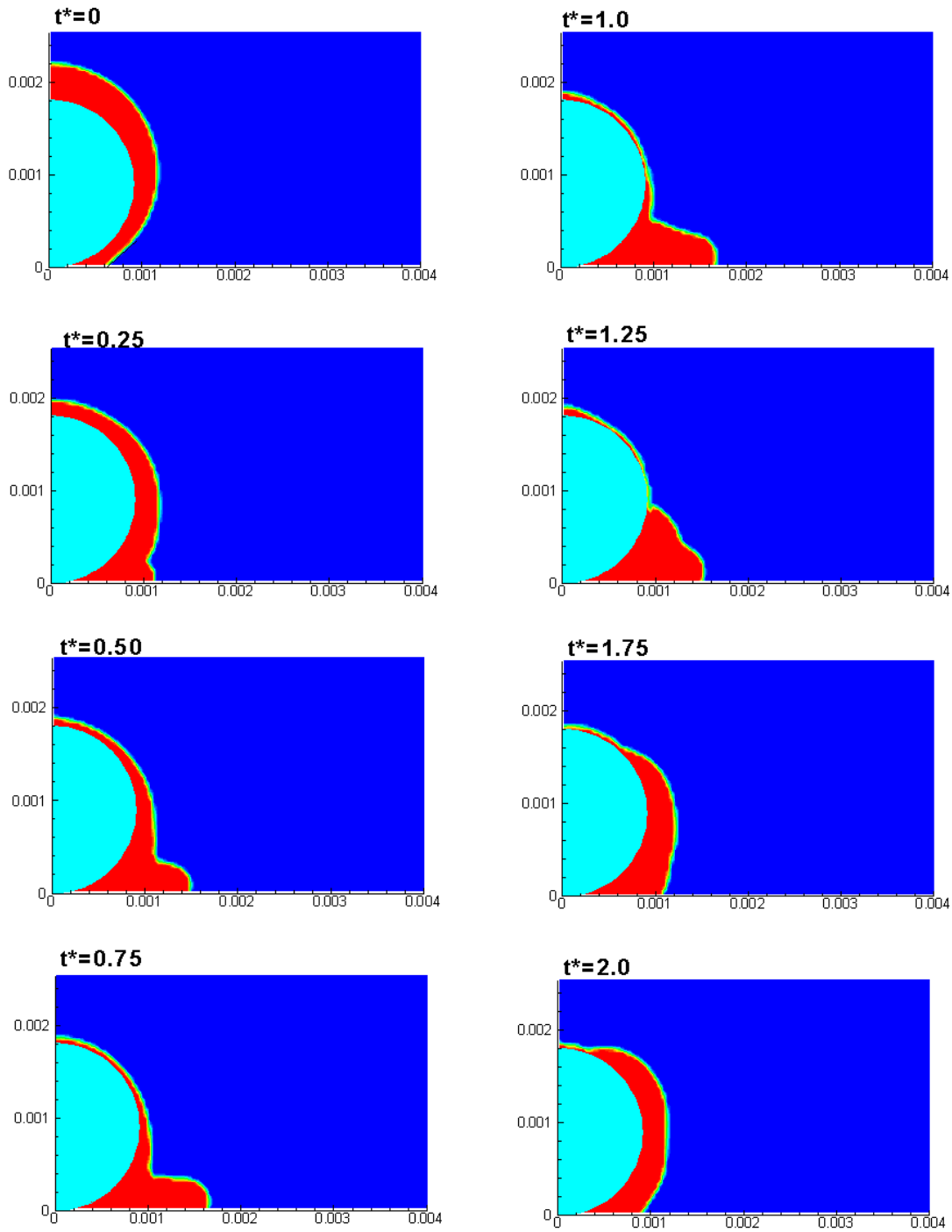

Figure 19- Snapshots of a semi-molten tin drop impact with core size r = 0.9mm and drop size R = 1.171 mm. The fluid volume is conserved, $V_{consr} = 3.6652\ mm^3$. The impact velocity is $U_o = 1\ m/s$.

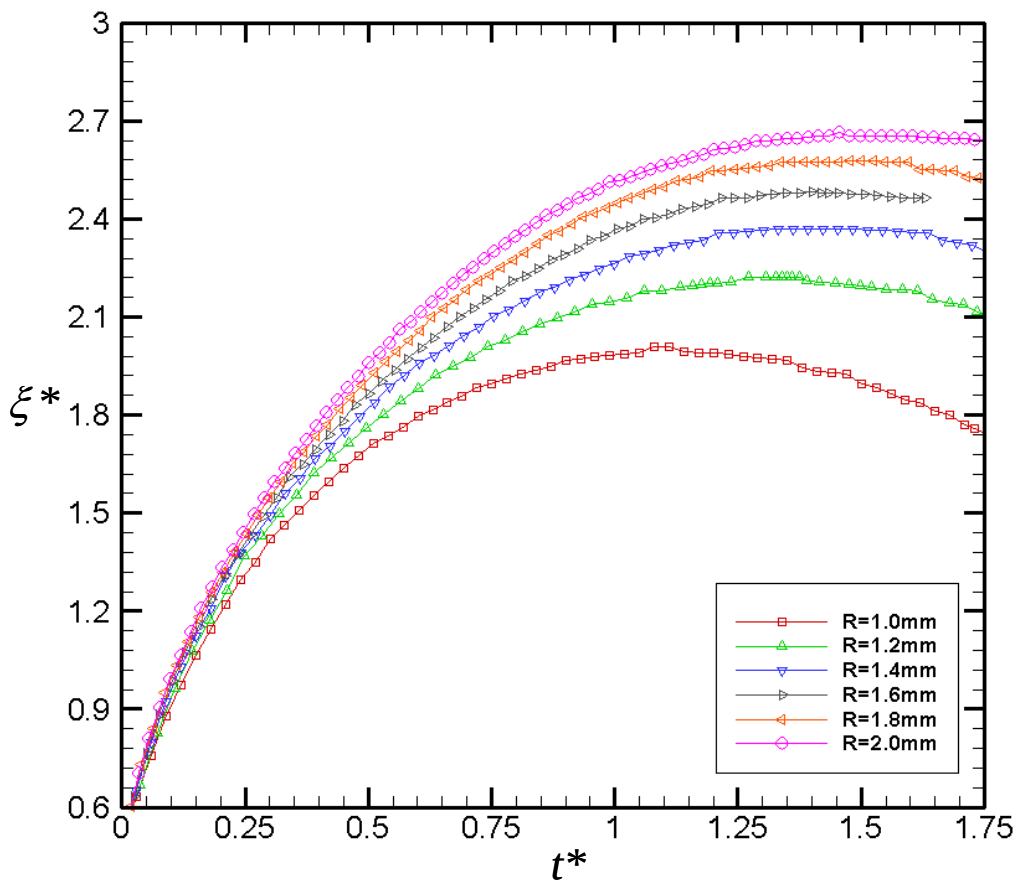

Figure 20- Modified spreading degree (ξ^*) vs non-dimensional time (t^*) for the impact of a semi-molten tin drop with constant core size ($r = 0.5\ mm$) and varying the drop radius (R). ξ^* is based on the equivalent diameter D_{liquid} for the fluid volume inside the drop.

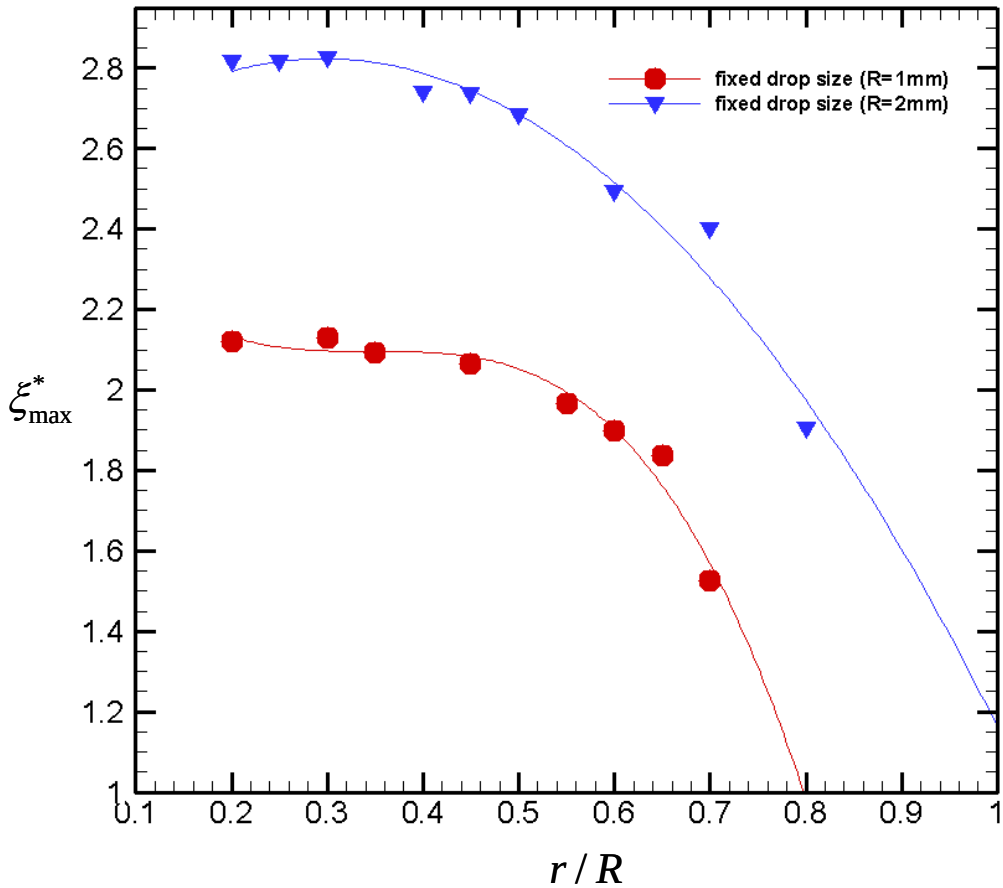

Figure 21- The maximum spread degree (ξ^*_{max}) vs the solid core size ratio (r / R) for constant drop radii of R=1mm and R=2mm.

CHAPTER 6

CONCLUSIONS

6.1 Conclusions

Recent development in the thermal spray industry has shown a growing interest in the low-temperature thermal spraying. The advantage of low-temperature spraying is that the initial composition of the feedstock powder can be maintained without suffering a significant degree of thermal degradation, caused by oxidation, decarburization, or dissolution during the deposition process. The disadvantage of low-temperature spraying is that the particle is usually partially-melted, and upon impact on the substrate, the spread degree of a semi-molten particle is lower, which leads to more voids (or porosity) in the as-deposited coating. To optimize the coating properties, a balance between the thermal degradation and the porosity level must be struck.

To begin to assess the balance between the thermal degradation and the porosity, a 2D model was developed to examine how a semi-molten droplet flattens upon impact on a substrate. The models solves for the fluid flow in the presence of a solid core by implementing the *Immersed Boundary* method.

Simulation was conducted for a semi-molten tin drop of radius R for a wide range of solid core radii r, varying the drop size ratio r/R, and the impact velocity U_o. The results confirm that the maximum spread degree $\xi^*_{\max}$ decreases as the solid core size r increases. There are two reasons for the change in fluid behavior during spreading when compared with a molten drop impact: (i) a recirculation flow is formed beneath the solid core, and (ii) less fluid becomes available for spreading.

Three process parameters were closely examined: the effect of impact velocity U_o, the effect of solid core size r, and the effect of drop size R. The effect of each parameter is described as follows.

(i): Increasing the impact velocity U_o increases the inertial energy of a semi-molten drop to overcome surface tension and viscous forces. Hence, fluid spreads further, forming a thinner splat, but the volume of fluid contributing to spreading remains the same since the size of the recirculation zone does not change with increasing U_o.

(ii): A larger solid core R impedes fluid motion to a greater extent than a smaller core, when the fluid volume remains constant. A larger core causes the splat periphery to recoil at an earlier time, which leads to a sphere-shape splat morphology.

(iii): The maximum spread degree $\xi^*_{\max}$ increases with increasing the drop size R when the solid core size r remains constant. As more fluid becomes available for spreading, the fluidity of a semi-molten drop increases.

6.2 Future Work

A list of recommended future work follows:

1. Currently, the model is restricted to a fixed solid core. The model should be generalized by incorporating free-moving solid particles within a drop by generalizing the *Immersed Boundary* method.

2. Converting this model into 3D coordinates would allow for the study of multiple solid particles within a drop.

3. Experimental work to validate semi-molten drop impacts at various solid core sizes, which can be correlated to the melting degree of a homogeneous particle, or to the solid core size of a composite particle such as WC-Co.